CHAPTER 4

NUMERICAL RESULTS AND DISCUSSION

This Chapter is concerned with the numerical results obtained from the solution procedure described in Chapter 3. A computer program has been developed to study electroelastic response of a finite piezoelectric cylinder subjected to mechanical loading and electric field. Two types of electrodes are considered, i.e. a smooth flexible electrode and a rough rigid one. Convergence and stability of numerical solutions are investigated and the accuracy of the present solution is verified by comparing with the existing solutions for isotropic and transversely isotropic cylinders. Numerical results are presented to demonstrate the influence of piezoelectric material parameters, cylinder shape and loading conditions on the displacements, stresses and electric field of the cylinder.

4.1 Numerical Scheme

The solution procedure described in the previous Chapter is implemented into a computer program. For the case of mechanical loading, three roots in equations (3.33) are first obtained to establish a system of linear simultaneous equations from the boundary conditions given by equations (3.64) to (3.69). For the case of electrical loading, the mixed boundary value problem is given by equations (3.86) and (3.90) for a smooth flexible electrode and equations (3.94) to (3.105) for a rigid electrode with a rough surface. The arbitrary constants are determined from a system of linear simultaneous equations. Finally, electroelastic fields of piezoelectric cylinder can be obtained by substituting the arbitrary constants into equations (3.58) to (3.63).

4.2 Convergence and Stability of Solution

First, the convergence of the loading function given by equation (3.77) is examined. For the parabolic loading applied at the top and bottom surfaces of the cylinder as shown in Figure 4.1(a), the Fourier Bessel series can be expressed as follows:

$$P(r) = (2r^2 - 1)q_0 = \sum_{s=1}^{\infty} \frac{8}{\lambda_s^2 J_0(\lambda_s)} J_0(\lambda_s r) \tag{4.1}$$

Figure 4.2(a) presents the partial sums of the parabolic loading function given by equation (4.2) for different r. It was found that the maximum error in the approximation of $P(r)$ occurs at r=0.0 and 1.0. Figure 4.2(b) shows the percentage of errors at r=0.0 and 1.0 with increasing number of s terms. The errors at both locations are less than 3% for both r=0.0 and 1.0 when s>30.

Next, consider the case of a cylinder subjected to the uniform pressure at the top and bottom surfaces as shown in Figure 4.1(b), in which

$$\sigma_{zz}(r, \pm h) = P(r) \tag{4.2}$$

where

$$P(r) = \begin{cases} -q_0 & 0 < r < r_0 \\ 0 & r_0 < r < 1 \end{cases} \tag{4.3}$$

and $P(r)$ can be expressed as

$$P(r) = -q_0 \left(r_0^2 + \sum_{s=1}^{\infty} \frac{2r_0 J_1(\lambda_s r_0)}{\lambda_s J_0^2(\lambda_s)} J_0(\lambda_s r) \right) \tag{4.4}$$

Figure 4.3 presents the convergence and error in approximation of the uniform load in Figure 4.1(b). It is obvious that the uniform loading requires more terms in the infinite series given by equation (4.4) to converge when compared to the parabolic loading. In addition, the number of terms required for convergence increase at r=0

and at the points of discontinuity (r=0.5). For example, in Figure 4.3(b), the error in approximation of $P(r)$ is less than 3% at r=0.05 and 0.10 when s>30, whereas, for r=0.0, the error could be as high as 10% even when s>100.

4.3 Comparison with Existing Solution

Chua and Wei (2000) presented the stress distributions within a finite isotropic solid circular of diameter $2R$ and length $2h$ under the double-punch test, in which two rigid circular punches of diameter $2a$ are applied at the top and bottom surfaces of the cylinder. The boundary conditions for a solid cylinder subjected to the double-punch test can be expressed as follows:

- At the curved surface, i.e. r=1 and $-h \le z \le h$

$$\sigma_{rr}(1,z) = 0 \tag{4.5}$$

$$\sigma_{rz}(1,z) = 0 \tag{4.6}$$

- At the top and bottom surfaces, i.e. $z = \pm h$ and $-1 \le r \le 1$

$$\sigma_{zz}(r,\pm h) = \begin{cases} P(r) \\ 0 \end{cases} \tag{4.7}$$

$$\sigma_{rz}(r,\pm h) = 0 \tag{4.8}$$

and

$$P(r) = \frac{P_0}{2a\pi\sqrt{a^2 - r^2}} \tag{4.11}$$

where P_0 is the magnitude of the applied point force. The boundary traction on $z = \pm h$ can be expanded into Fourier-Bessel series as (Watson, 1944).

$$\sigma_{zz} = -\frac{P_0}{\pi a R}\sum_{s=1}^{\infty}\frac{\sin(\lambda_s a)}{\lambda_s J_0^2(\lambda_s)}J_0(\lambda_s r) \tag{4.10}$$

where λ_s is the s^{th} root of the $J_1(x) = 0$, and $J_n(x)$ is the Bessel function of the first kind order n.

Figures 4.4 to 4.6 show comparisons of normalized hoop stresses and normalized vertical stresses from the present study with those given by Chua and Wei (2000) along the vertical axis of the cylinder by varying Poisson's ratio, the size of a punches and the shape of a cylinder. Excellent agreement between the two solutions is clearly demonstrated in those figures for all values of parameters.

Vendhan and Archer (1977) considered a transversely isotropic solid cylinder of radius R and height $2h$ subjected to the following boundary conditions.

- At the curved surface, i.e. $r=1$ and $-h \le z \le h$

$$\sigma_{rr}(1,z) = 0 \tag{4.11}$$

$$\sigma_{rz}(1,z) = 0 \tag{4.12}$$

- At the top and bottom surfaces, i.e. $z=\pm h$ and $-1 \le r \le 1$

$$\sigma_{zz}(r,\pm h) = P(r) \tag{4.13}$$

$$\sigma_{rz}(r,\pm h) = 0 \tag{4.14}$$

where $P(r)=\left(1-2r^2\right)E_m$ and E_m is the modulus of elasticity of a magnesium cylinder.

Figure 4.7 shows a comparison between normalized hoop stresses of magnesium cylinder with those given by Vendhan and Archer (1978) along the z-axis at r/R=0.0 and 0.5 and H/D=0.5 and 1.0. Comparisons between normalized hoop and radial stresses along the r-axis at z=0.0 for a magnesium cylinder with H/D=0.05 and 0.20 are presented in Figure 4.8. It can be clearly seen from Figures 4.7 and 4.8 that both solutions agree very closely. Note that the properties of the magnesium cylinder are given in Table 4.1.

4.4 Electroelastic Field of Cylinder under Mechanical Loading

Numerical results for four different types of piezoelectric materials, namely, $BaTiO_3$, PZT-4, PZT-5H and PZT-6B are presented in this section to demonstrate

the influence of various governing parameters on a piezoelectric cylinder. The material properties of the four piezoelectric materials are given in Table 4.1.

4.4.1 Cylinders under Different Mechanical Loading.

Numerical solutions for four different piezoelectric cylinders under both parabolic and uniform loads as shown in Figure 4.1 are presented in Figures 4.9 to 4.21. The case of a cylinder without piezoelectric effect, i.e., e_{ij}=0, is also considered for comparison. All results presented in Figures 4.9 to 4.21 correspond to the case of cylinders with H/D=1.0. In addition, the radius of the loading area for the uniform loading is kept constant as r_0/R=0.5.

Figures 4.9 and 4.10 show the normalized radial stress $\sigma_{rr}^{*}=\sigma_{rr}/q_0$ of four piezoelectric cylinders along the radial and vertical axes under parabolic loading and uniform loading, respectively, with H/D=1.0. From Figures 4.9(a) and 4.10(a), it can be seen that the radial stress is tensile at the center of the cylinder before approaching zero at the curved surface for both loading cases. The condition of zero radial stress at r/R=1.0 is not exactly satisfies in some cases for uniform loading because of precision problem discussed in section 4.2. In addition, it is also found that the magnitudes of radial stresses corresponding to the case of four piezoelectric cylinders are always greater than those of the non- piezoelectric ones.

Figures 4.11 and 4.12 show the normalized hoop stress $\sigma_{\theta\theta}^{*}=\sigma_{\theta\theta}/q_0$ for different piezoelectric cylinders along the radial and vertical axes under parabolic loading and uniform loading, respectively. It is found from Figure 4.11(a) and 4.12(a) that the hoop stress is always positive under parabolic loading for all piezoelectric materials. The hoop stress for $BaTiO_3$, PZT-4 and PZT-5H decreases along the r-axis, whereas, for PZT-6B, it increases before reducing near the edge of the cylinder. For non-piezoelectric materials, except $BaTiO_3$, the hoop stress increases along the r-axis. The variation of $\sigma_{\theta\theta}^{*}$ along the z-axis is similar to those of σ_{rr}^{*} in Figures 4.9(b) and 4.10(b) because of the axisymmetric condition.

Figures 4.13 and 4.14 illustrate the non-dimensional vertical stress, $\sigma_{zz}^{*} = \sigma_{zz} / q_0$ along the radial and vertical axes, respectively. The vertical stresses are compressive at r=0 and then decay rapidly along the r-axis as shown in Figures 4.13(a) and 4.14(a). They become zero in the vicinity of r=0.7 since the function of the parabolic loading is $P(r) = (2r^2 - 1)q_0$, therefore, $P(r)$ vanishes when r approaches to 0.7. The piezoelectric effect i.e. $e_{ij} \neq 0$ results in lower vertical stress for both parabolic and uniform loads. It is also noted from Figure 4.13(b) and 4.14(b) that the magnitude of the compressive stress increases along the z-axis from the center of the cylinder approaching unity at the boundaries.

Figures 4.15 and 4.16 present the non-dimensional vertical electric displacement, $D_z^{*} = D_z c_{44} / e_{31} q_0$ for $BaTiO_3$, PZT-4, PZT-5H and PZT-6B along radial and vertical axes, respectively. It should be noted that the materials without piezoelectric effect, i.e., e_{ij}=0, are not presented in Figures 4.15 and 4.16. In Figure 4.15(a) and 4.16(a), the vertical electric displacement is positive at the center of cylinder and then decreases along the radial axis. It is zero near r=0.7 due to the zero normal pressure at that location. Note that the condition of zero vertical electric displacement at the top end of the cylinder shown in Figure 4.15(b) and 4.16(b) is not satisfied exactly due to precision problem. The vertical electric displacement remains positive along the vertical axis. D_z^{*} increases rapidly from center of cylinder to peak value near z/R=0.7. Thereafter, it gradually decreases along the z-axis approaching zero at the top surface.

Non-dimensional vertical electric fields $E_z^{*} = E_z e_{31} / q_0$ along the radial and vertical axes are shown in Figures 4.17 and 4.18, respectively. In Figure 4.17(a) and 4.18(a), the vertical electric field is maximum at r=0 and gradually decreases along the r-axis for both parabolic and uniform loads. The maximum value of E_z^{*} along the z-axis in Figure 4.17(b) and 4.18(b) occurs near z/R=0.7 for all materials. Note that the vertical electric field under parabolic loading is always negative along r-axis and z-axis except near the edge and the top end of the cylinder. However, for uniform loading, E_z^{*} is negative throughout the two axes.

Non-dimensional radial displacements $u_r^* = u_r c_{44} / Rq_0$ for all materials along the radial axis as shown in Figures 4.19(a) and 4.19(b) for parabolic and uniform loading, respectively, are zero at r=0. The radial displacements then increase along the r-direction reaching the maximum values near r/R=0.6. In Figures 4.20(a) and 4.20(b), the vertical displacements $u_z^* = u_z c_{44} / Rq_0$ along the vertical axis under parabolic and uniform loading, respectively, are presented. They are zero at z=0 for all four materials and gradually increase along the vertical axis. Significant difference between u_r^* and u_z^* corresponding to the cases of $e_{ij} = 0$ and $e_{ij} \neq 0$ is noted. It appears that the absence of piezoelectric effect would increase the displacement due to the parabolic and uniform loads which means that the dielectric failure would lead to softening of the material. However, for PZT-6B , the absence of the piezoelectric effect does not produce a substantial change in the radial displacement because the properties of PZT-6B are similar to those of an elastic material. This was earlier observed by Rajapakse and Zhou (1997).

Figure 4.21 shows the variation of electric potential $\phi^* = \phi e_{31} / Rq_0$ of four piezoelectric materials along the vertical axis due to the parabolic and uniform loads of magnitude q_0. It can be seen from those figures that the electric potential is zero at z=0 before monotonically increases along the z-axis. Note that the shear stress, radial electric displacement and radial electric field are zero along the r-axis at z=0 and z-axis at r=0 for the parabolic and uniform loading. In addition, the radial displacement along the z-axis and the vertical displacement along the r-axis under both loading cases are also zero.

4.4.2 Cylinders for Different Shape Factors.

Figures 4.22 to 4.34 show the normalized radial stress, hoop stress, vertical stress, electric displacement, electric field, mechanical displacements and electric potential for different shape factors, i.e., H/D=0.5, 1.0, 2.0 and 5.0, along the radial and vertical axes. In addition, two piezoelectric materials, $BaTiO_3$ and PZT-5H are considered for both parabolic and uniform loads.

Figures 4.22 and 4.23 show the normalized radial stress along the radial and vertical axes under parabolic loading and uniform loading, respectively. The variation of the radial stress due to the parabolic loading is similar to that in Figure 4.9(a) for a short cylinder (H/D<2.0). The radial stress is maximum at the center before decreasing along the radial direction. The magnitude of σ_{rr}^{*} decreases with increasing the value of H/D. Only tensile stress occurs for σ_{rr}^{*} along the r-axis at z=0 of the cylinder under vertical loading at the end except for a short cylinder with H/D=0.5. Significant compressive stress is developed for r/R>0.5 as shown in Figure 4.23(a). The results in Figure 4.22(b) and 4.23(b) indicate that the maximum compressive stress occurs near both ends of the cylinder. The peak tensile shifts towards the end of the cylinder when H/D is increased. In addition, the maximum values of tensile stress for all ratios of H/D are nearly identical. This implies that the tensile strength does not depend on the shape of the cylinder. This behavior was also noted by Chen and Yuan (1980) for the case of an isotropic cylinder.

Figures 4.24 and 4.25 show non-dimensional hoop stress along the radial and vertical axes of piezoelectric cylinders under parabolic and uniform loading, respectively. The values of the hoop stress for H/D>2 are almost negligible for both $BaTiO_3$ and PZT-5H, which is consistent with the one-dimensional theory as shown in Figures 4.24(a) and 4.25(a).

Figures 4.26 and 4.27 show the non-dimensional vertical stress $\sigma_{zz}^{*}=\sigma_{zz}/q_0$ along the radial and vertical axes of cylinder under parabolic and uniform loading, respectively. As expected, the vertical stress at the middle plane of the cylinder (z=0) are constant, for $H/D \geq 2$, approaching a one-dimensional solution. For parabolic loading in Figure 4.1(a), the total vertical stress in this case is equal to zero since

$$\int_0^1 2\pi r(2r^2-1)dr = 0 \qquad (4.15)$$

whereas, for uniform loading in Figure 4.1(b), the vertical stress is equal to 0.25 since

$$\frac{\int_{0}^{r_0=0.5} 2\pi r dr}{\pi r^2} = 0.25 \qquad (4.16)$$

Figures 4.26(b) and 4.27(b) show the variation of the normalized vertical stress along the z-axis at $r=0$ under parabolic and uniform loading, respectively. It can be seen from these two figures that only compressive stress occurs along the vertical axes under both loading types and the maximum stresses are found at the end surfaces. The vertical stresses decay rapidly before approaching a one-dimensional solution for a long cylinder ($H/D \geq 2.0$). This once again demonstrates the applicability of one-dimensional solution for a long cylinder.

Figures 4.28 and 4.29 present the non-dimensional vertical electric displacement under parabolic and uniform loading, respectively, for different ratios of H/D. The variation of D_z^* along the radial direction for a short cylinder, i.e., $H/D \leq 1.0$, in Figures 4.28(a) and 4.29(a) is similar to what observed in Figures 4.15(a) and 4.16(a). Note that D_z^* for a long cylinder ($H/D \geq 2.0$) diminishes into a negligible value at the middle plane ($z=0$). Numerical results in Figures 4.28(b) and 4.29(b) indicate that, for all ratios of H/D, D_z^* is zero at the loaded ends. For $H/D \geq 1.0$, D_z^* abruptly increases reaching the maximum value at the vicinity of the end surface before decreasing rapidly along the vertical axis. For $H/D=0.5$, however, the maximum value of D_z^* is found at the middle plane of the cylinder.

Figures 4.30 and 4.31 show the normalized vertical electric field along the r-axis at $z=0$ and z-axis at $r=0$ for cylinders of different H/D. In the Figures 4.30(a) and 4.31(a), the variation of vertical electric field, $E_z^* = E_z e_{31}/q_0$ along the r-axis is qualitatively similar to that of the vertical stress shown in Figures 4.26(a) and 4.27(a). For the case of a long cylinder ($H/D \geq 2.0$), E_z^* at the middle plane ($z=0$) approaches the one-dimensional solution, i.e., zero for parabolic loading, and 0.0137 and 0.0323 for $BaTiO_3$ and PZT-5H, respectively, for uniform loading. The variation of the vertical electric field along the vertical axis in Figure 4.30(b) and 4.31(b) is similar to that of the vertical electric displacement in Figure 4.28(b) and 4.29(b).

Figure 4.32 shows non-dimensional radial displacement at the middle plane under both parabolic and uniform loads for different values of H/D. For parabolic loading, u_r^* for a short cylinder ($H/D \leq 1.0$) increases from zero at the center approaching the maximum value near r/R=0.6. Thereafter, it gradually decreases along the r-axis to the edge of the cylinder. On the other hand, for a long cylinder ($H/D \geq 2.0$), u_r^* is almost negligible at the middle plane. For uniform loading, u_r^* for a short cylinder is similar to that under parabolic loading. However, for a long cylinder, u_r^* is zero at the center and then linearly increases along the radial direction reaching the maximum value at the edge of the cylinder.

The variations of u_z^* along the vertical axis are presented for parabolic and uniform loading in Figure 4.33(a) and 4.33(b), respectively. Numerical results indicate that except for a long cylinder ($H/D \geq 2.0$) under parabolic loading, u_z^* linearly increases along the vertical axis from zero at the center reaching the maximum value at the loaded end. For a cylinder with $H/D \geq 2.0$ under parabolic loading, u_z^* decreases rapidly from the maximum value at the loaded end until reaching zero value at the center of the cylinder.

Figure 4.34 shows the variation of the non-dimensional electric potential along the vertical axis of cylinder under both parabolic and uniform loads. The general trend of ϕ^* is similar to that of u_z^* along the vertical axis as shown in Figure 4.33. Note that a piezoelectric material PZT-5H generates a larger electric potential in the central region of the cylinder when compared to that in a $BaTiO_3$ cylinder.

4.4.3 Cylinder for Various Radii of Applied Uniform Load.

Figures 4.35 to 4.42 show the normalized stresses, electric displacement, electric field, mechanical displacements and electric potential along the radial and vertical axes due to the uniform loading of intensity q_0 for various radii of applied load (see Figure 4.1(b)). Note that all numerical results correspond to the case of cylinders with H/D=1.0.

Figure 4.35 shows the normalized radial stress along the radial and vertical axes. The radial stress is positive at the center of cylinder and diminishes along the radial axis to the zero value at the curved surface for r_0/R=0.50 and 0.80. However, for r_0/R=0.10 and 1.00, σ_{rr}^* is nearly zero for the entire middle plane as shown in Figure 4.35(a). In Figure 4.35(b), the tensile stress occurs when $-0.6 < z < 0.6$ for r_0/R=0.5 and 0.8, and the maximum tensile stress is found at the center. For r_0/R=0.1 and 1.0, no significant tensile stress is developed along the vertical axis. Note that the maximum compressive stress is found near the loaded ends of the cylinder for all ratios of r_0/R except when $r_0 = R$.

Figure 4.36 presents the non-dimensional hoop stress along the radial and vertical axes of the cylinder. The characteristics of $\sigma_{\theta\theta}^*$ along both axes are similar to those of σ_{rr}^* shown in Figure 4.35. The variation of $\sigma_{\theta\theta}^*$ along the r-axis when r_0/R=0.50 and 0.80, gradually decreases from the maximum value at the center reaching the minimum value at the loaded ends. When r_0/R=0.10 and 1.0, $\sigma_{\theta\theta}^*$ is nearly constant along the r-axis with the value being much lower than the other two cases. Note that $\sigma_{\theta\theta}^*$ for $r_0 = R$ is almost negligible along both axes.

Figure 4.37 shows the non-dimensional vertical stress along the r-axis and z-axis. For r_0/R=0.10 and 1.00, it is observed that the vertical stresses are -0.01 and -1.00, respectively, at the middle plane of the cylinder (z=0) as shown in Figure 4.37(a). This value is exactly equal to the one-dimensional solution.

Figure 4.38(a) illustrates the non-dimensional vertical electric displacement which is positive along the r-axis and decays to zero near r/R=0.6. In Figure 4.38(b), it is found that the vertical electric displacement remains positive along the vertical axis and increases from r/R=0.0 to its peak value. Thereafter, it gradually reduces with z/R to zero value at z/R=1.0 due to the boundary condition. The location of the peak shifts towards the end surfaces as the radius of applied load is increased, while the maximum value of D_z^* decreases with increasing r_0. Note that

D_z^* is equal to zero throughout the r-axis and z-axis for r_0/R=1.0. This implies that the piezoelectric effect does not occur when $r_0 = R$.

Figure 4.39 shows the non-dimensional vertical electric field along the r-axis and z-axis. The variation of E_z^* along the r-axis is similar to those for σ_z^* shown in Figure 4.37(a). Note that the vertical electric field is uniform for r_0/R=1.00 along both r- and z-axes.

Figures 4.40 and 4.41 show the non-dimensional radial and vertical displacements along the r-axis and z-axis, respectively. It is found that both radial and vertical displacements increase with increasing the radius of applied load. For r_0/R=1.00, the radial and vertical displacements linearly increase along the r-axis and z-axis of a cylinder which is similar to one-dimensional behavior. In addition, the general trend of electric potential along the vertical axis shown in Figure 4.42 is similar to what observed for u_r^* in Figure 4.40. Note that ϕ^* increases as r_0 increases and a piezoelectric material PZT-5H generates higher electric potential than $BaTiO_3$.

4.5 Electroelastic Field of Cylinder under Electric Loading

In this section, electroelastic response of a piezoelectric cylinder subjected to the electrical loading applied to the top and bottom surfaces as shown in Figure 3.3 is investigated.

4.5.1 Cylinder under Different Electrodes

The influence of the stiffness and the condition of contact surface of the electrodes is examined by considering three piezoelectric materials, namely, $BaTiO_3$, PZT-4 and PZT-5H, under applied electric potential. All results presented in Figures 4.43 to 4.50 correspond to the cylinders with H/D=1.0 the radius of electrodes being equal to $0.5R$.

Figure 4.43 shows the variation of non-dimensional radial stress, $\sigma_{rr}^{**} = \sigma_{rr}R/e_{31}\phi_0$, along the radial and vertical axes of a cylinder for flexible and rigid

electrodes. The maximum tensile stress of σ_{rr}^{**} along the radial axis at z=0 for both flexible and rigid electrodes occurs at r=0 and approaches to zero value at the curved surface where r/R=1.00. The radial stress along the z-axis is tension at the center, z=0, and decreases with the vertical axis. In addition, the magnitude of the radial stress for the case of the rigid electrode is always higher than that of the flexible one.

Profiles of non-dimensional hoop stress, $\sigma_{\theta\theta}^{**} = \sigma_{\theta\theta} R / e_{31}\phi_0$, along both r- and z-axes as shown in Figure 4.44 indicate that $\sigma_{\theta\theta}^{**}$ is positive at the center of cylinder ($r = z$ =0) and remains positive throughout the radial axis of cylinder for the case of the rigid electrode. For the case of the flexible electrode, the hoop stress is positive at r=0 and becomes negative for r/R>0.5. The variation of $\sigma_{\theta\theta}^{**}$ along the z-axis is similar to that of σ_{rr}^{*} in Figure 4.43(b).

Figures 4.45(a) and 4.45(b) show the variation of non-dimensional vertical stress, $\sigma_{zz}^{**} = \sigma_{zz} R / e_{31}\phi_0$, along r-axis at z=0 and along z-axis at r=0 of a piezoelectric cylinder, respectively. The maximum value of σ_{zz}^{**} in the case of a rigid electrode occurs at the center of cylinder, then it decreases with the radial distance. The vertical stress along the vertical axis increases from the center to the maximum value at the top end for a rigid electrode. For the flexible electrode, on the other hand, it decreases from the maximum value at the center to zero at both ends. The vertical stress in the case of flexible electrode is significantly smaller than that of a cylinder under the rigid electrode.

Figure 4.46 shows the variation of non-dimensional vertical electric displacement, $D_z^{**} = D_z c_{44} R / e_{31}\phi_0$, along r-axis at z=0 and z-axis at r=0 of the piezoelectric cylinder. The profiles of D_z^{**} are almost parallel along both r- and z-axes for both flexible and rigid electrodes. Numerical results indicate that the vertical electric displacements for all three piezoelectric materials are negative along both axes. The maximum value along the r-axis is at the center and D_z^{**} decreases along the radial distance for both flexible and rigid electrodes. However, the maximum value of D_z^{**} is found at both ends of cylinder and it gradually decreases to the minimum value at the center.

Figure 4.47 shows the variation of non-dimensional vertical electric field, $E_z^{**} = E_z R/\phi_0$, along r-axis at z=0 and z-axis at r=0 of the piezoelectric cylinder. E_z^{**} is negative along the r-axis with the maximum value being at the center of piezoelectric cylinder. Thereafter, it decreases rapidly along the radial axis. On the other hand, the minimum negative value of E_z^{**} is at z=0 before increasing along the vertical axis reaching the maximum values at both ends.

Figure 4.48 shows the normalized radial displacement, $u_r^{**} = u_r e_{31}/c_{44}\phi_0$ along r-axis at z=0 for both flexible and rigid electrodes. The radial displacement is zero at r=0 and gradually increases along the radial axis for the flexible electrode. However, for the rigid electrode, u_r^{**} is nearly zero for $0<r/R<0.4$. Profiles of non-dimensional vertical displacement, $u_z^{**} = u_z e_{31}/c_{44}\phi_0$ along z-axis at r=0 are presented in Figure 4.49. The vertical displacement is also zero at z=0 before increasing almost linearly along the z-axis for the case of flexible electrode. For the rigid electrode, u_z^{**} is almost zero throughout the vertical axis. A substantial difference for both u_r^{**} and u_z^{**} corresponding to the case of flexible and rigid electrodes is noted. It is found that smaller displacements along both r- and z- axes occur under rigid electrodes due to the electric potential loading.

Figure 4.50 shows the non-dimensional electric potential, $\phi^* = \phi/\phi_0$ along the z-axis at r=0 for different electrode conditions. The electric potential is zero at z/R=0.0 before increasing nearly linearly along z-axis approaching 1.0 at the end surfaces. It is found that the difference between of electric potentials corresponding to the case of flexible and rigid electrodes is almost negligible.

Figures 4.51 to 4.53 present the normalized shear stress, vertical stress and vertical electric displacement along the r-axis for various different value of z/R for $BaTiO_3$ cylinder under rigid electrode. In addition, H/D=1.0 and r_0/R=0.5. In Figure 4.51, the shear stress under the electrodes is zero at the center of cylinder, i.e., r=0 before increasing to the maximum value at r_0/R=0.5. The shear stress becomes zero outside the electrodes, i.e., $r_0/R>0.5$, which agrees with the boundary condition given by as shown in equation (3.104). The vertical stress and the electric

displacement are negative under the electrodes and equal to zero outside the contact area, r_0 / R>0.5. In addition, the variation of vertical stress along the r-axis in Figure 4.52 is similar to that of the vertical electric displacement in Figure 4.53.

Figures 4.54 to 4.56 present the non-dimensional radial displacement, vertical displacement and electric potential along the r-axis for different the z/R. From the boundary conditions given in Chapter 3, u_r^{**} and u_z^{**} are zero at the contact surfaces.

4.5.2 Cylinders of Different H/D Ratios

Figures 4.57 to 4.69 show the electroelastic field of a cylinder under electrical loading with different geometry of cylinder, i.e. H/D=0.5, 1.0, 2.0 and 5.0. Two piezoelectric materials under both flexible and rigid electrodes are considered with the radius of the electrodes being equal to 0.5 R.

Figures 4.57 and 4.58 show the non-dimensional radial stress along the r-axis at z=0 and z-axis at r=0 with flexible and rigid electrodes, respectively. In Figures 4.57(a) and 4.58(a), the variation of radial stress along the r-axis is the same as those in Figure 4.43. The magnitude of radial stress decreases with increasing the shape factor, H/D. The radial stress along the z-axis at r=0 for the short cylinder ($H/D \leq 1.0$), is positive at the center of cylinder and then rapidly increases along the vertical axis. For a long cylinder, $H/D \geq 2$, the radial stress at the middle plane (z=0) is nearly zero which implies that a one-dimensional solution is valid for a long cylinder under applied electric loading.

Figures 4.59 and 4.60 show the non-dimensional hoop stress along the r-axis at z=0 and z-axis at r=0 of two piezoelectric cylinders with flexible and rigid electrodes, respectively. The hoop stress for the case of the flexible electrodes is positive at r=0 and decays along the radial axis, until becoming negative near r/R=0.5. For the case of rigid electrodes, the hoop stress is positive throughout radial axis. In addition, it is found that the hoop stress for a long cylinder ($H/D \geq 2$) is almost zero along both axes which is consistent with the one-dimensional solution.

Figures 4.61 and 4.62 show the non-dimensional vertical stress along the r-axis at z=0 and z-axis at r=0 with flexible and rigid electrodes, respectively. For a

short cylinder ($H/D \leq 1.0$) the maximum compressive stress for the flexible electrode is found at the center of a cylinder. σ_{zz}^{**} then decreases with radial distance and becomes positive for $r/R>0.5$. For the rigid electrodes, the vertical stress is compressive and decreases with increasing the shape factor, H/D. For a long cylinder, $H/D>2$, σ_{zz}^{**} is nearly zero for the case of flexible electrodes. However, for the rigid electrodes, the vertical stress of a long cylinder is almost constant along both r- and z-axes.

Figures 4.63 and 4.64 show the non-dimensional vertical electric displacement along the r-axis at $z=0$ and z-axis at $r=0$ for both flexible and rigid electrodes, respectively. Along r-axis, the vertical electric displacement is negative with the maximum value being at $r=0$. D_z^{**} decays with the radial distance for a short cylinder, whereas for a long cylinder ($H/D \geq 2$), the vertical electric displacement is almost constant along the r-axis Figures 4.65 and 4.66 show the non-dimensional vertical electric field along the r-axis at $z=0$ and z-axis at $r=0$. The variation of the vertical electric field is similar to that of the vertical electric displacement as shown in Figure 4.63 and 4.64.

Figures 4.67 and 4.68 show the normalized radial displacement along r-axis at $z=0$ and the normalized vertical displacement along z-axis at $r=0$, respectively for both flexible and rigid electrodes. The radial displacement is zero at $r=0$ and increases along the radial axis. For a long cylinder with $H/D \geq 2$, the radial displacement is nearly linear due to the solution approaching to a one-dimensional solution. In the case of flexible electrodes, the vertical displacement along the z-axis at $r=0$ increases with the vertical distance. In addition, for the rigid electrodes, the vertical displacement is zero at $z=0.0$ and then increases to the maximum value near $z/R=0.5$. Thereafter, it decreases to zero at the top end of cylinder.

Figures 4.69(a) and 4.69(b) show the non-dimensional electric potential along z-axis at $r=0$ for flexible and rigid electrodes, respectively. The electric potential is zero at $z=0$ and increases almost linearly to unity at $z/R=1.0$ due to the boundary condition. The variation and magnitude of the electric potential corresponding to the cases of flexible and rigid electrodes are nearly identical.

4.5.3 Influence of Various Radii of Electrodes r_0 / R.

Figures 4.70 to 4.83 show the non-dimensional electroelastic fields of two piezoelectric materials, i.e., $BaTiO_3$ and PZT-5H, subjected to electrical loading at the top and end surfaces with the shape factor H / D=1.0. The influence of the radius of electrodes is examined in this section.

Figures 4.70 and 4.71 show the non-dimensional radial stress along the r-axis at z=0 and z-axis at r=0 for flexible and rigid electrodes, respectively. From Figures 4.70(a) and 4.71(a), it can be seen that the radial stress is positive at the center of the cylinder before approaching zero at the curved surface of the cylinder for both types of electrodes. The largest radial stress along the r-axis at z=0.0 corresponds to the case of r_0 / R=0.5 followed by r_0 / R=0.1, 0.8 and 1.0, respectively. For r_0 / R=1.0, it is observed that the radial stress is nearly zero for both flexible and rigid electrodes.

Figure 4.72 and 4.73 show the non-dimensional hoop stress along the r-axis at z=0 and z-axis at r=0 for flexible and rigid electrodes, respectively, for different radii of electrodes. For the flexible electrode, the hoop stress is tensile at r=0 and then decays rapidly along the r-axis as shown in Figure 4.72(a). It becomes zero in the vicinity of r / R=0.5 before changing to compressive stress when r>0.5R. In addition, for the case of rigid electrodes, the hoop stress is positive throughout the middle plane at z=0.

Figures 4.74 and 4.75 show the non-dimensional vertical stress along the r-axis at z=0 and z-axis at r=0 for flexible and rigid electrodes, respectively. For the case of a flexible electrode, the vertical stress is negative at the center of the cylinder and changes into tensile stress at r / R>0.6 for PZT-5H. In the case of a $BaTiO_3$ cylinder, σ_{zz}^{**} remains tensile stress at r / R<0.6 before becoming compressive stress. However, the magnitude of σ_{zz}^{**} for a $BaTiO_3$ cylinder is smaller than that of a PZT-5H cylinder. In addition, σ_{zz}^{**} is negative throughout the radial distance of cylinder at z=0 under a rigid electrode.

Figures 4.76 and 4.77 show the non-dimensional vertical electric displacement along the r-axis at $z=0$ and z-axis at $r=0$ for flexible and rigid electrodes, respectively, for different the radii of electrodes. When $r_0/R=1$, it is observed that the vertical electric displacement is nearly constant for both conditions, i.e., flexible and rigid electrodes. In addition, D_z^{**} corresponding to the case of a flexible electrode is smaller than that in the case of a rigid electrode.

Figures 4.78 and 4.79 show the non-dimensional vertical electric field along the r-axis at $z=0$ and z-axis at $r=0$ for flexible and rigid electrodes, respectively, with different radii of electrodes. It is found that, E_z^{**} is -1.0 when $r_0=R$ at the middle plane ($z=0$) as shown in Figures 4.78(a) and 4.79(a). In addition, it is also observed that the variations of E_z^{**} for both flexible and rigid electrodes are nearly identical. This implies that the variation of the vertical electric field does not depend on the rigidity of the electrodes and the contact condition between the electrodes and the cylinder.

Non-dimensional radial and vertical displacements along the radial and vertical axes are shown in Figures 4.80 and 4.81, respectively for both flexible and rigid electrodes. The radial displacements is zero at $r=0.0$ before increasing along the r-axis and reaching the maximum value at the curved surface, i.e., $r=R$. It is found that both radial and vertical displacements increase with increasing the radius of electrodes. When $r_0/R=1$, u_r^{**} and u_z^{**} for the flexible electrode linearly increase along the r- axis and z-axis, respectively. In addition, the vertical displacement along the z-axis for the rigid electrode is zero at $z=0.0$ and 1.0 due to the boundary conditions given in Chapter 3.

Figures 4.82(a) and 4.82(b) present the non-dimensional electric potential along the z-axis for the case of flexible and rigid electrodes, respectively. It is found that ϕ^{**} is zero at $z/R=0.0$ and 1.0. For $r_0/R=0.8$ and 1.0, the electric potential linearly increase along the z-axis from the center to the end of the cylinder.

Table 4.1 Material properties

	Magnesium	$BaTiO_3$	PZT-4	PZT-5H	PZT-6B
c_{11} (10^{10} N m^{-2})	5.64	15	13.9	12.6	16.8
c_{12} (10^{10} N m^{-2})	2.30	6.6	7.78	7.95	6.0
c_{13} (10^{10} N m^{-2})	1.81	6.6	7.43	8.41	6.0
c_{33} (10^{10} N m^{-2})	5.86	14.6	11.5	11.7	16.3
c_{44} (10^{10} N m^{-2})	1.68	4.4	2.56	2.3	2.71
e_{15} (C m^{-2})	-	11.4	12.7	17.0	4.6
e_{31} (C m^{-2})	-	-4.35	-5.2	-6.55	-0.9
e_{33} (C m^{-2})	-	17.5	15.1	23.3	7.1
ε_{11} (10^{-9} F m^{-1})	-	9.87	6.45	15.38	3.6
ε_{33} (10^{-9} F m^{-1})	-	11.15	5.62	12.76	3.4

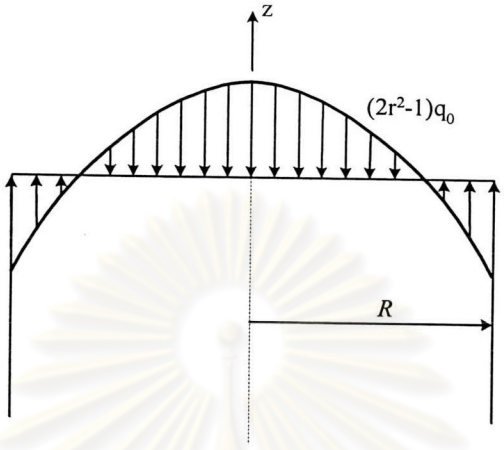

(a) Parabolic loading

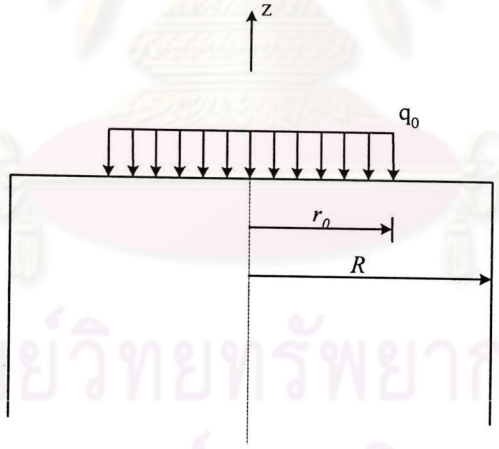

(b) Uniform loading

Figure 4.1 Piezoelectric cylinder subjected to axisymmetric load.

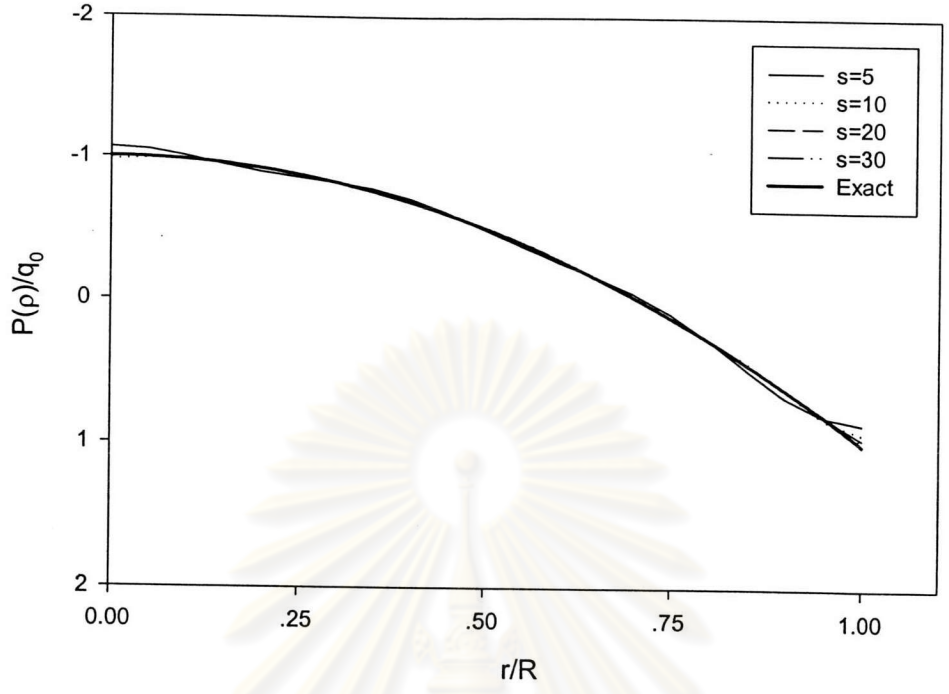

(a) Series expansion of the parabolic loading.

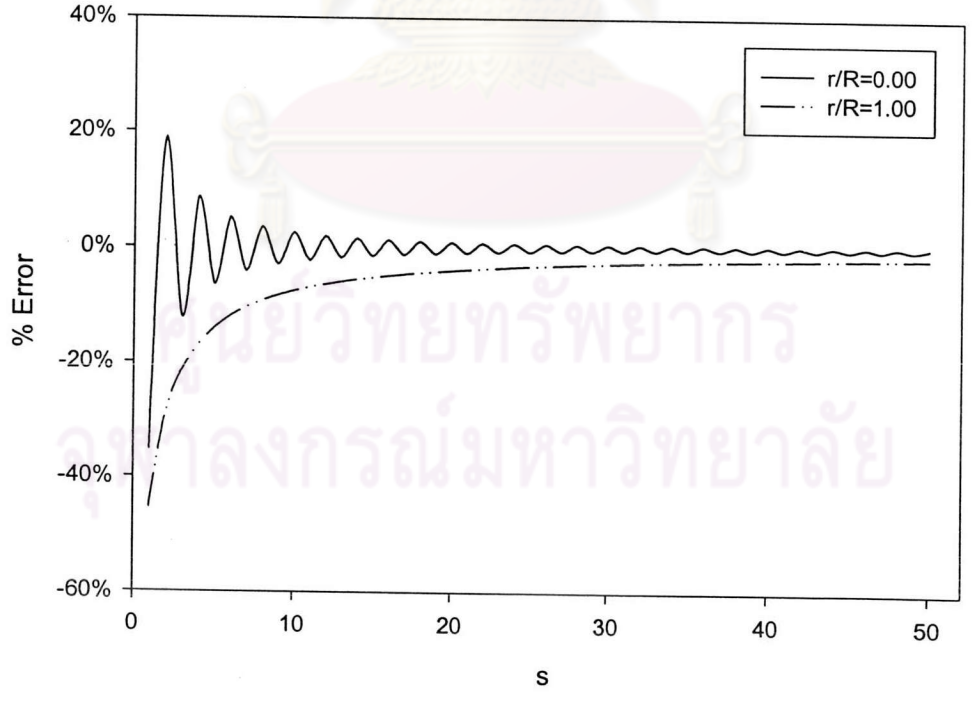

(b) Percent of error for the series expansion of the parabolic loading at r/R=0.00 and r/R=1.00 for different s values.

Figure 4.2 Convergence of parabolic load on the top and bottom surfaces of cylinder

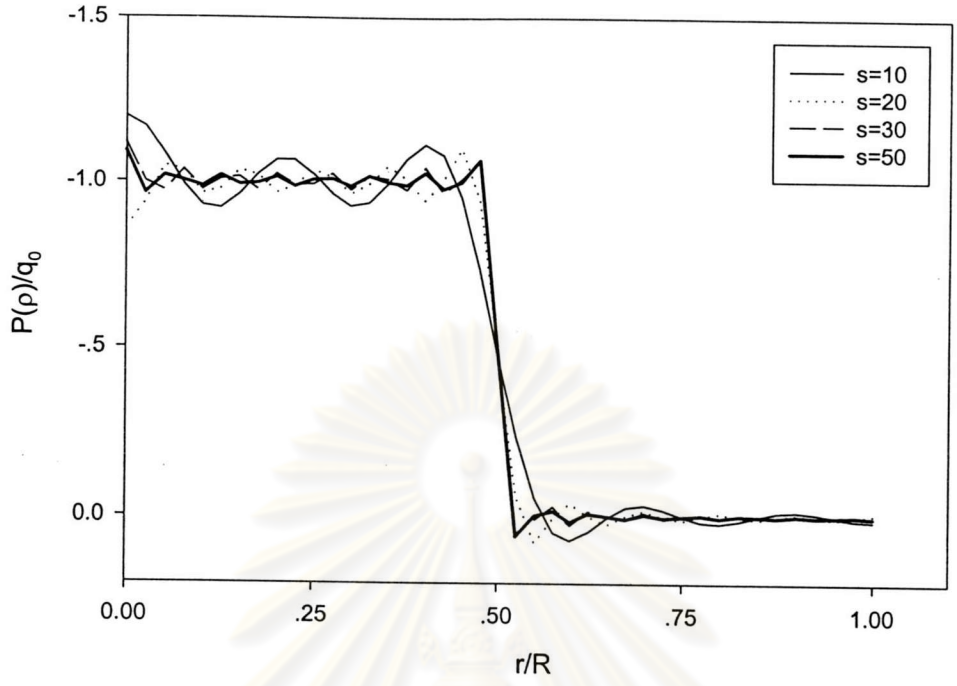

(a) Series expansion of the uniform loading.

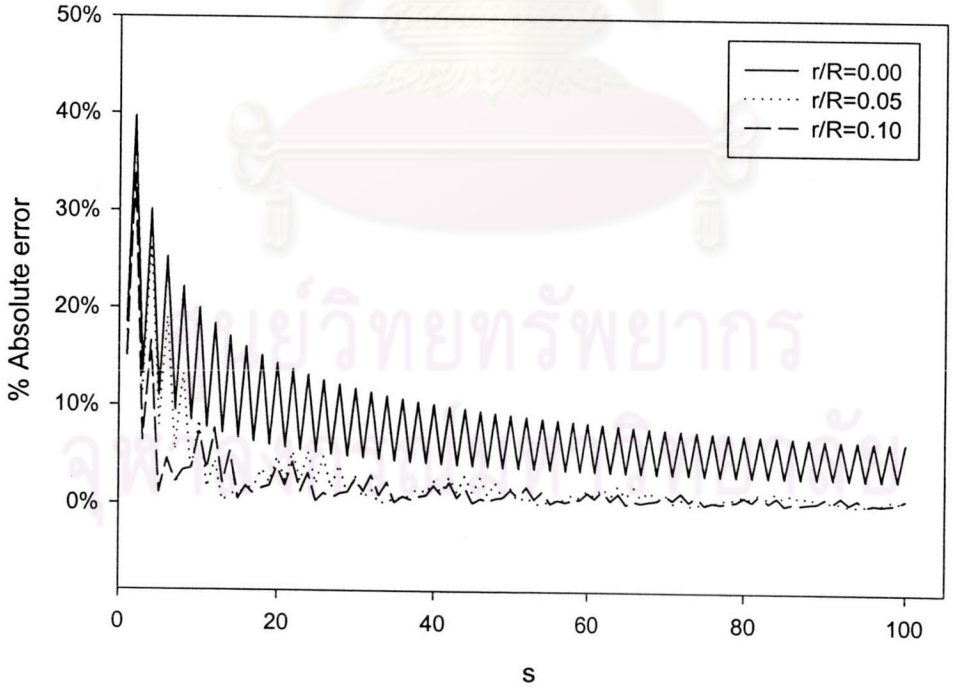

(b) Percent of error for the series expansion of the uniform loading at r/R=0.00, 0.05 and 0.10 for different s values.

Figure 4.3 Convergence of uniform load on the top and bottom surfaces of cylinder

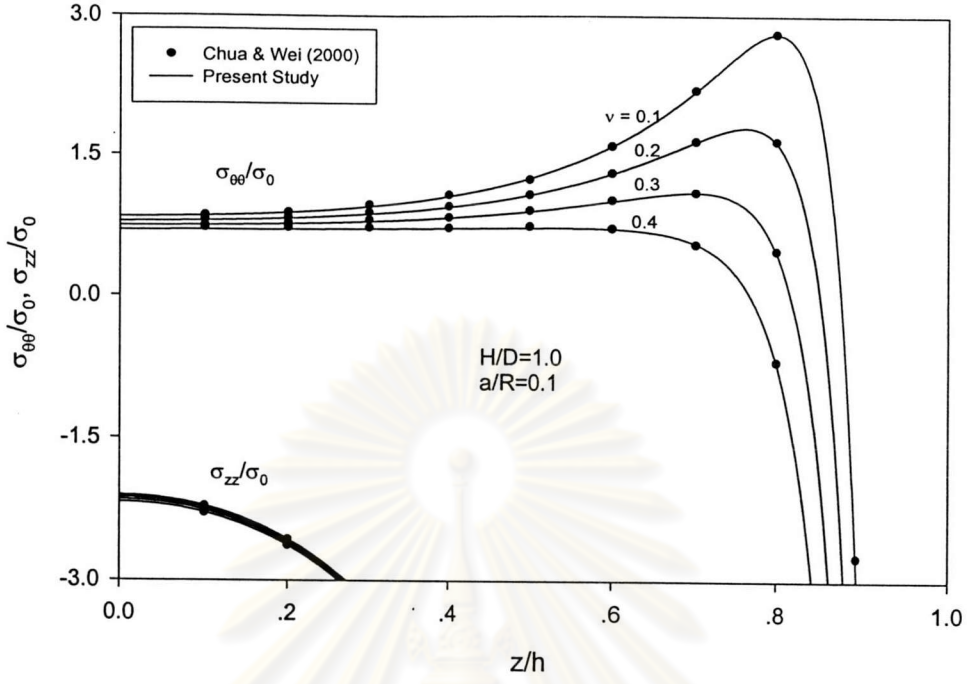

Figure 4.4 Normalized stresses $\sigma_{\theta\theta}/\sigma_0$ and σ_{zz}/σ_0 stresses versus normalized distance *z/h* for isotropic cylinder for various Poisson's ratio.

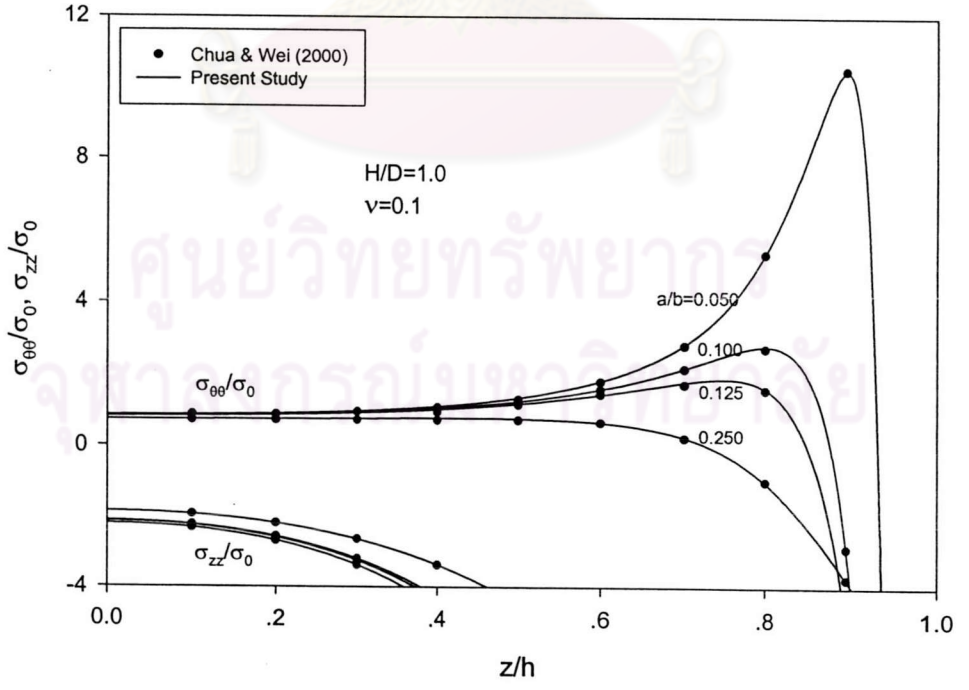

Figure 4.5 Normalized stresses $\sigma_{\theta\theta}/\sigma_0$ and σ_{zz}/σ_0 stresses versus normalized distance z/h for isotropic cylinder for various size of punches.

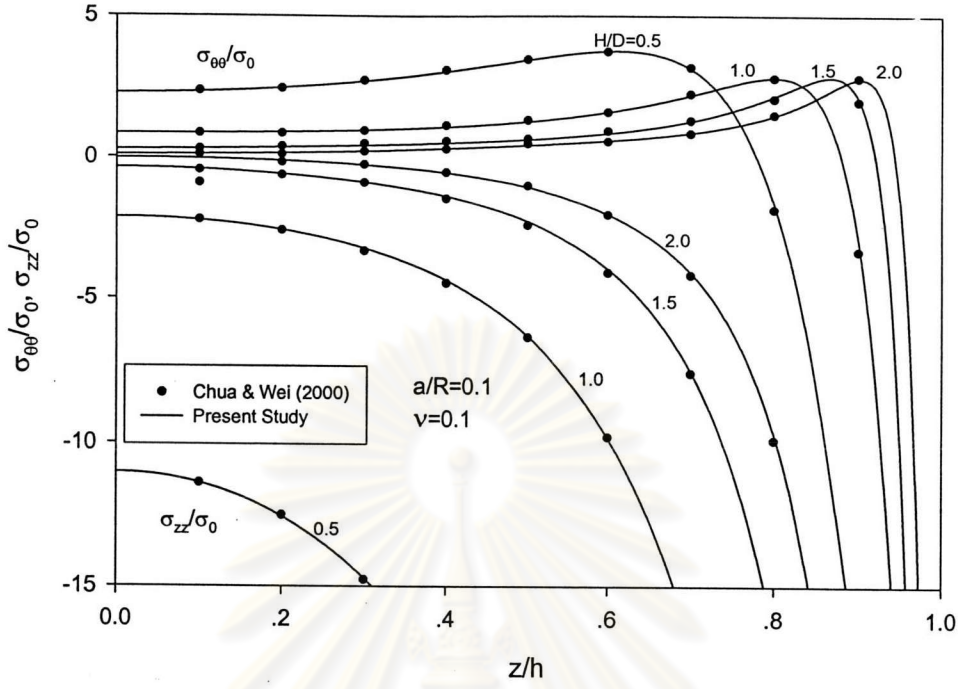

Figure 4.6 Normalized stresses $\sigma_{\theta\theta}/\sigma_0$ and σ_{zz}/σ_0 stresses versus normalized distance z/h for isotropic cylinder for various size of punches.

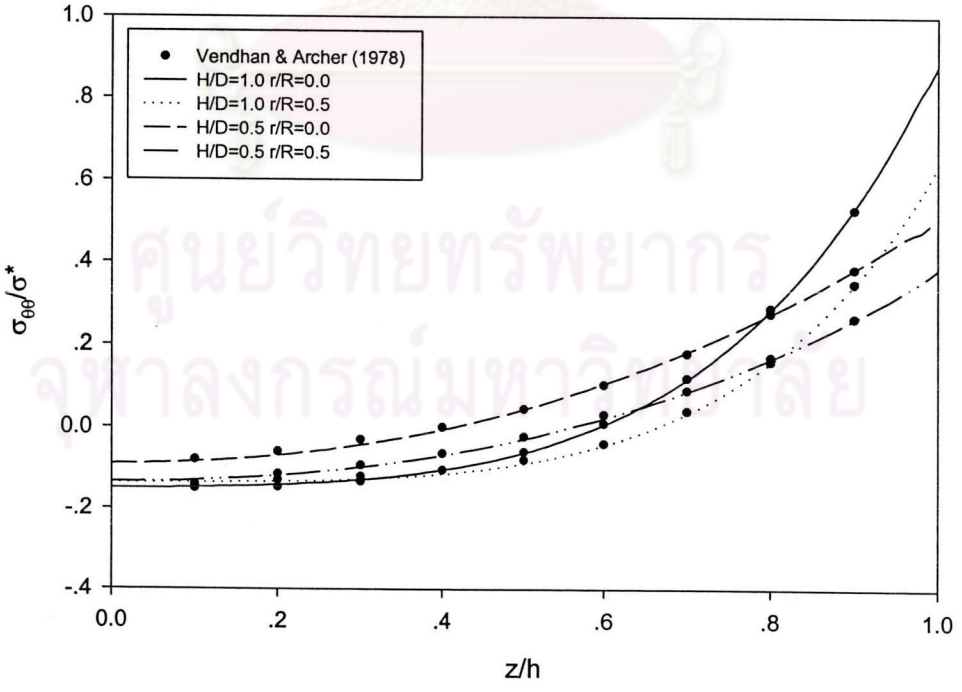

Figure 4.7 Normalized stress $\sigma_{\theta\theta}/\sigma^*$ versus normalized distance z/h for transversely isotropic cylinder of Magnesium.

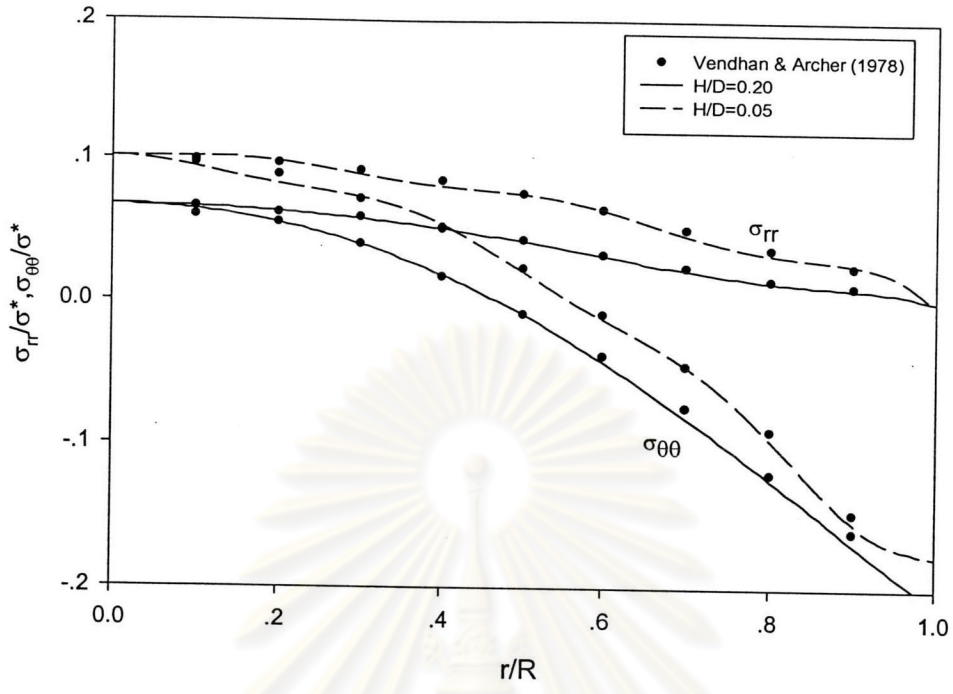

Figure 4.8 Normalized stresses hoop and axial stresses versus normalized distance r/R for transversely isotropic cylinder of Magnesium.

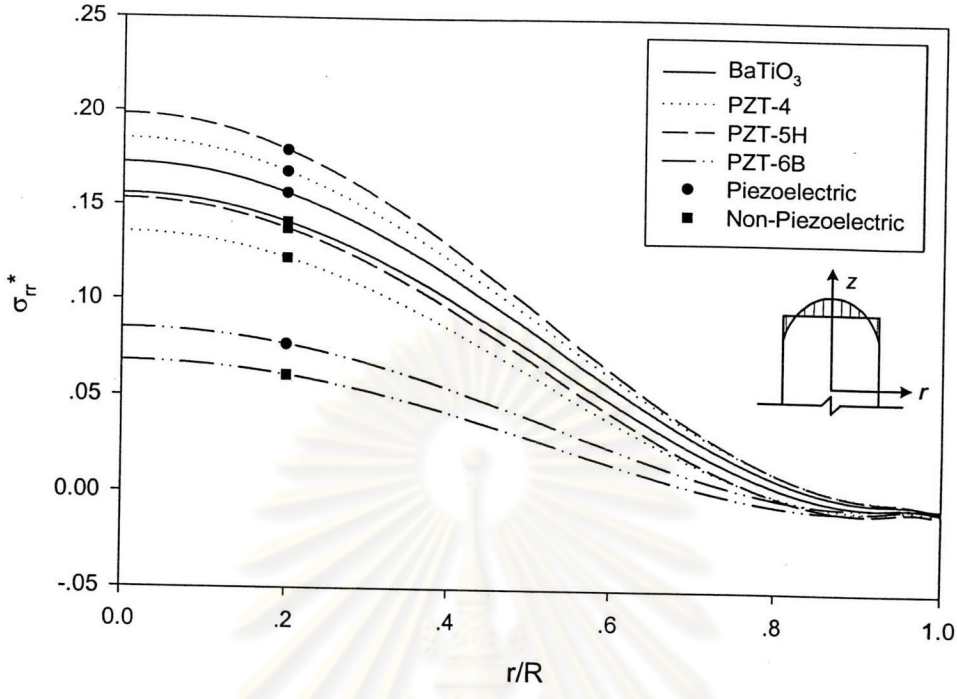

(a) Along r-axis at $z=0$.

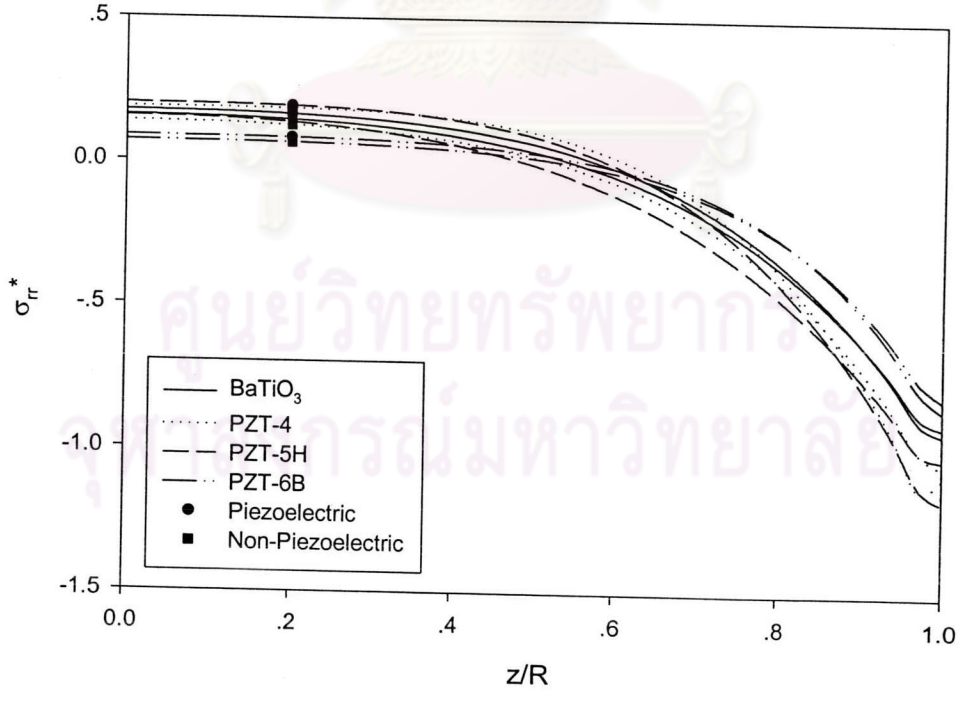

(b) Along z-axis at $r=0$.

Figure 4.9 Non-dimensional radial stress profiles due to parabolic load for different materials.

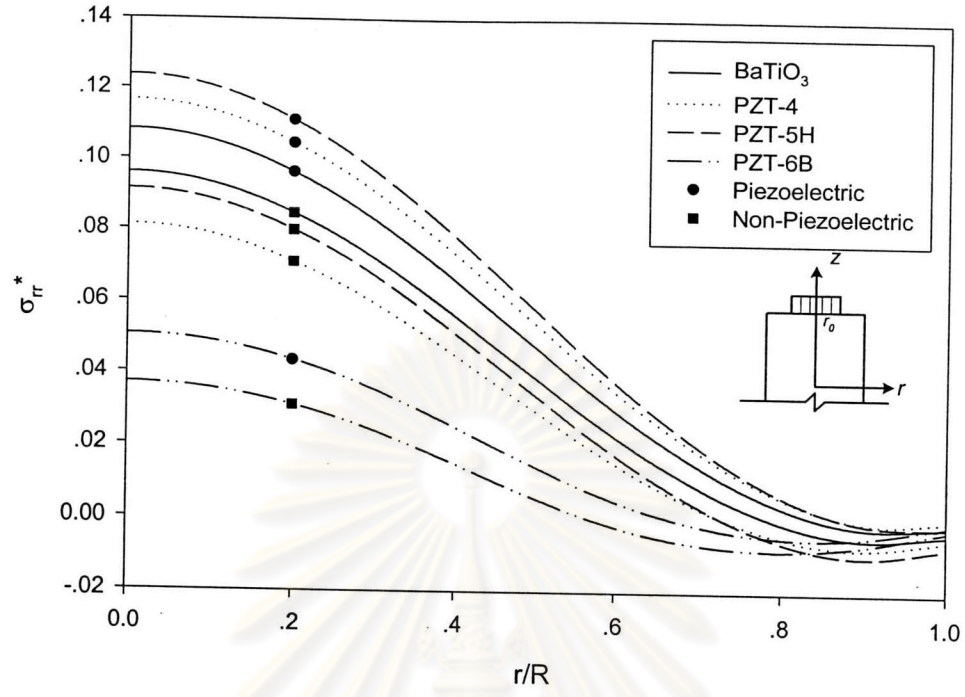

(a) Along r-axis at z=0.

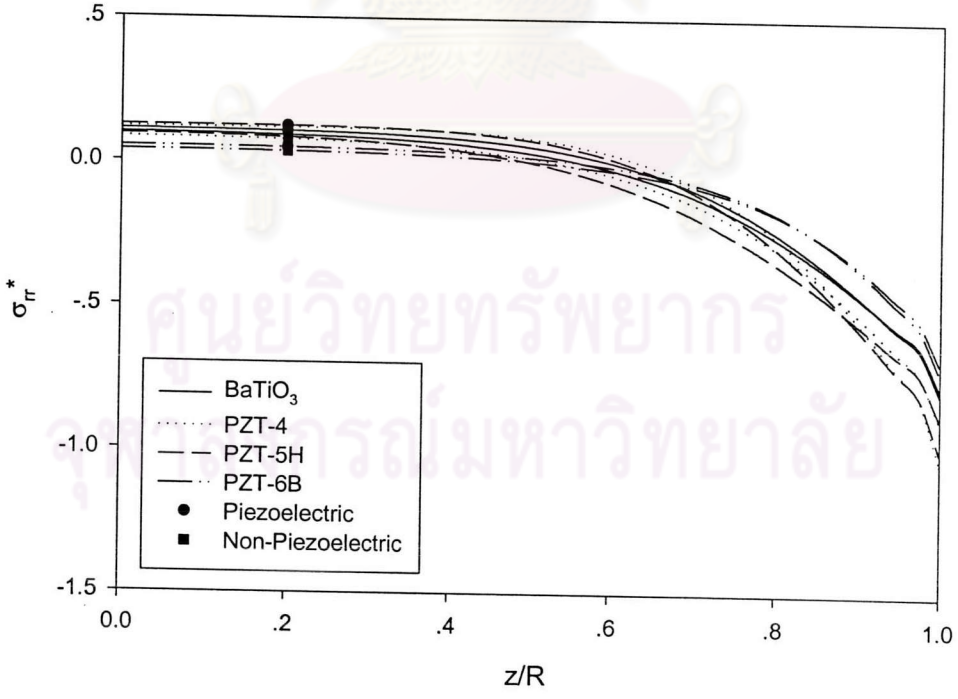

(b) Along z-axis at r=0.

Figure 4.10 Non-dimensional radial stress profiles due to uniform load for different materials.

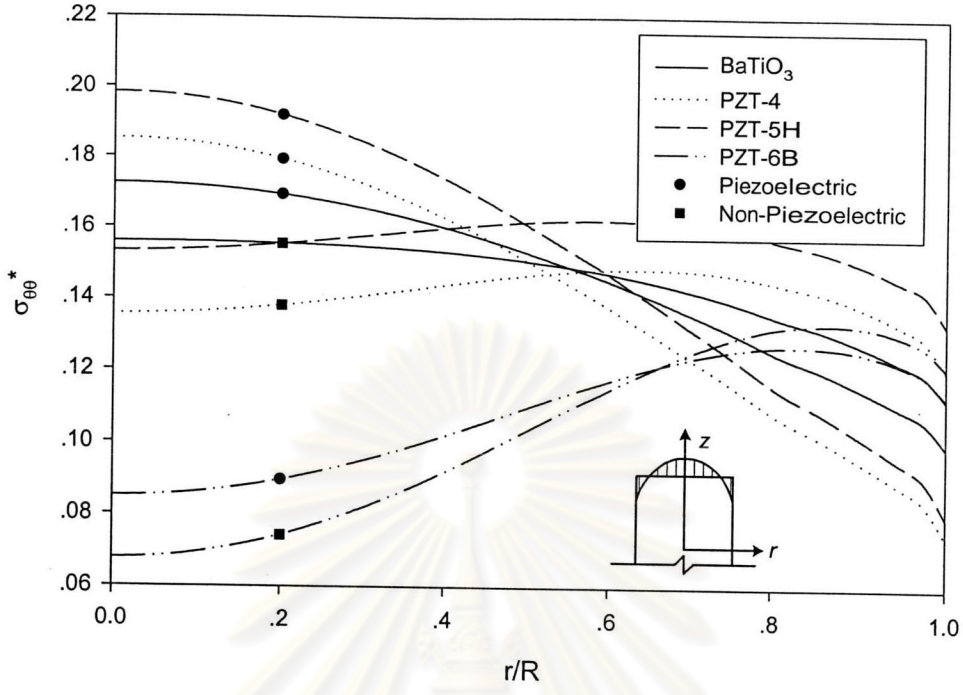

(a) Along r-axis at z=0.

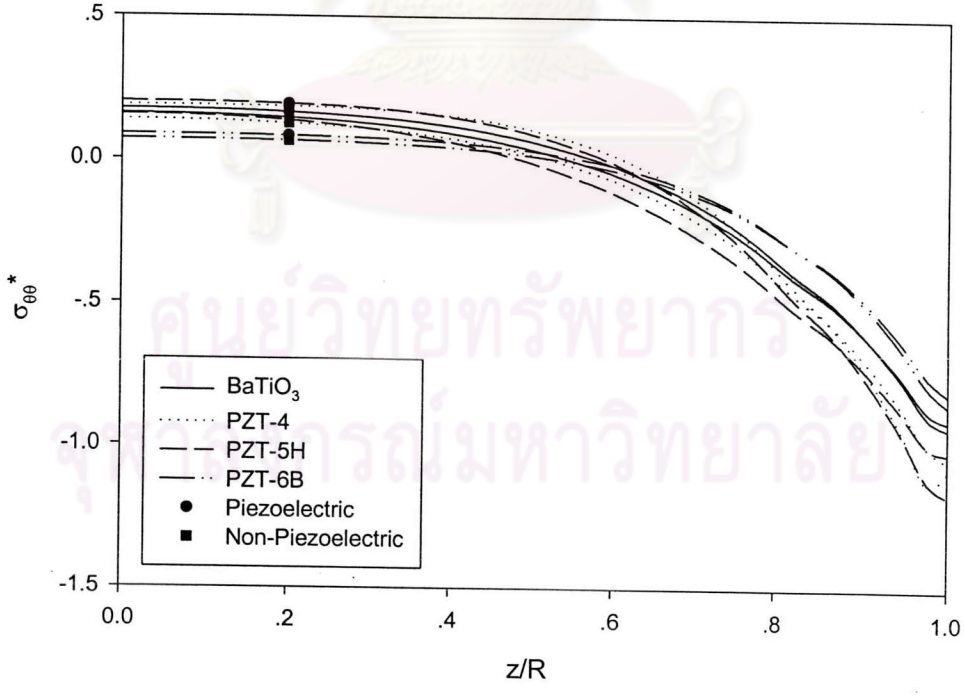

(b) Along z-axis at r=0.

Figure 4.11 Non-dimensional hoop stress profiles due to parabolic load for different materials.

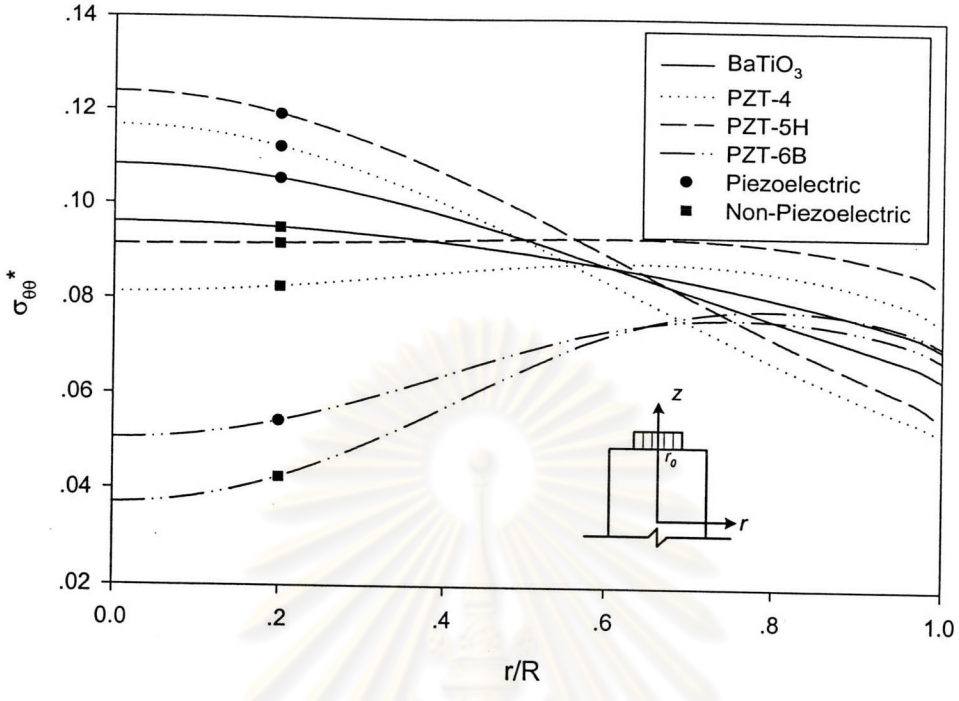

(a) Along r-axis at z=0.

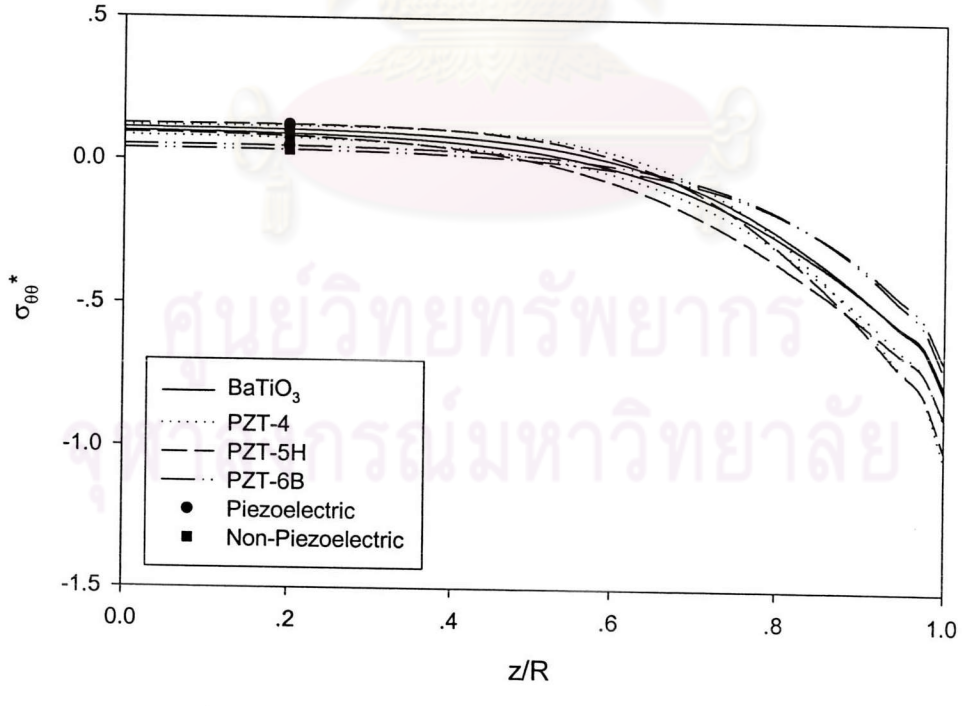

(b) Along z-axis at r=0.

Figure 4.12 Non-dimensional hoop stress profiles due to uniform load for different materials.

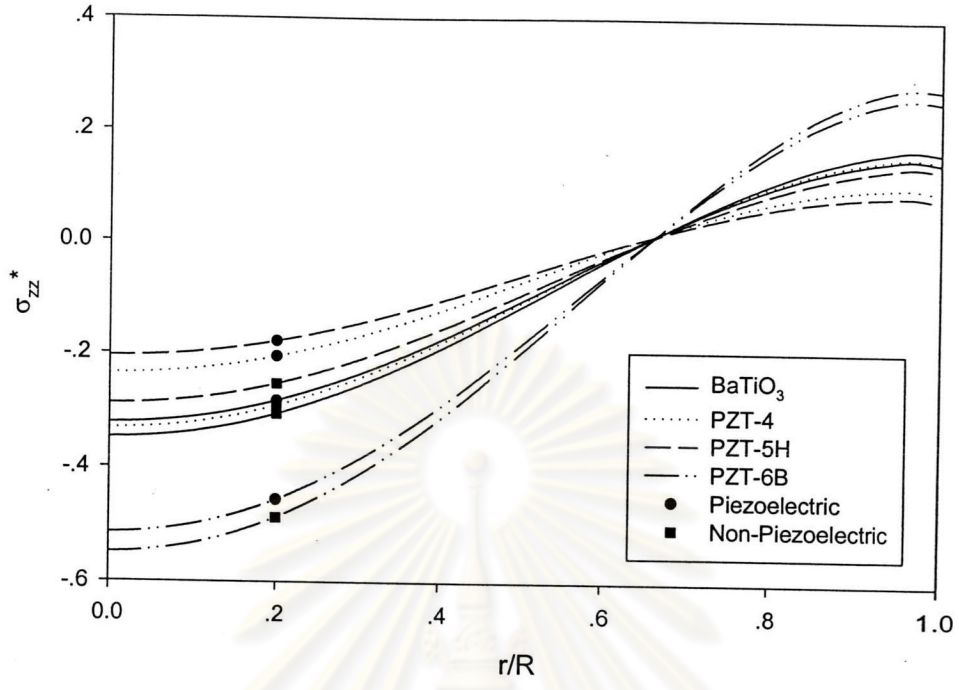

(a) Along r-axis at z=0.

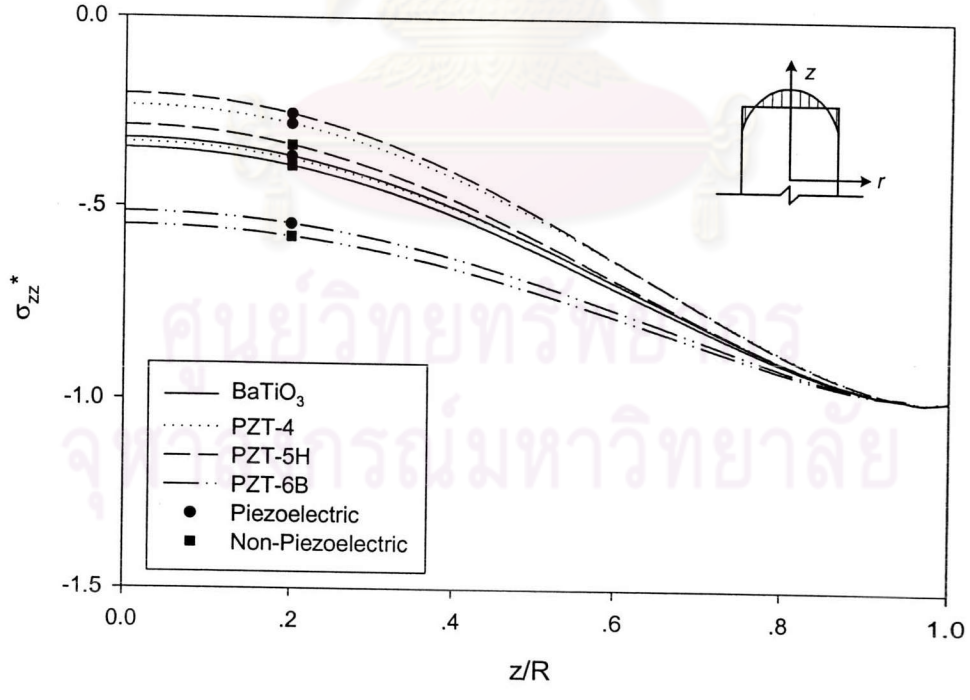

(b) Along z-axis at r=0.

Figure 4.13 Non-dimensional vertical stress profiles due to parabolic load for different materials.

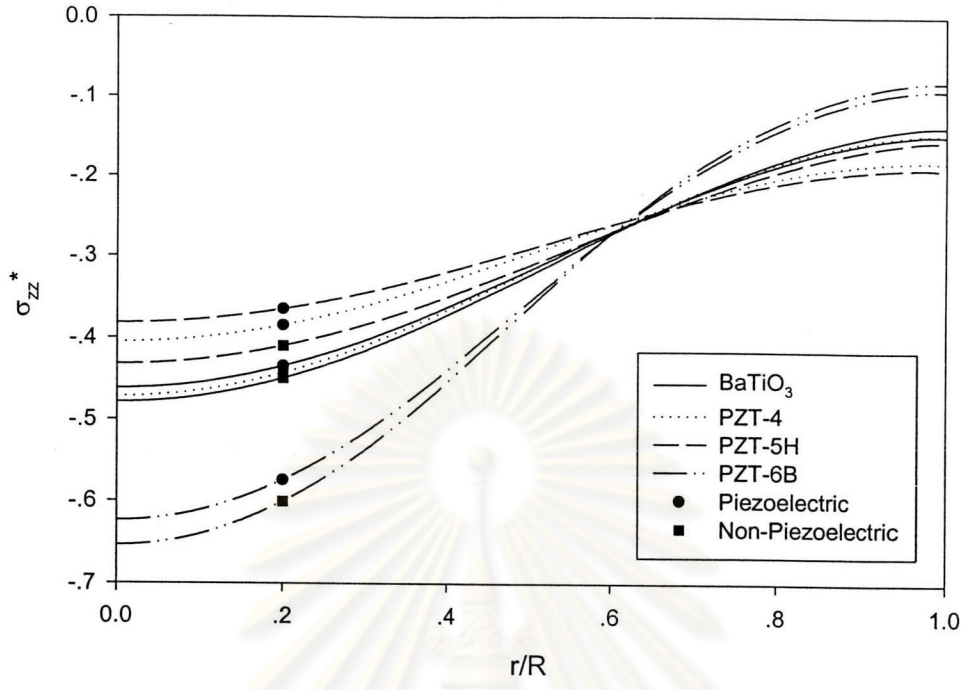

(a) Along r-axis at z=0.

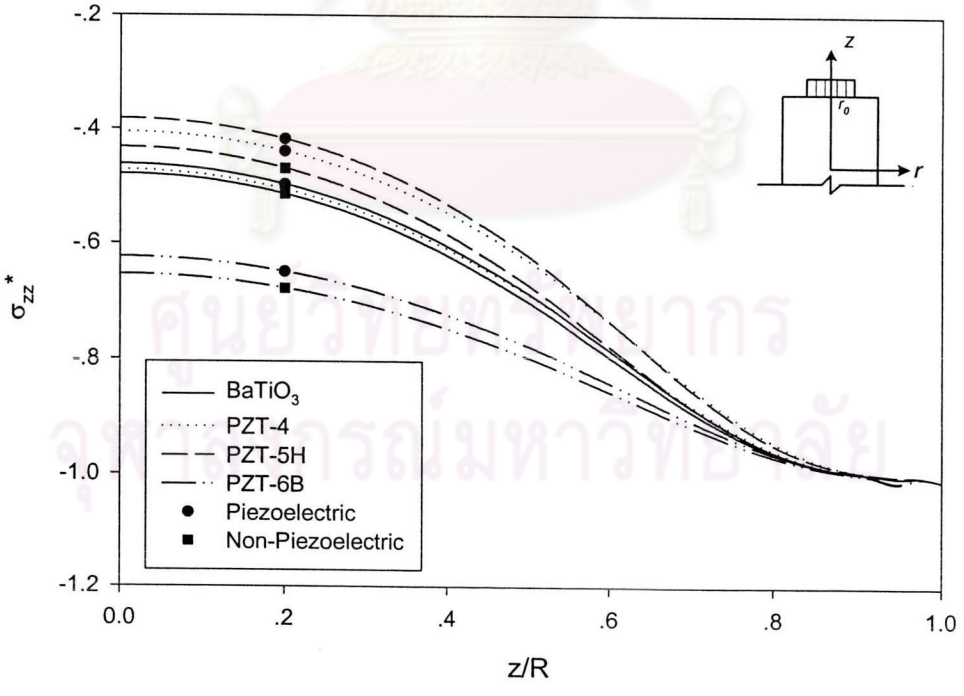

(b) Along z-axis at r=0.

Figure 4.14 Non-dimensional vertical stress profiles due to uniform load for different materials.

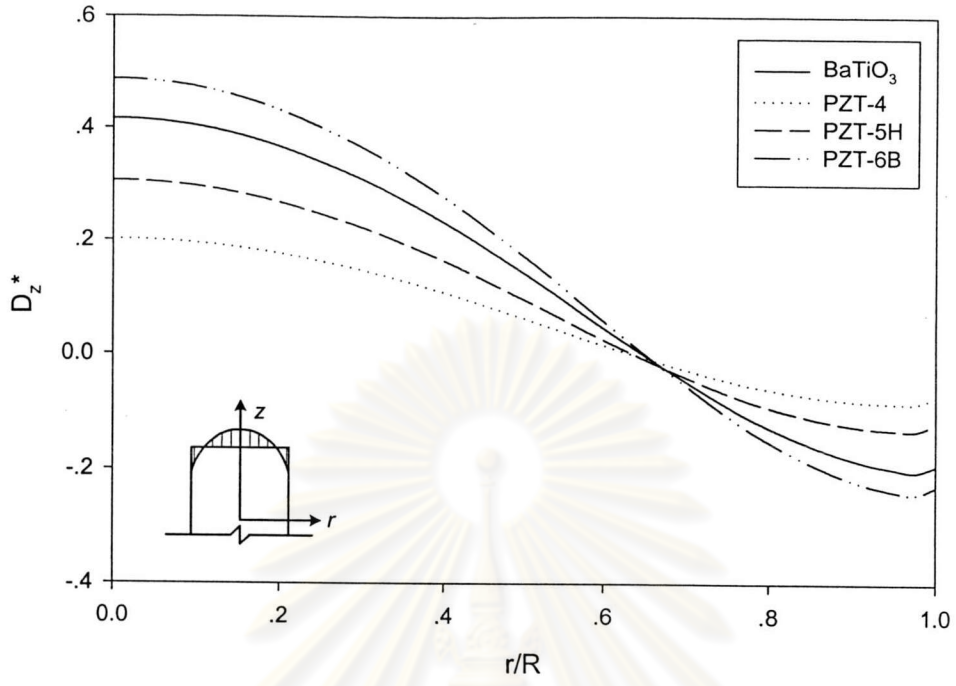

(a) Along r-axis at $z=0$.

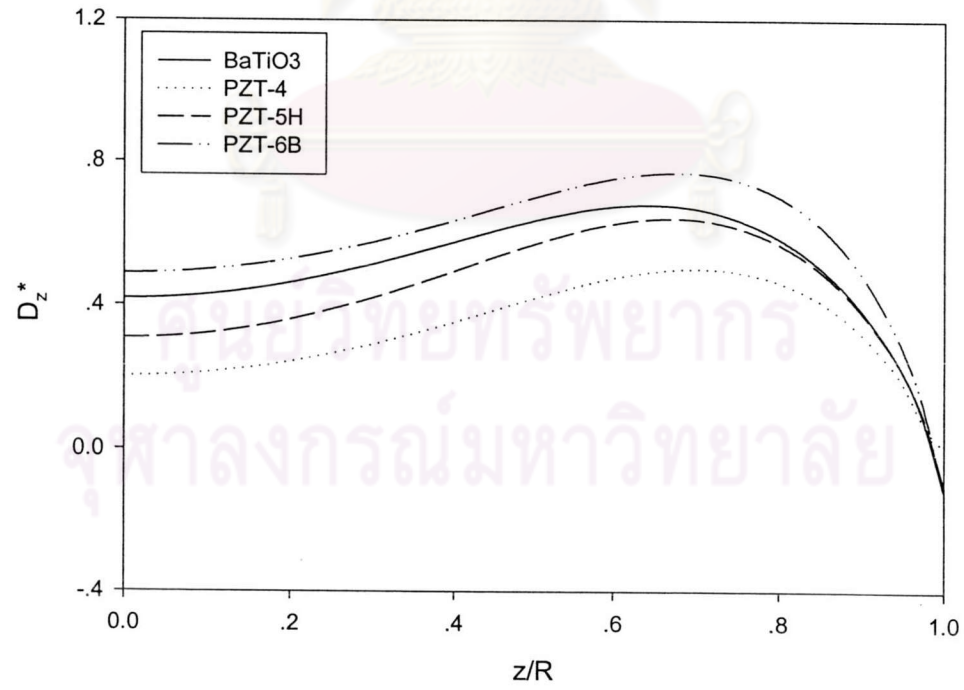

(b) Along z-axis at $r=0$.

Figure 4.15 Non-dimensional electric displacement profiles due to parabolic load for different materials.

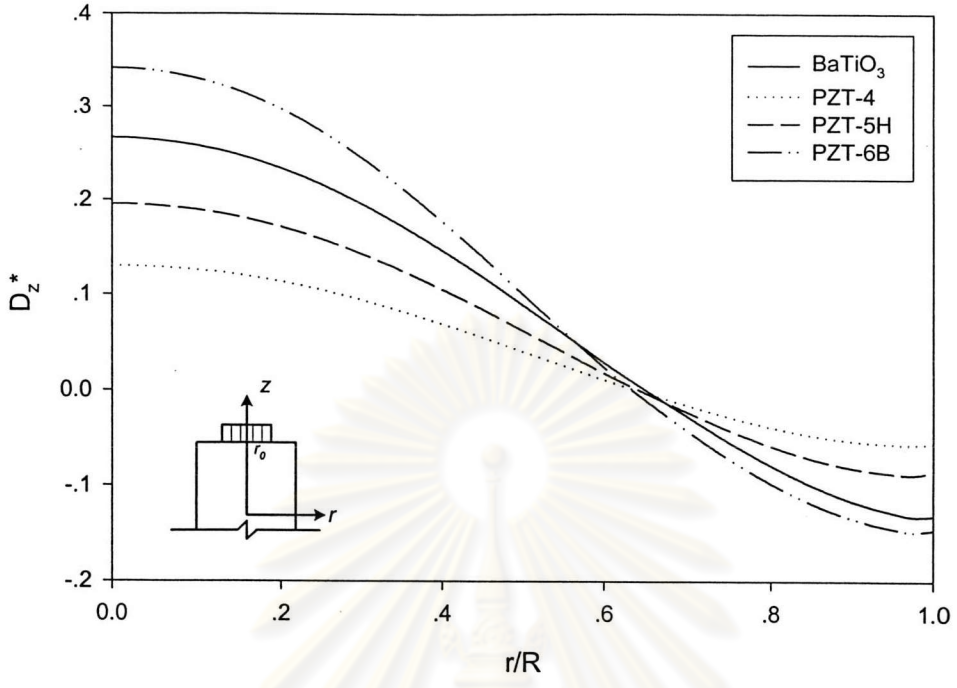

(a) Along r-axis at $z=0$.

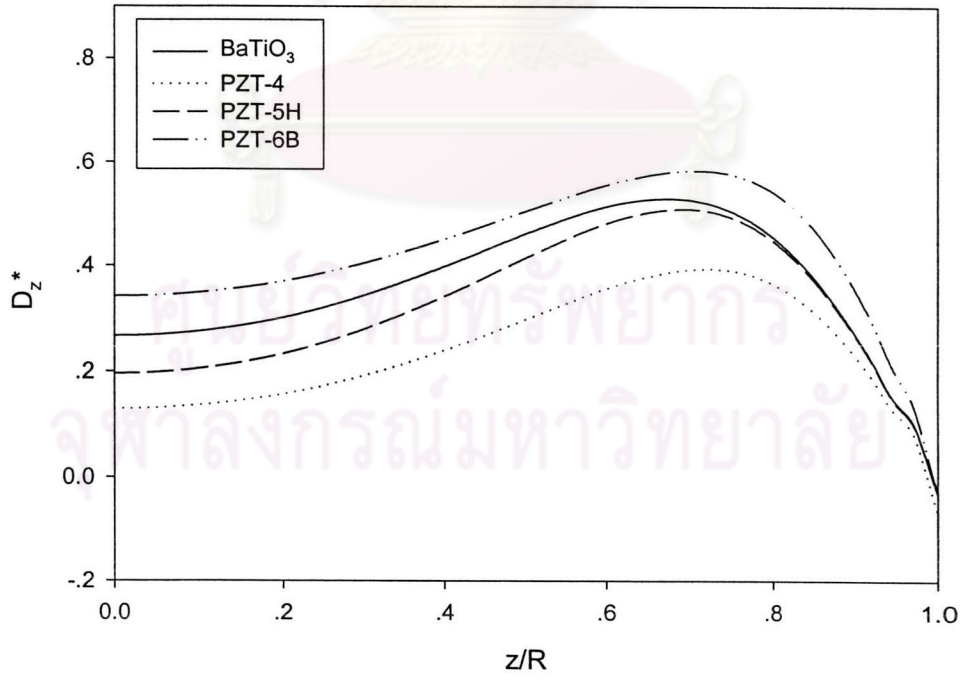

(b) Along z-axis at $r=0$.

Figure 4.16 Non-dimensional electric displacement profiles due to uniform load for different materials.

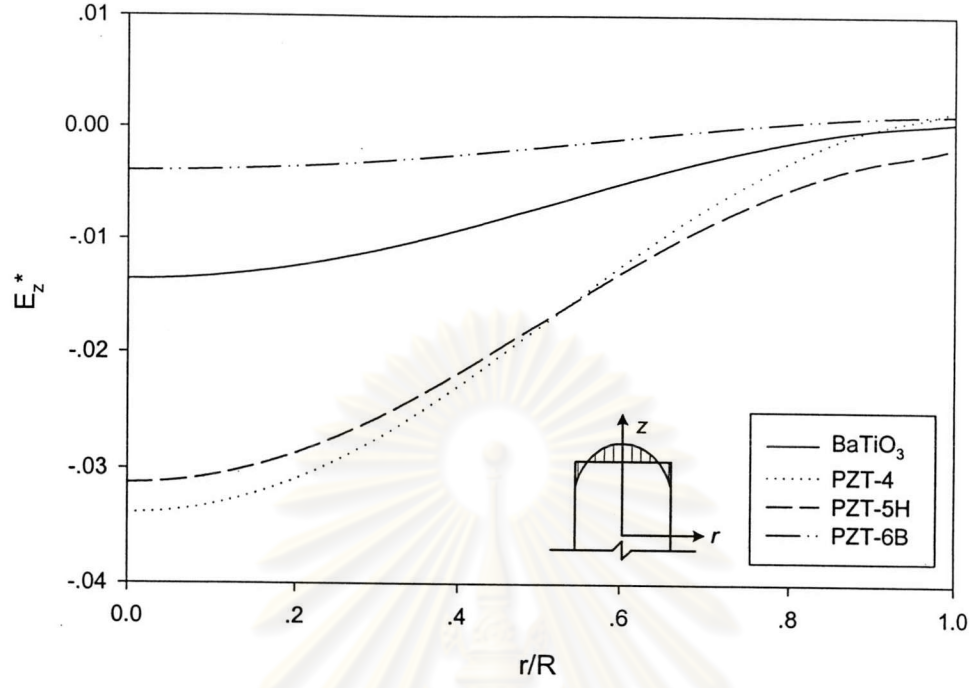

(a) Along r-axis at z=0.

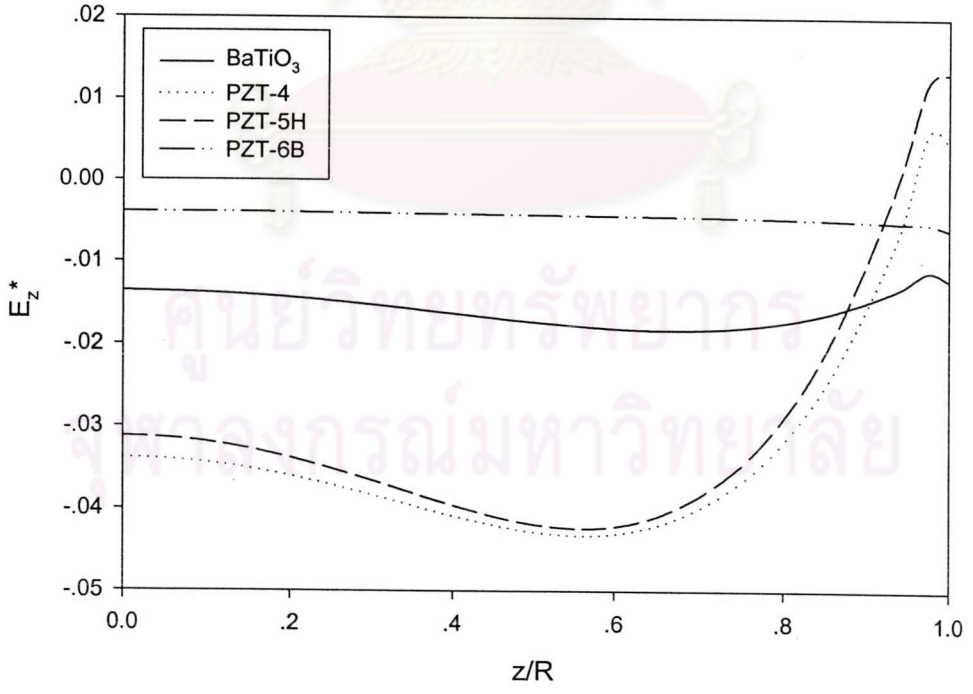

(b) Along z-axis at r=0.

Figure 4.17 Non-dimensional electric field profiles due to parabolic load for different materials.

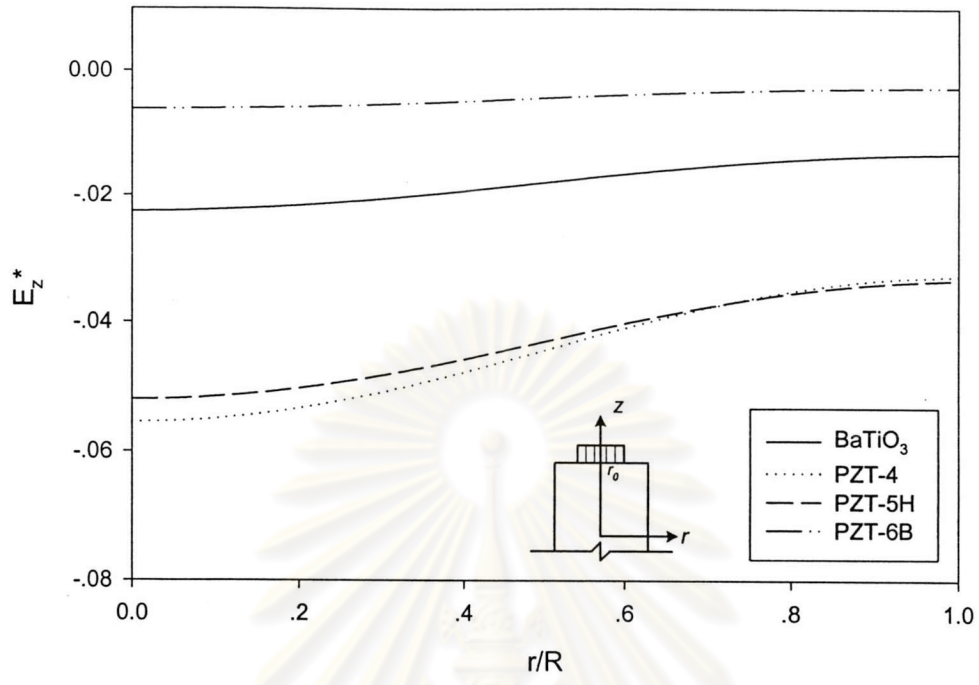

(a) Along r-axis at z=0.

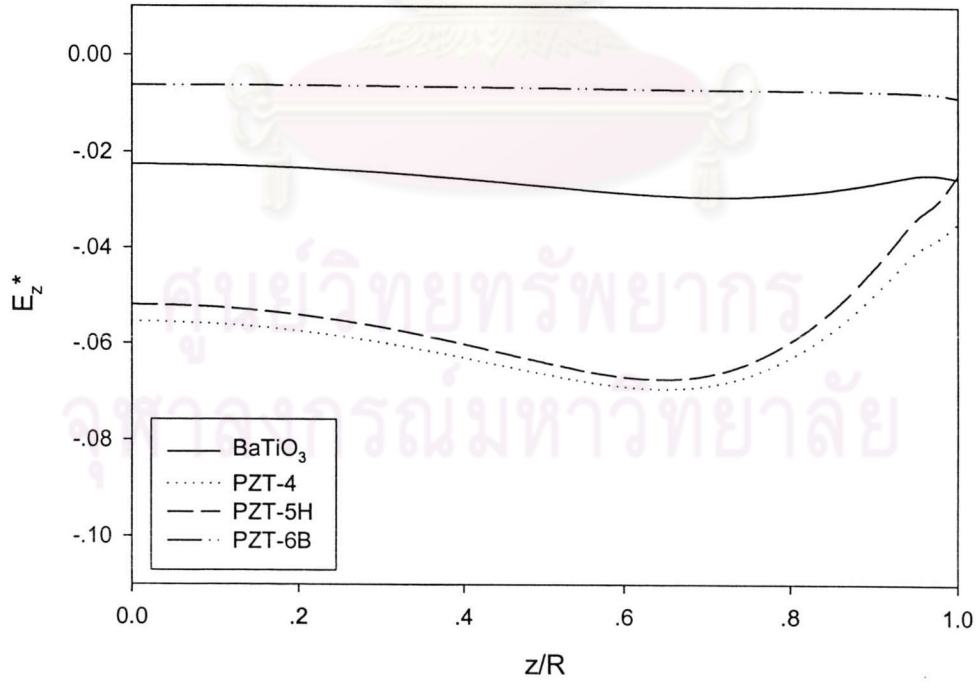

(b) Along z-axis at r=0.

Figure 4.18 Non-dimensional electric field profiles due to uniform load for different materials.

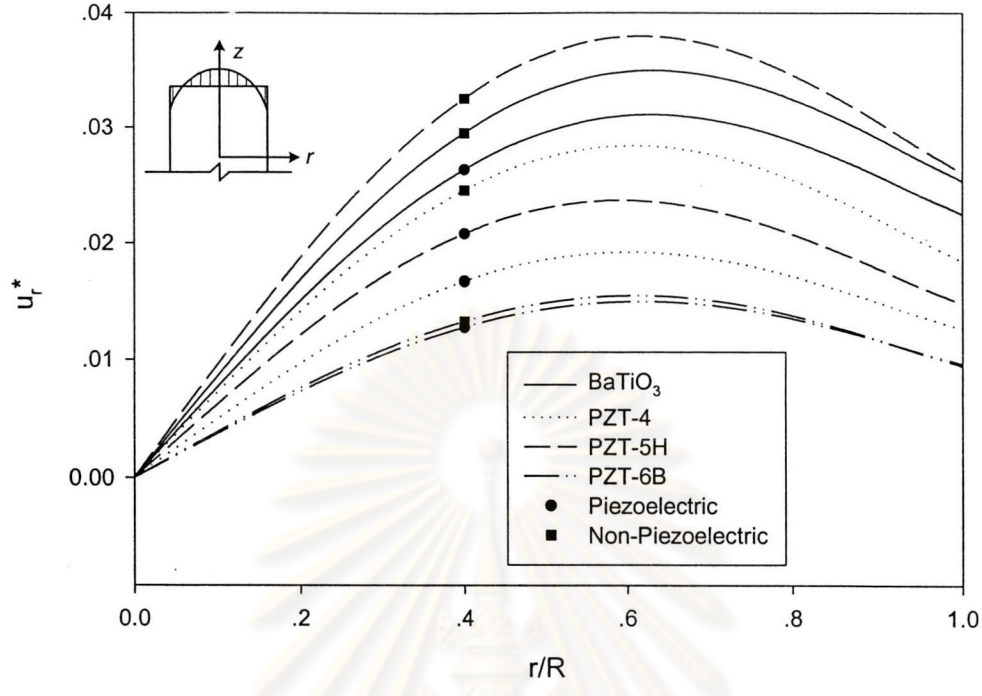

(a)

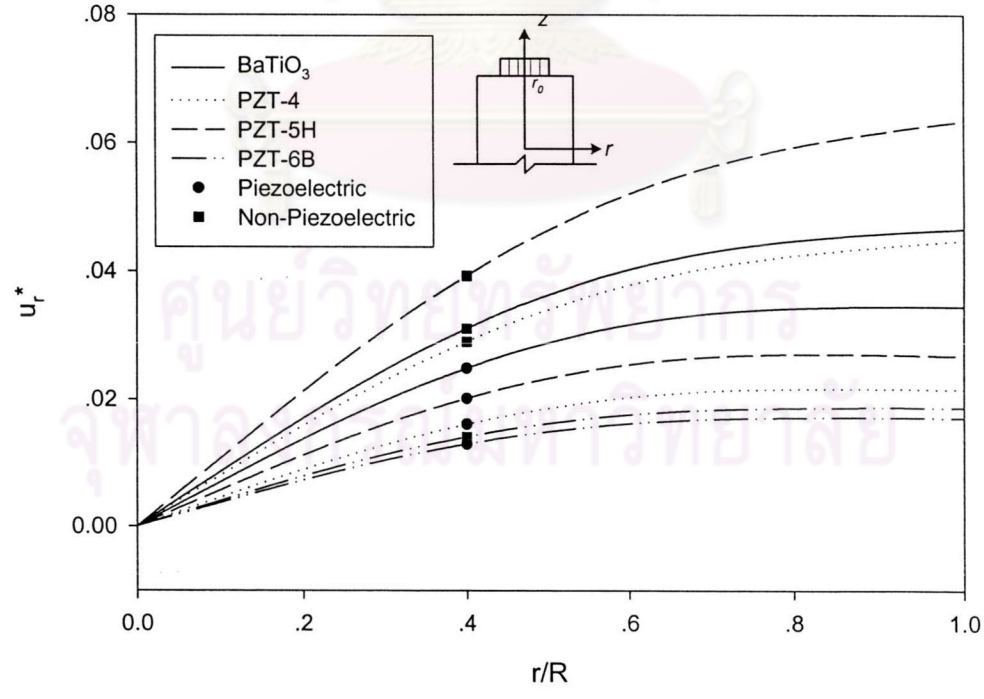

(b)

Figure 4.19 Non-dimensional radial displacement profiles along r-axis at $z=0$ due to (a) parabolic load and (b) uniform load for different materials.

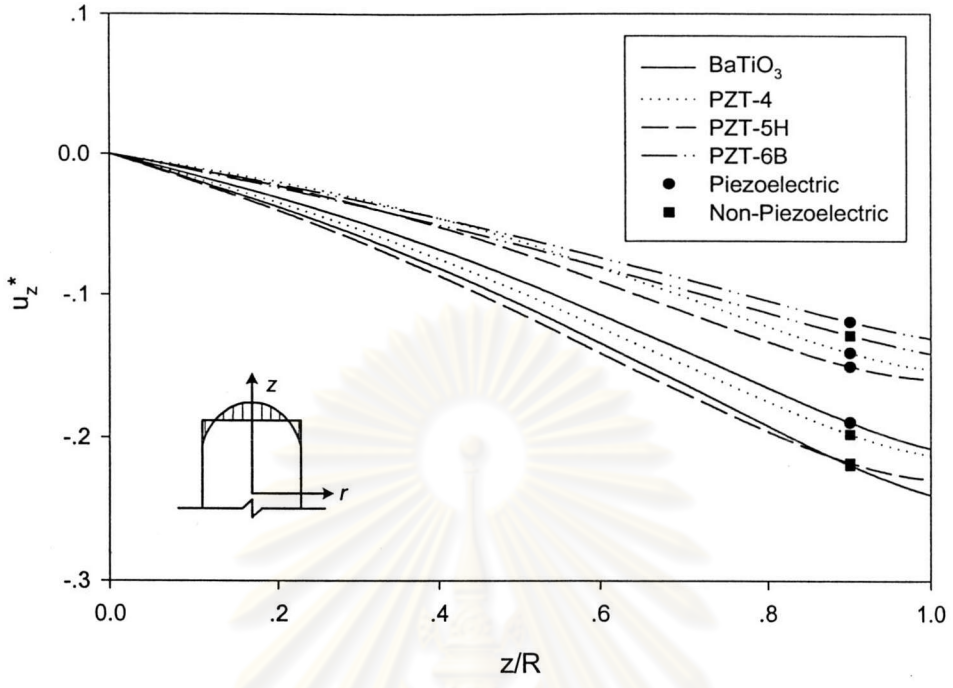

(a)

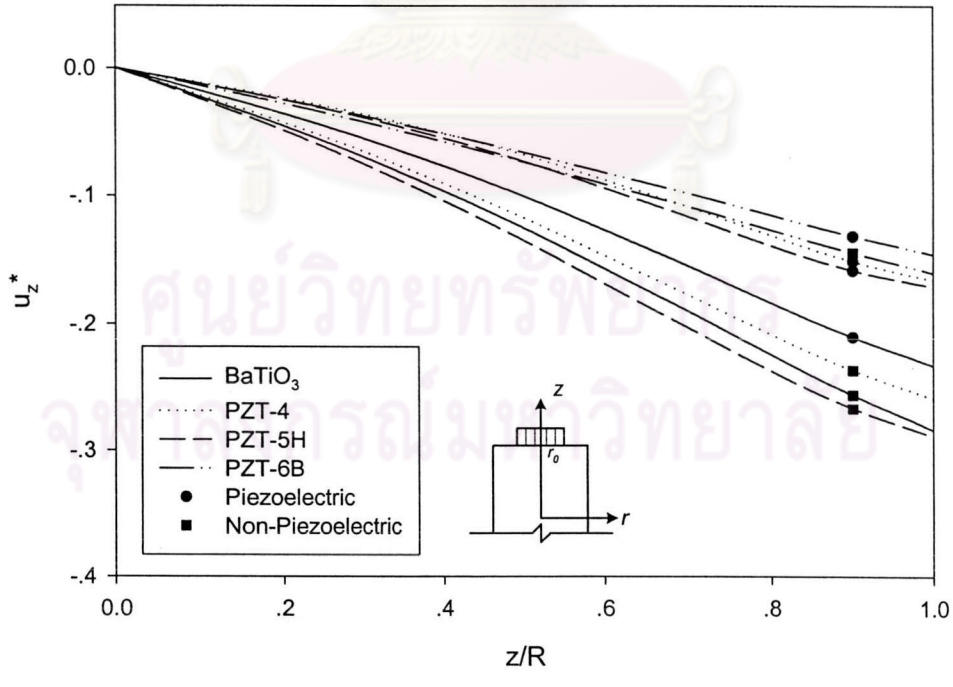

(b)

Figure 4.20 Non-dimensional vertical displacement profiles along z -axis at r =0 due to (a) parabolic load and (b) uniform load for different materials.

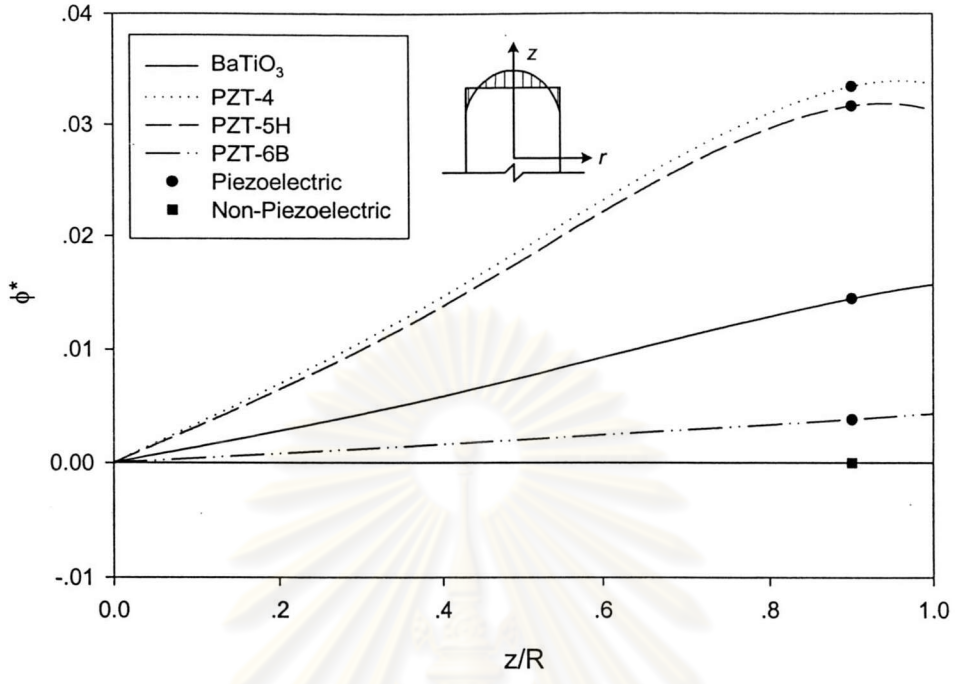

(a)

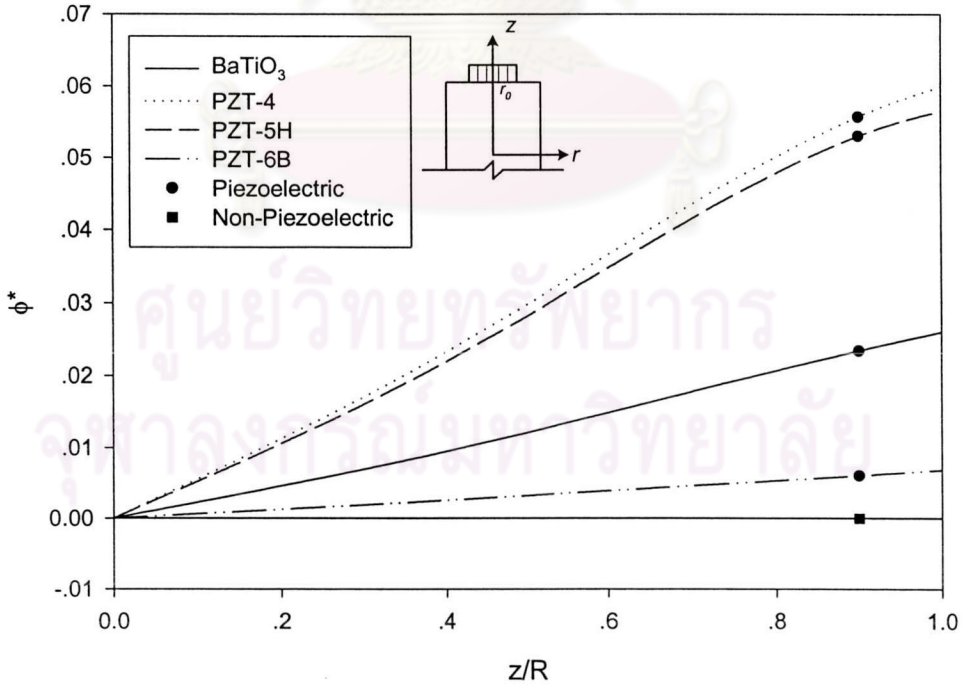

(b)

Figure 4.21 Non-dimensional electric potential profiles along z -axis at r =0 due to (a) parabolic load and (b) uniform load for different materials.

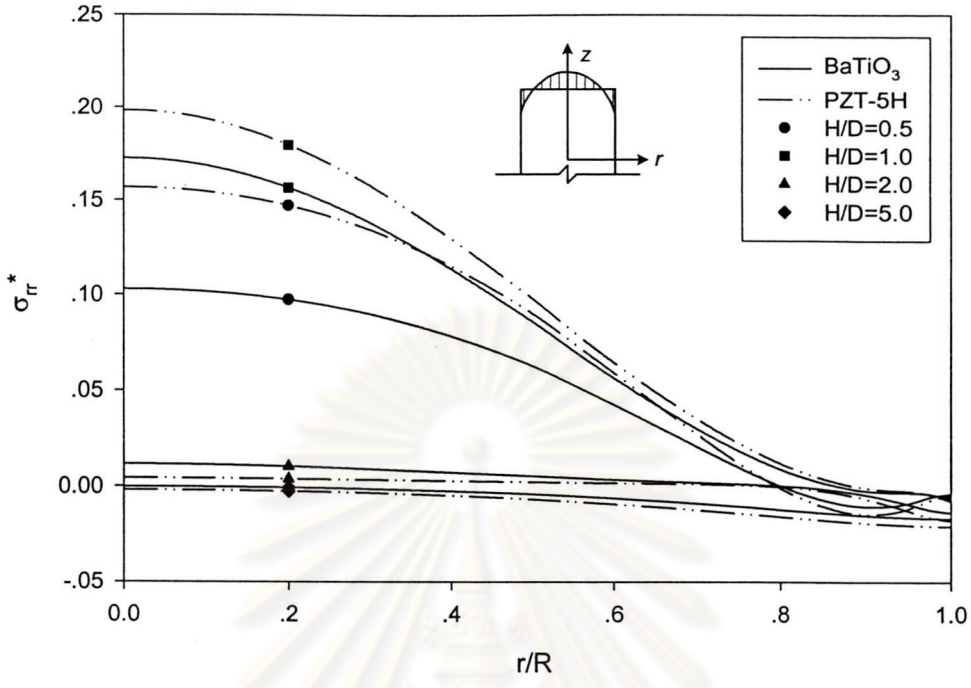

(a) Along r-axis at z=0.

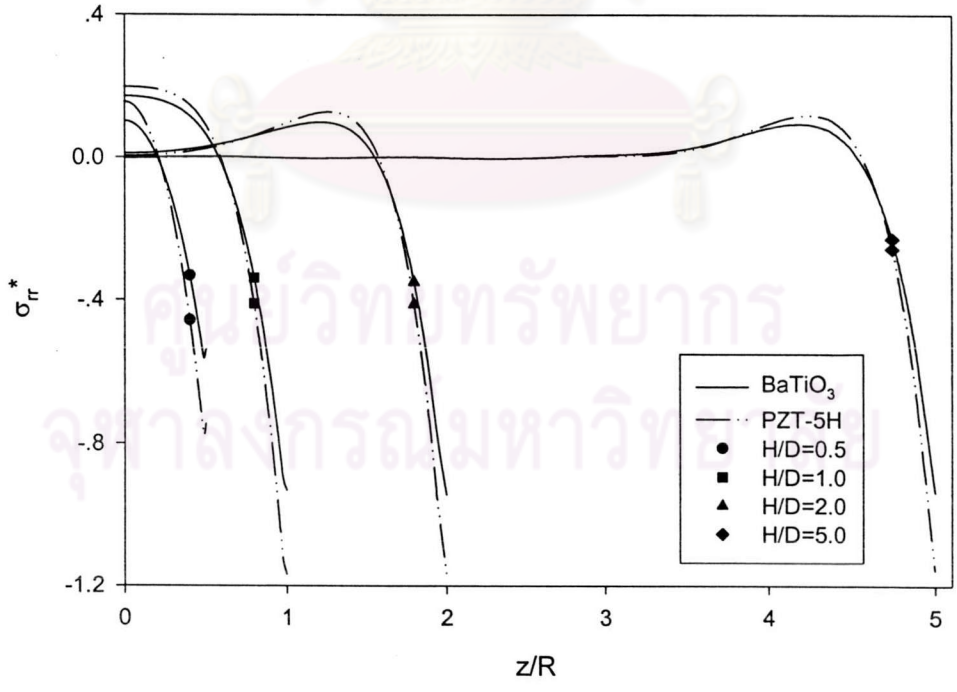

(b) Along z-axis at r=0.

Figure 4.22 Non-dimensional radial stress profiles due to parabolic load for various shape factors.

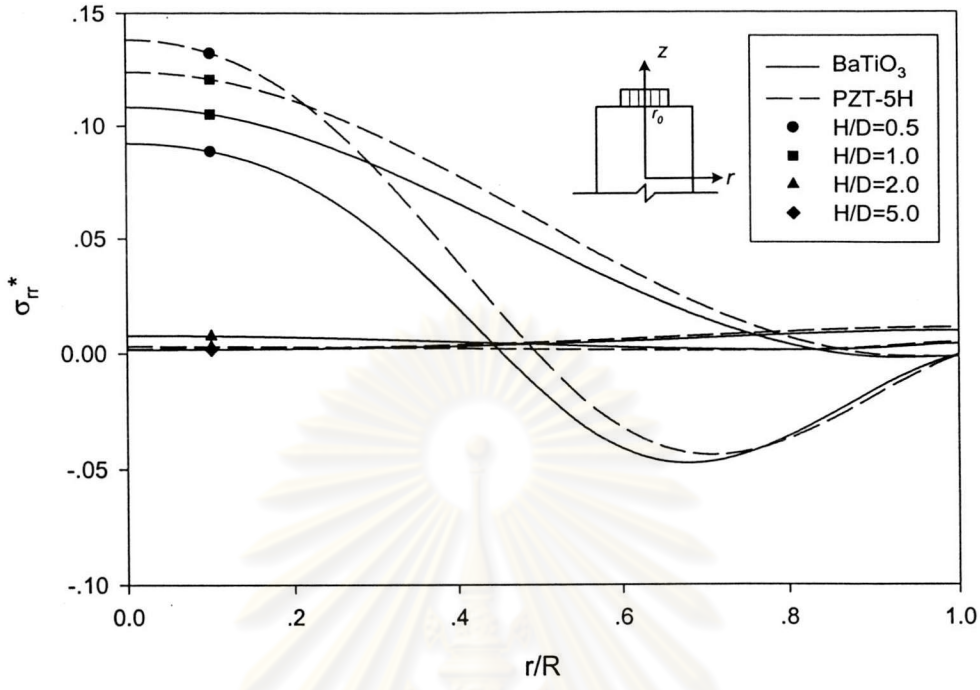

(a) Along r-axis at z=0.

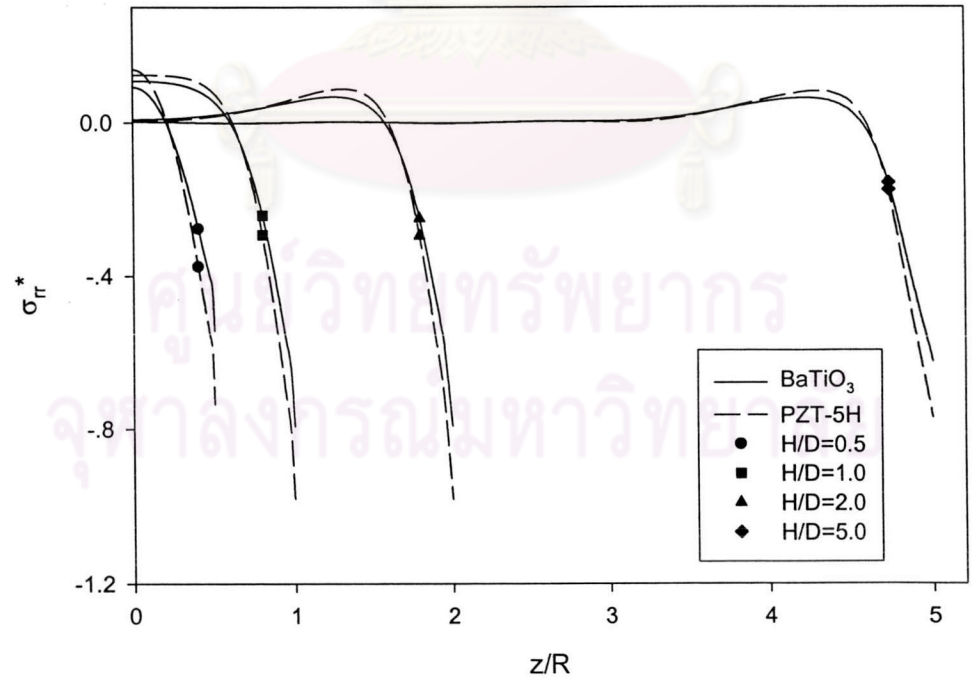

(b) Along z-axis at r=0.

Figure 4.23 Non-dimensional radial stress profiles due to uniform load for various shape factors.

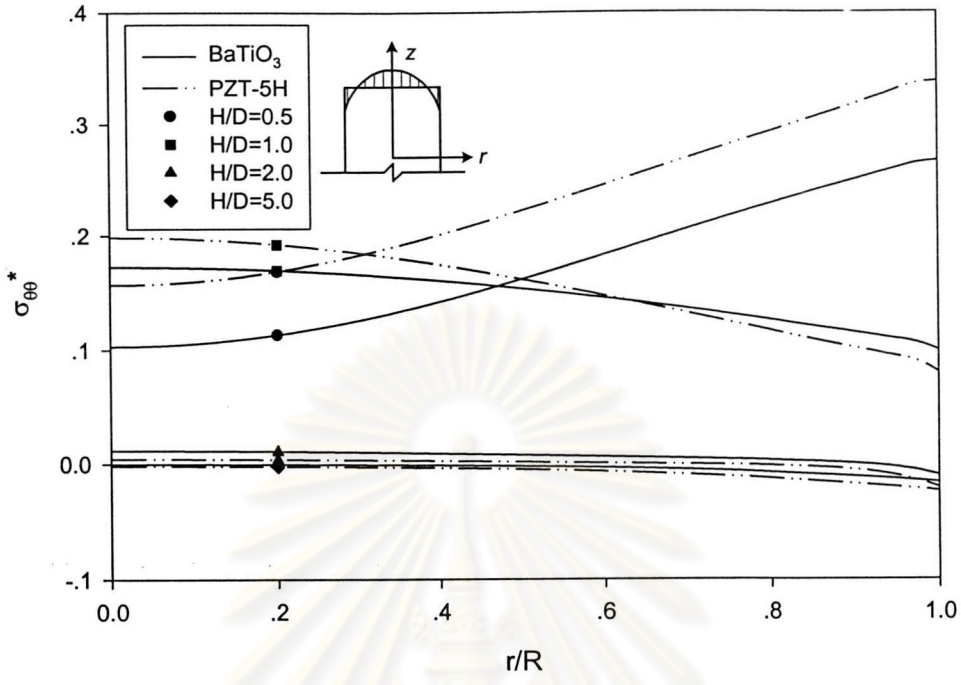

(a) Along r-axis at z=0.

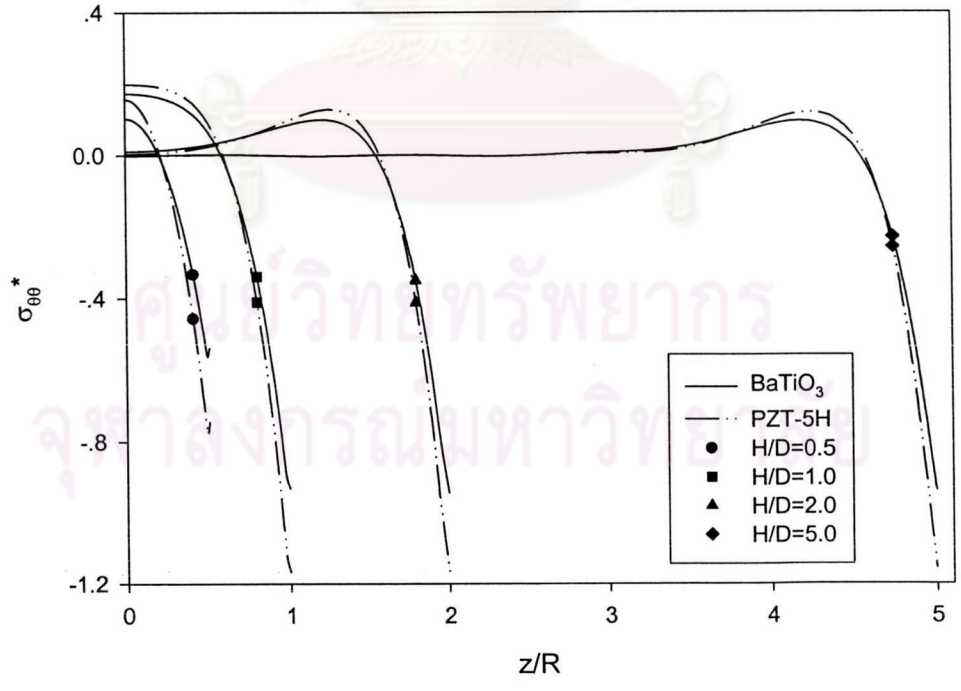

(b) Along z-axis at r=0.

Figure 4.24 Non-dimensional hoop stress profiles due to parabolic load for various shape factors.

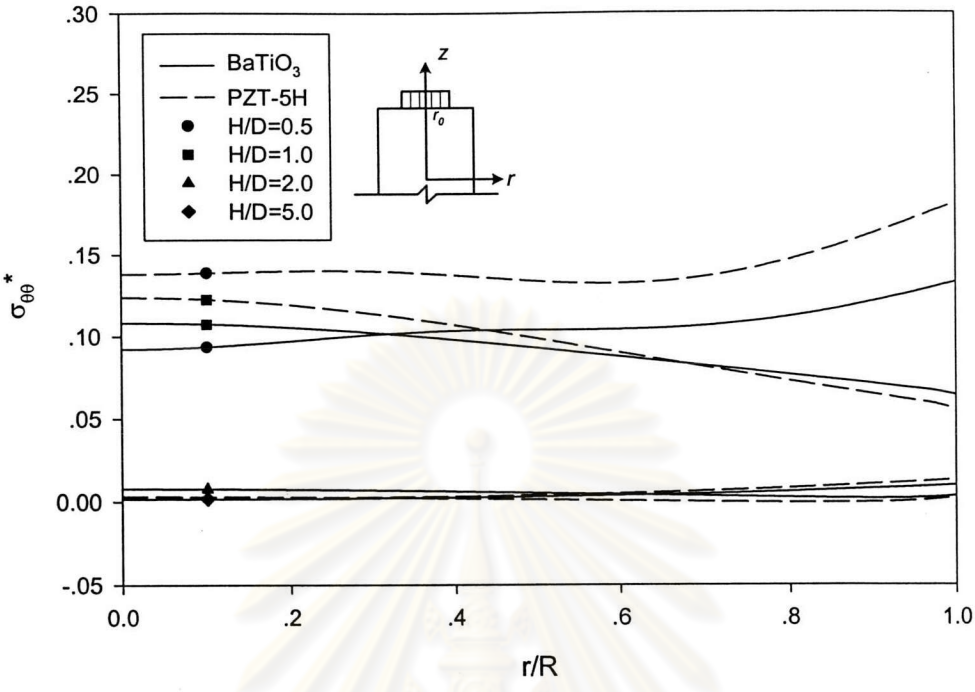

(a) Along r-axis at z=0.

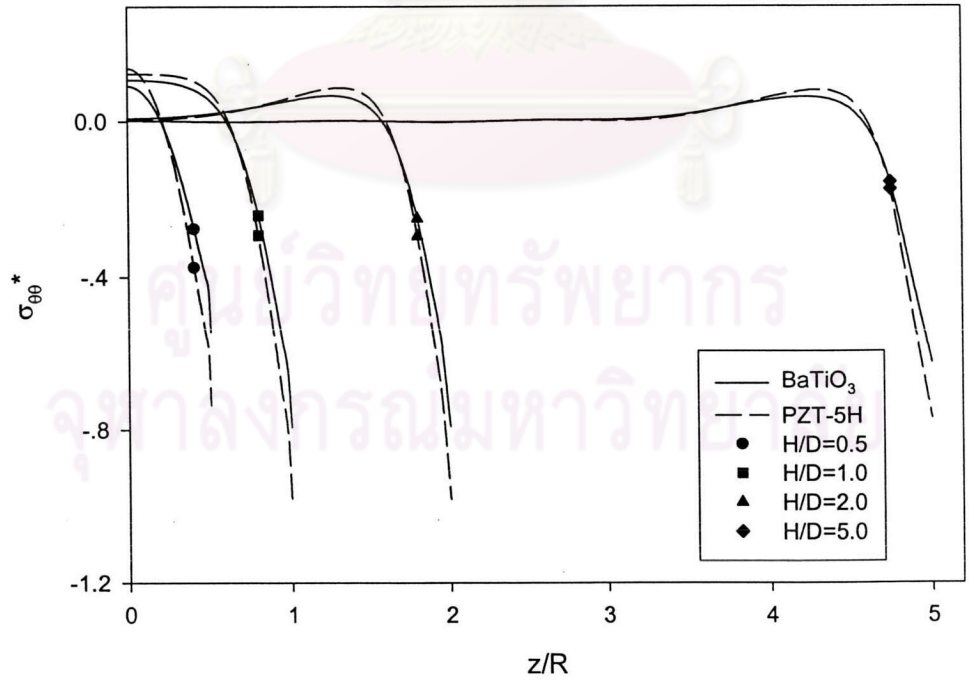

(b) Along z-axis at r=0.

Figure 4.25 Non-dimensional hoop stress profiles due to uniform load for various shape factors.

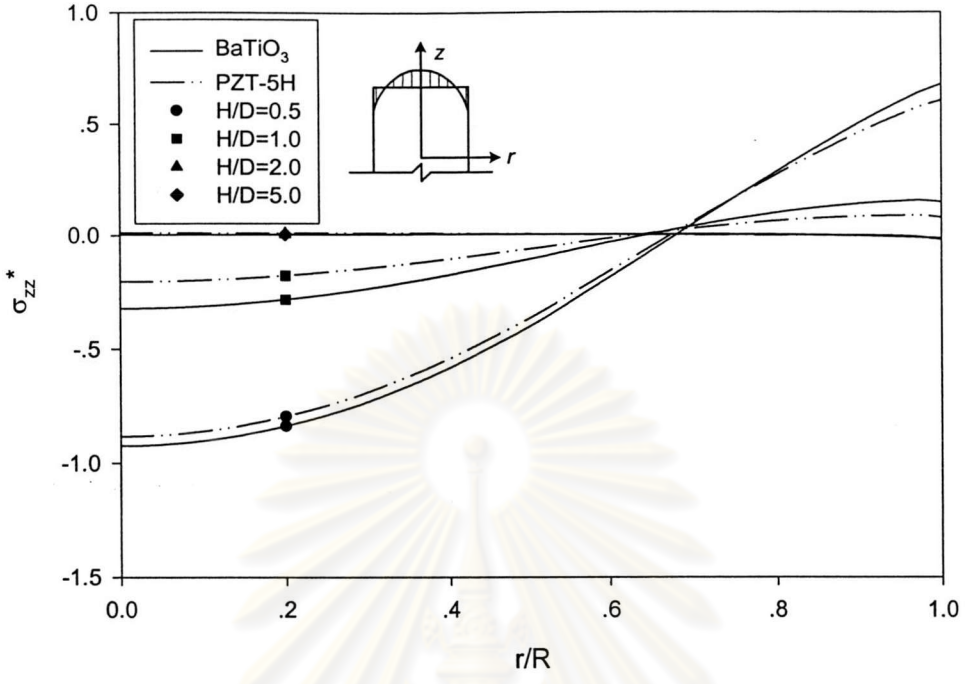

(a) Along r-axis at z=0.

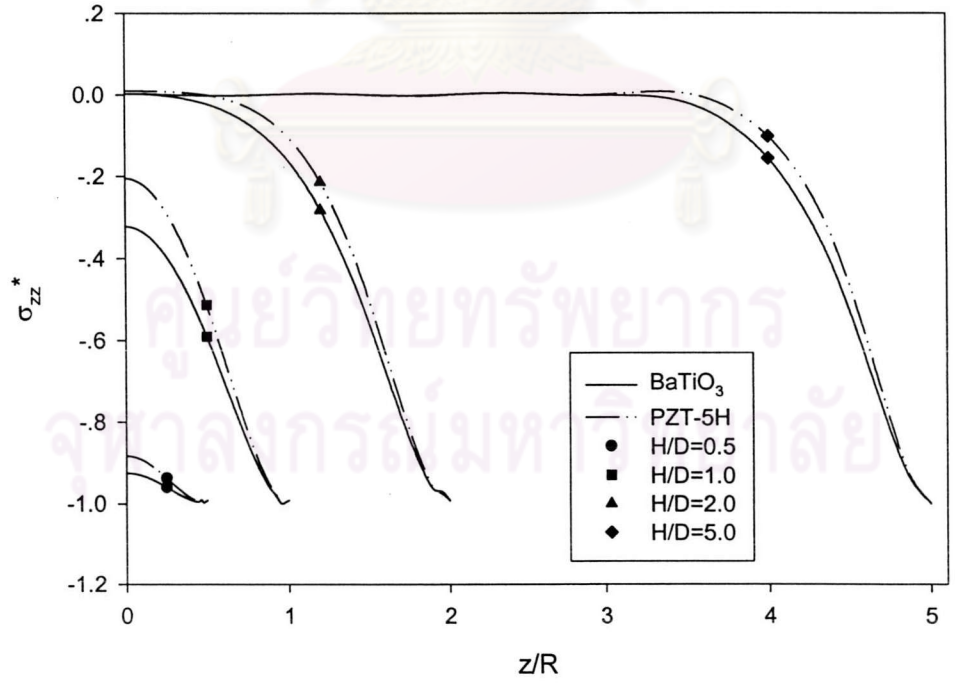

(b) Along z-axis at r=0.

Figure 4.26 Non-dimensional vertical stress profiles due to parabolic load for various shape factors.

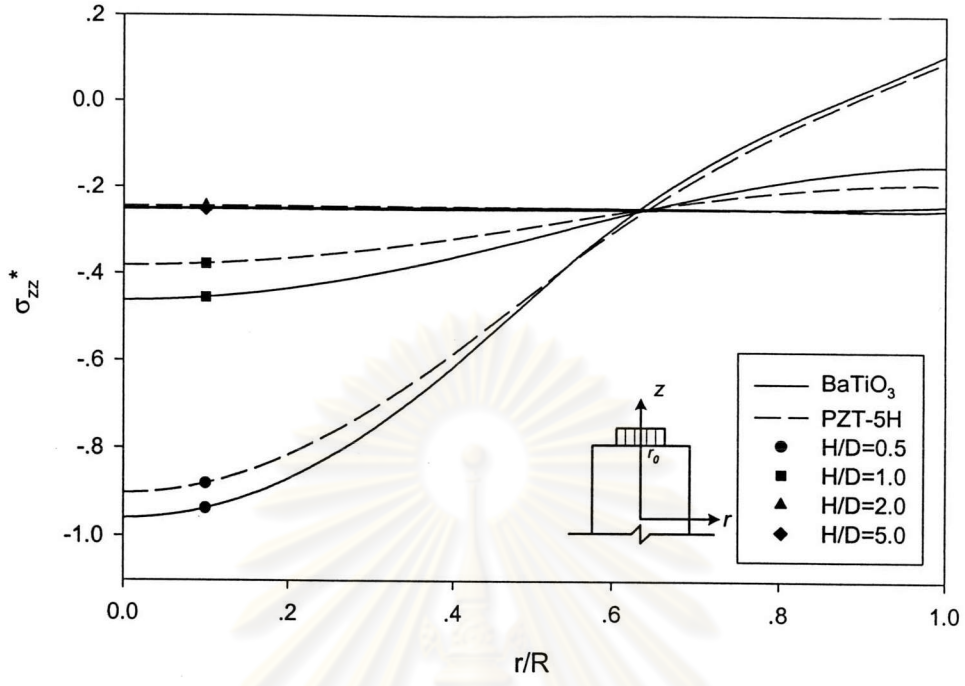

(a) Along r-axis at z=0.

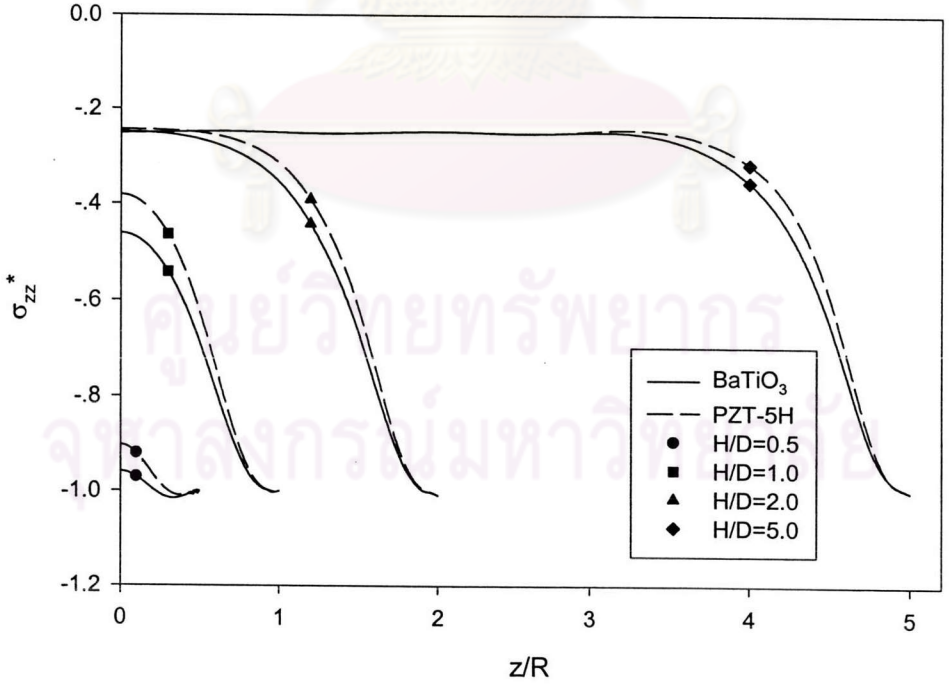

(b) Along z-axis at r=0.

Figure 4.27 Non-dimensional vertical stress profiles due to uniform load for various shape factors.

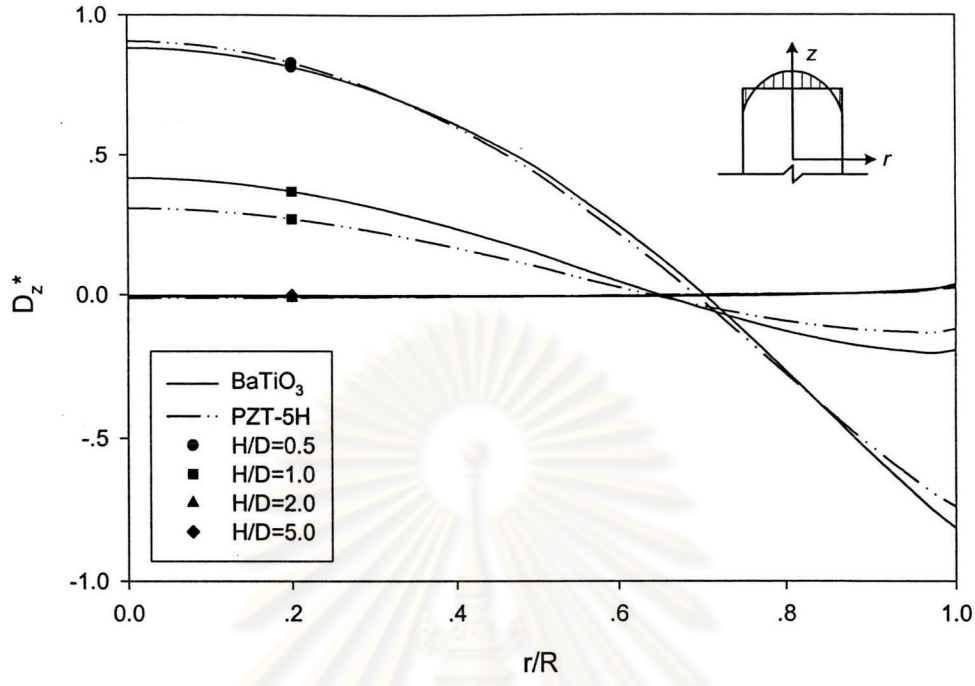

(a) Along r-axis at z=0.

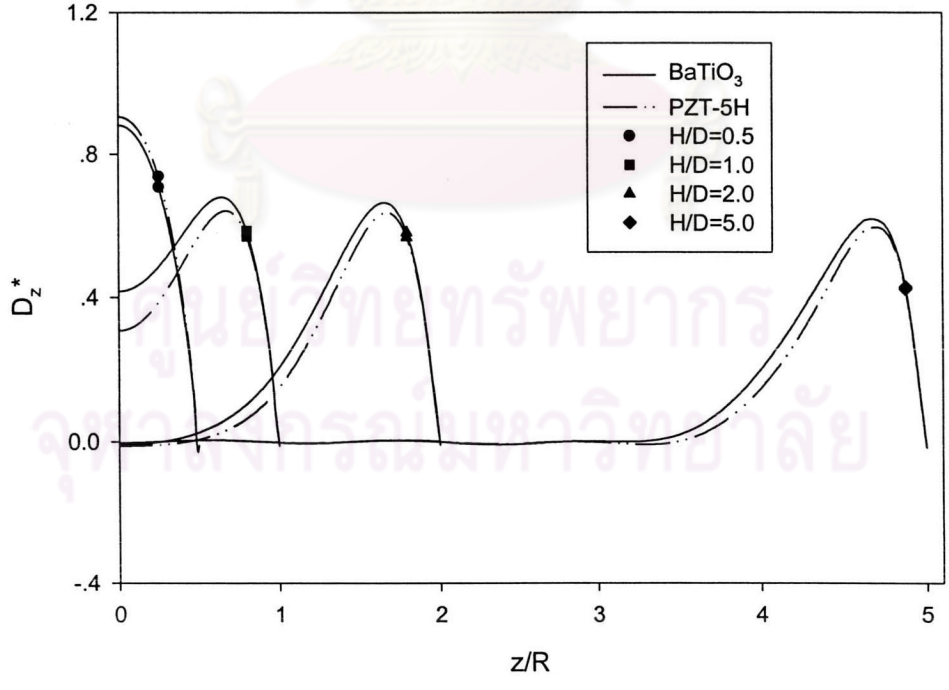

(b) Along z-axis at r=0.

Figure 4.28 Non-dimensional electric displacement profiles due to parabolic load for various shape factors.

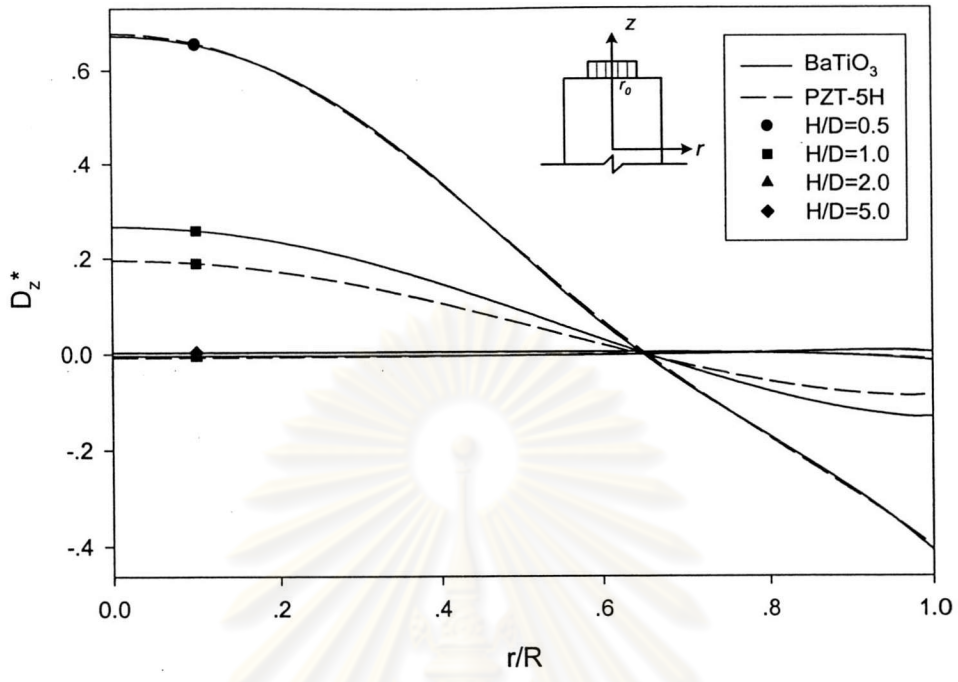

(a) Along r-axis at z=0.

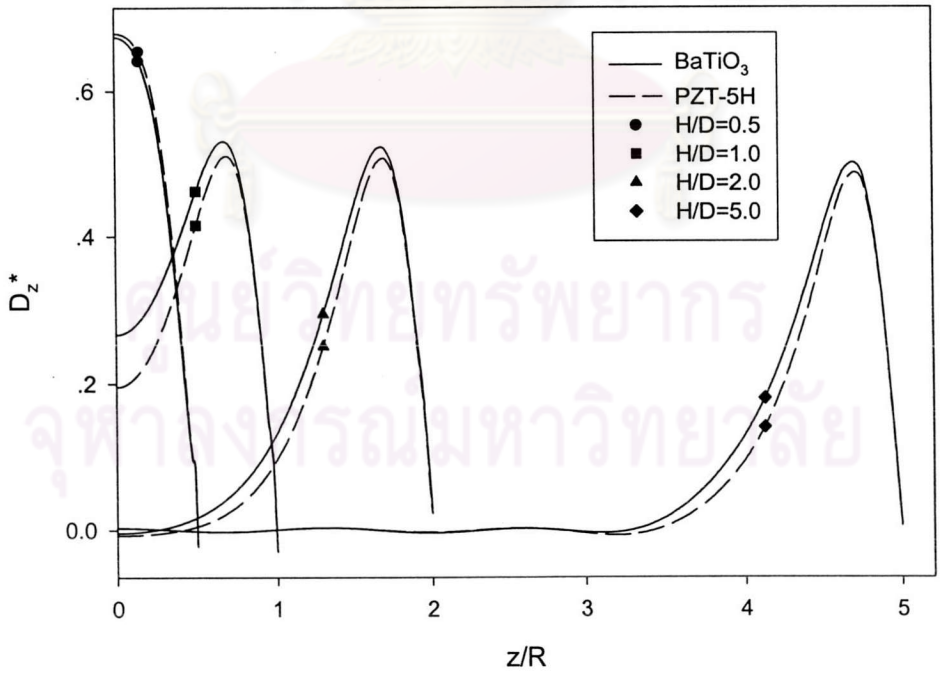

(b) Along z-axis at r=0.

Figure 4.29 Non-dimensional electric displacement profiles due to uniform load for various shape factors.

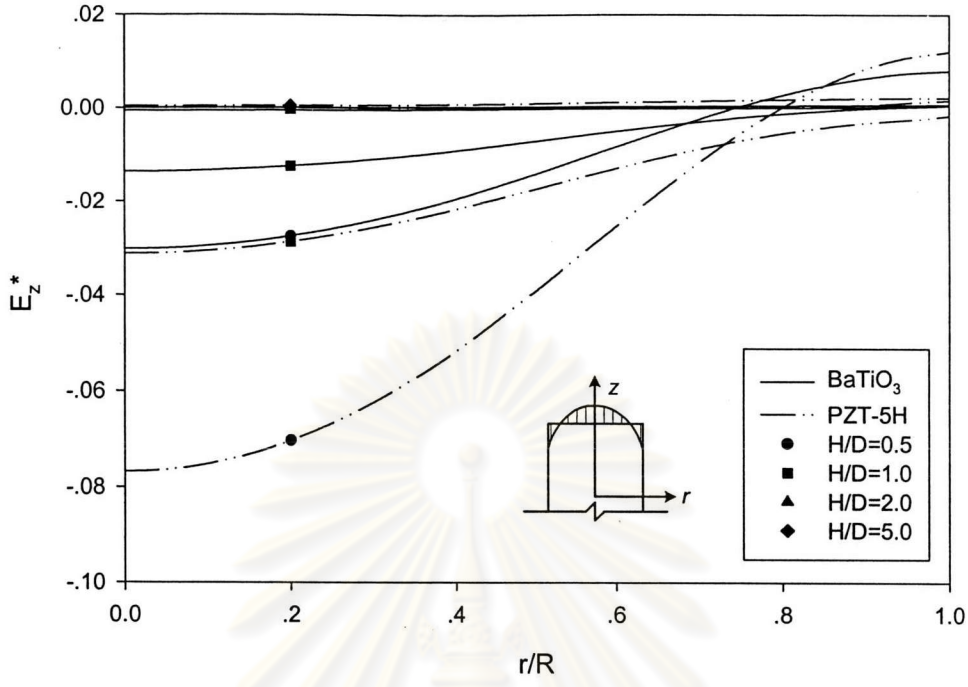

(a) Along r-axis at z=0.

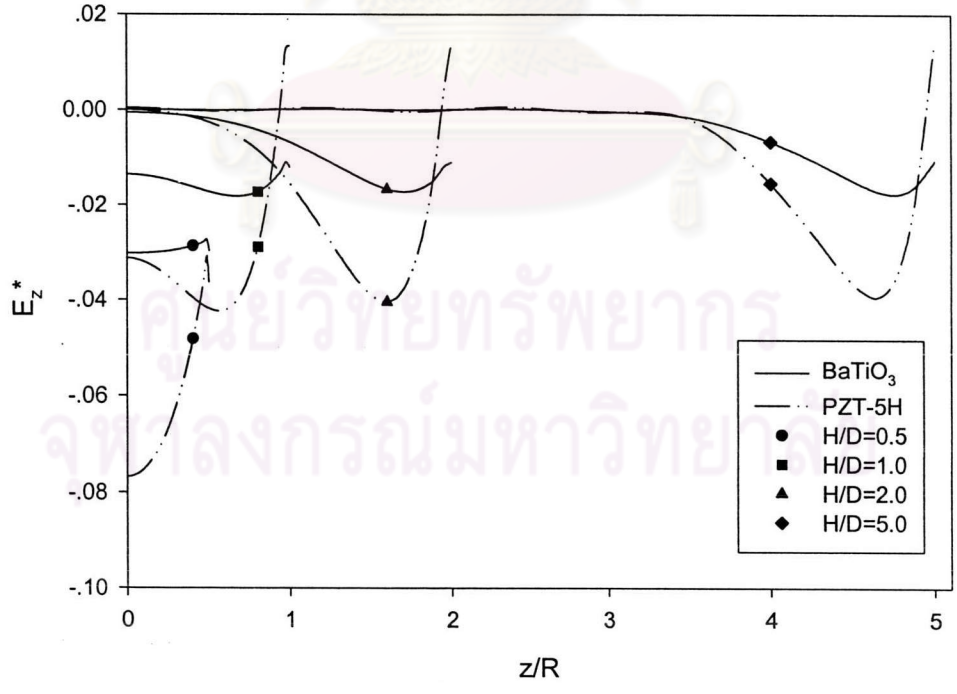

(b) Along z-axis at r=0.

Figure 4.30 Non-dimensional electric field profiles due to parabolic load for various shape factors.

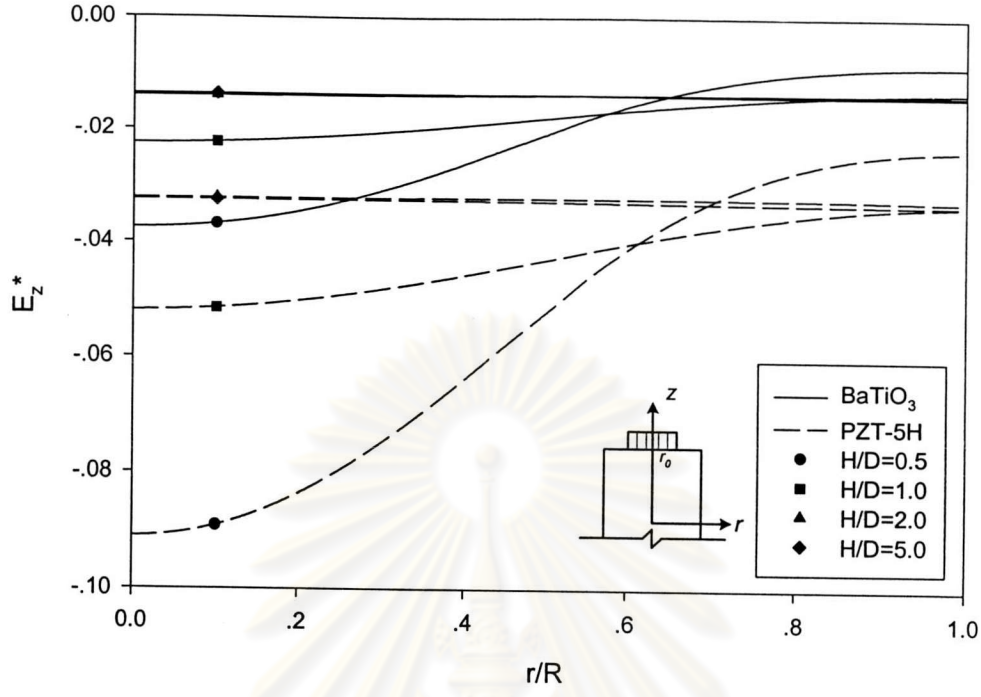

(a) Along r-axis at z=0.

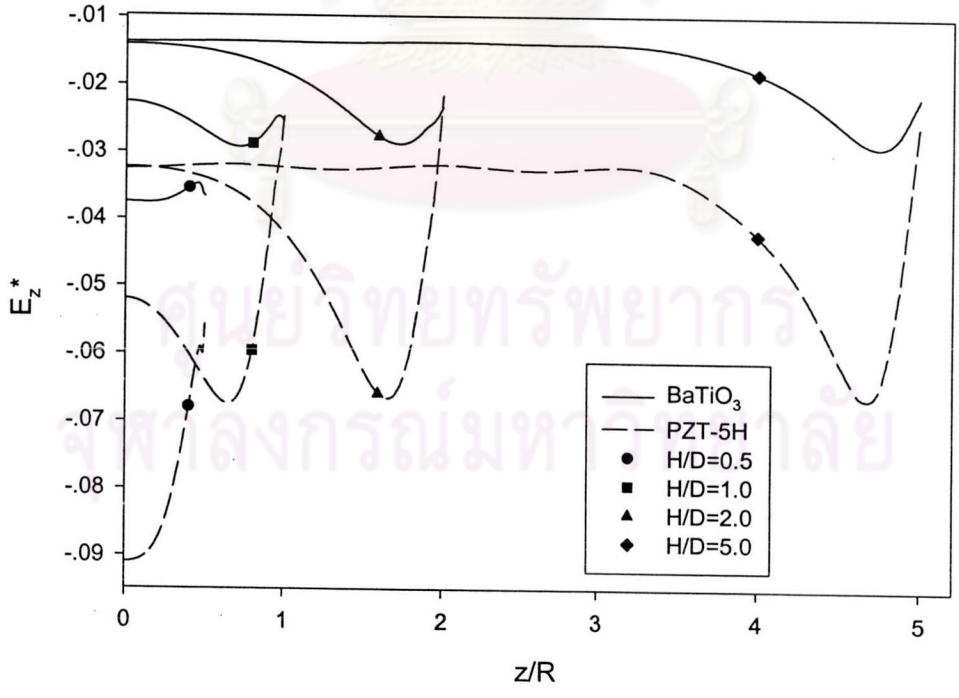

(b) Along z-axis at r=0.

Figure 4.31 Non-dimensional electric field profiles due to uniform load for various shape factors.

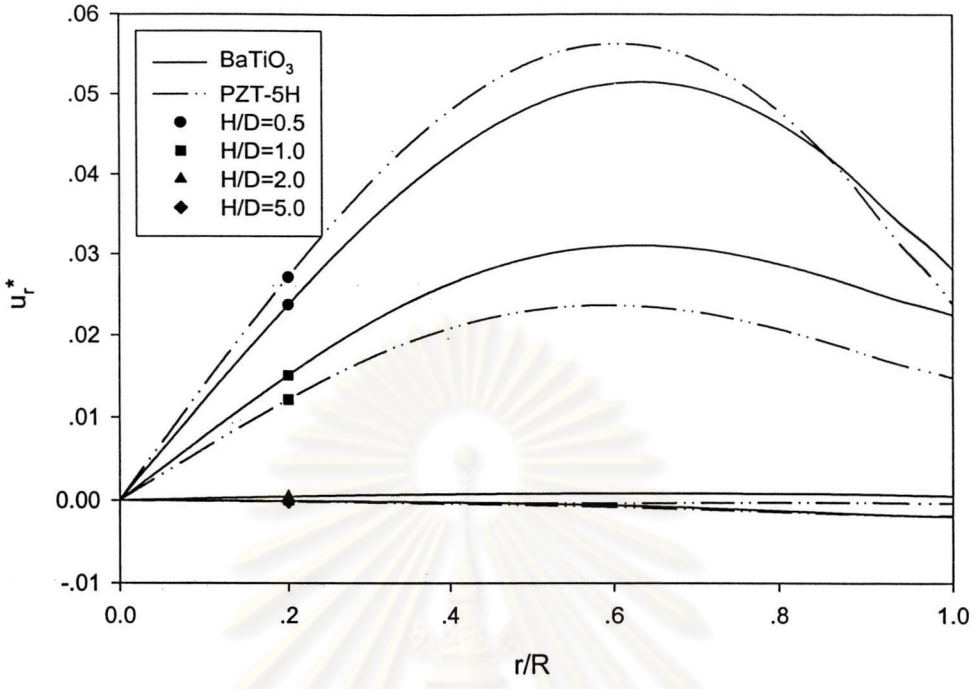

(a)

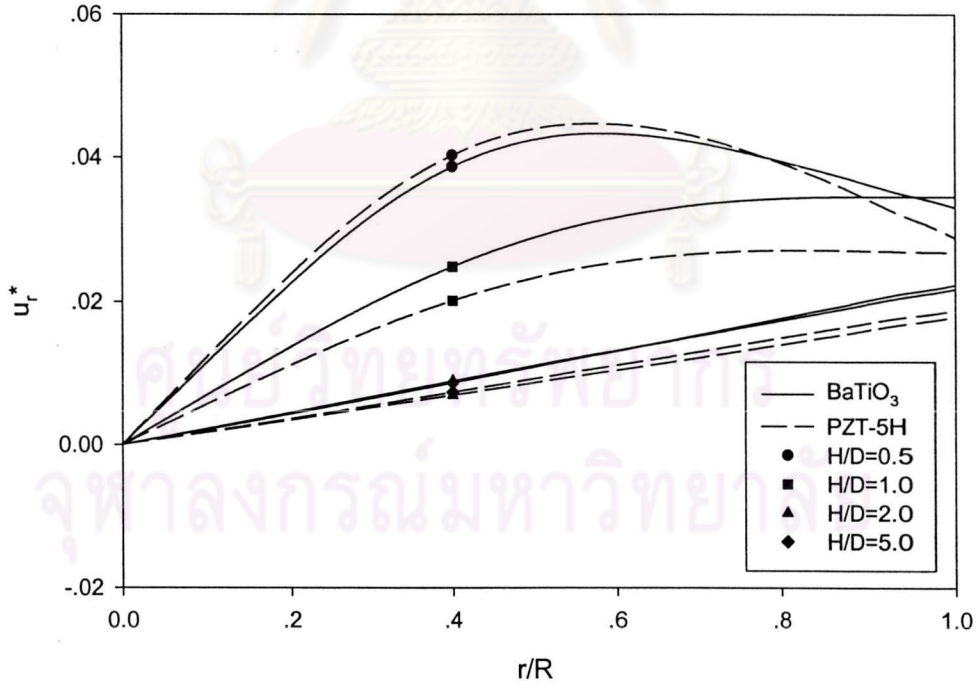

(b)

Figure 4.32 Non-dimensional radial displacement profiles along the r-axis at $z=0$ due to (a) parabolic load and (b) uniform load for various shape factors.

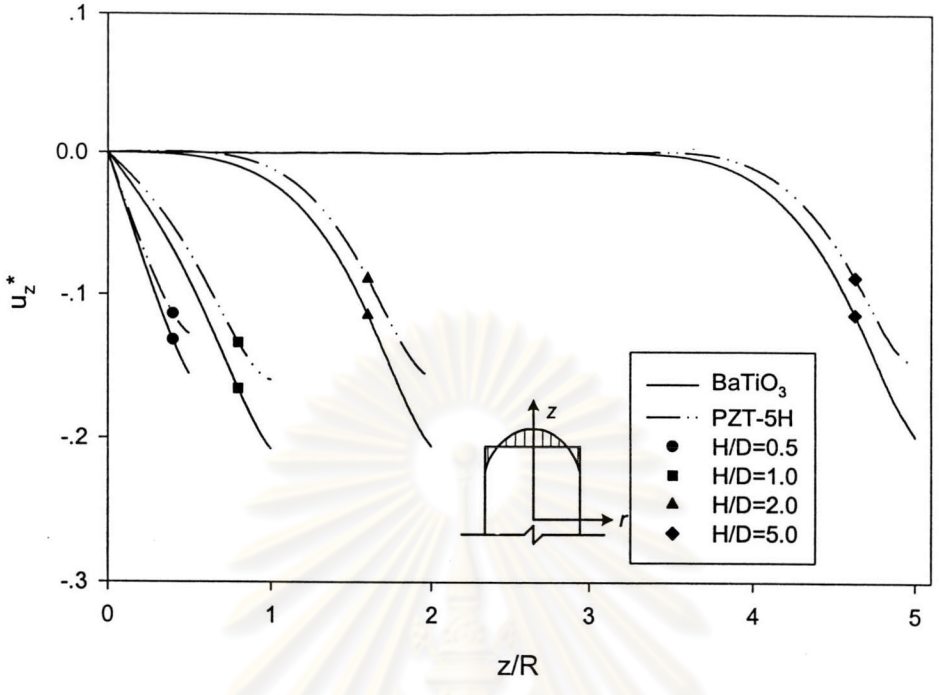

(a)

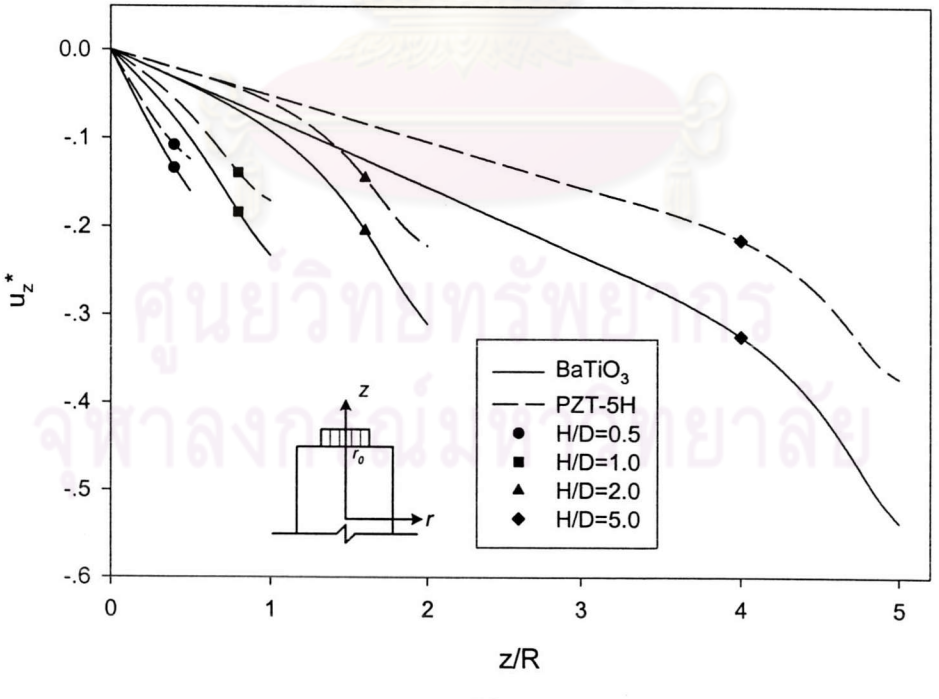

(b)

Figure 4.33 Non-dimensional vertical displacement profiles along the z-axis at $r=0$ due to (a) parabolic load and (b) uniform load for various shape factors.

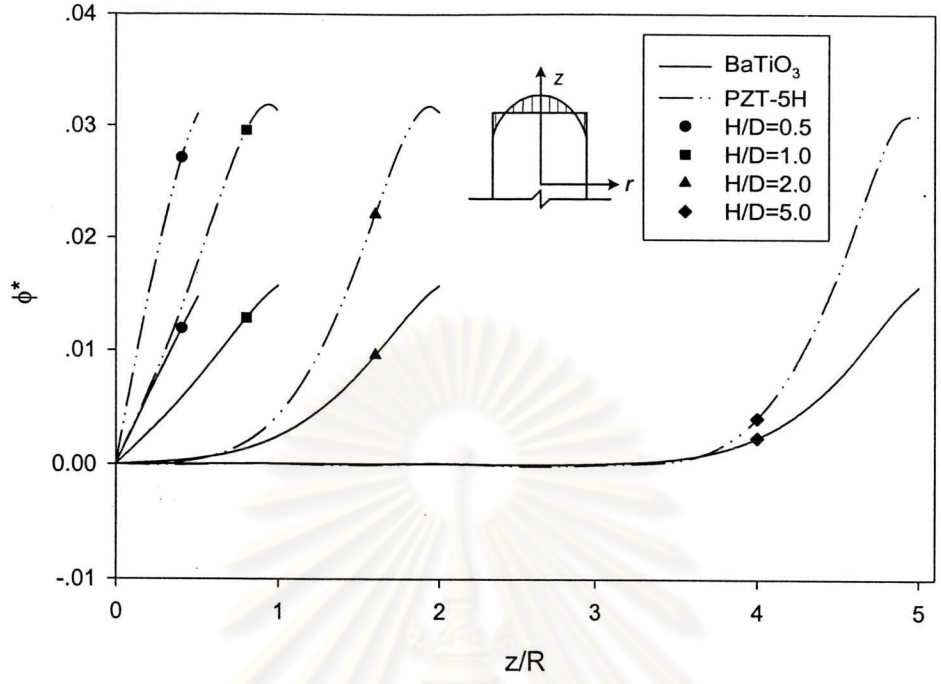

(a)

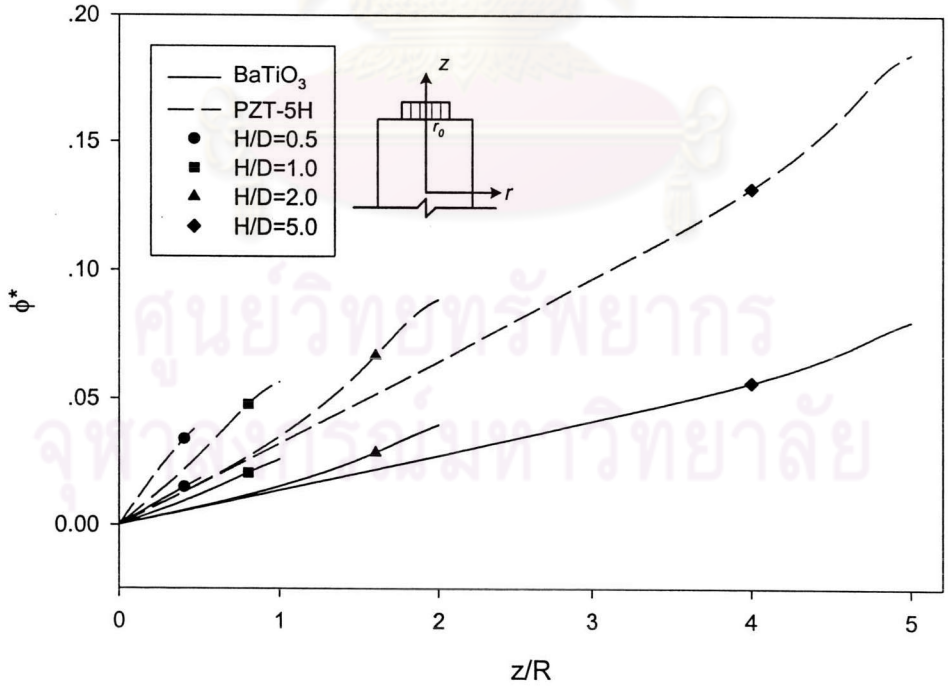

Figure 4.34 Non-dimensional electric potential profiles along z -axis at r =0 due to (a) parabolic load and (b) uniform load for various shape factors.

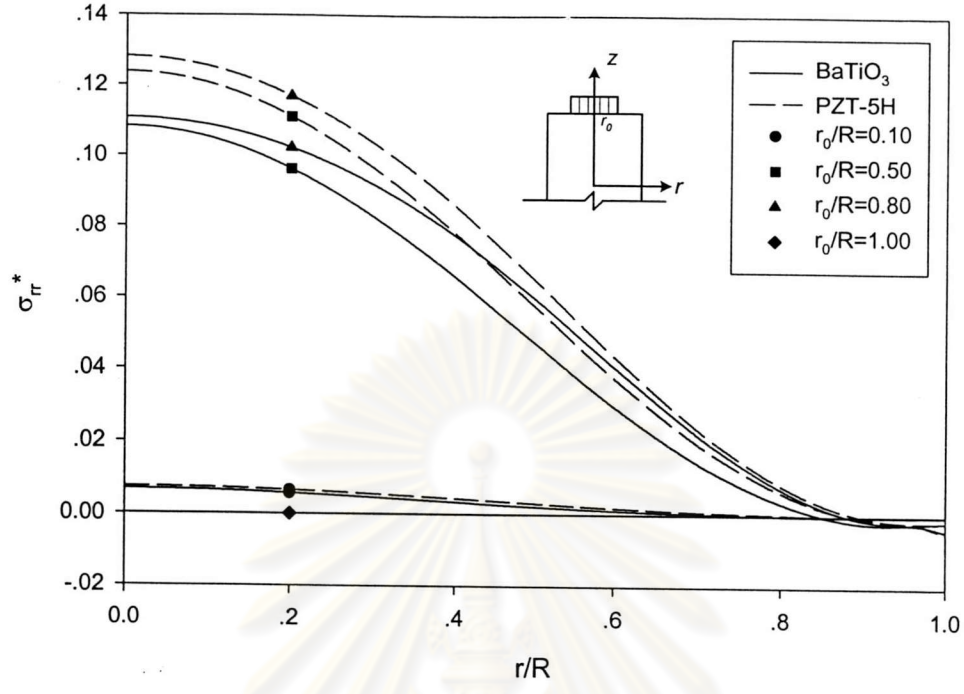

(a) Along r-axis at z=0.

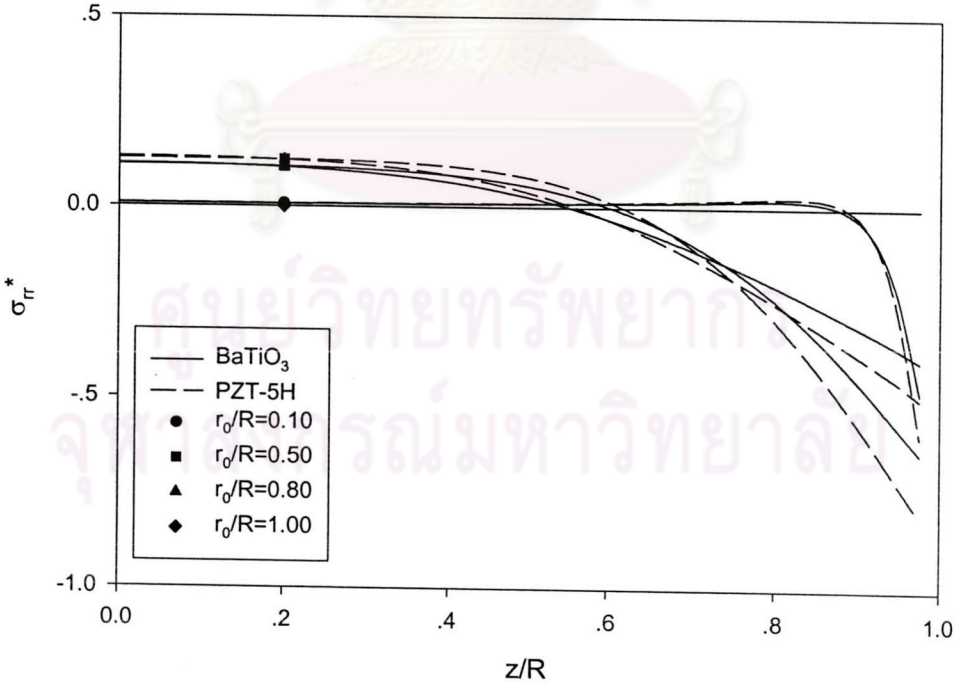

(b) Along z-axis at r=0.

Figure 4.35 Non-dimensional radial stress profiles due to uniform load for various r_0.

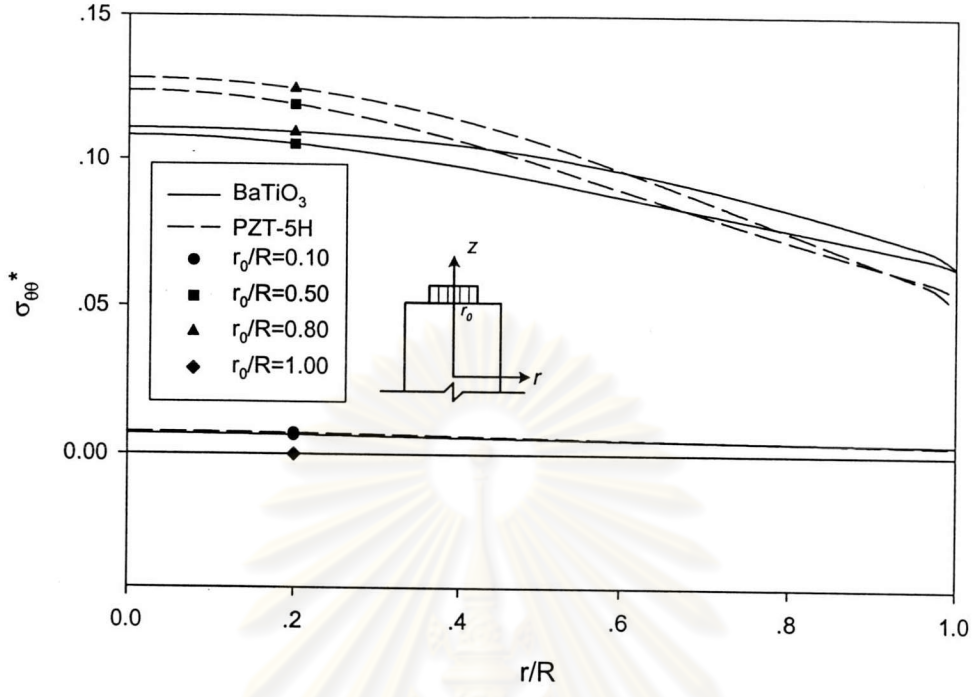

(a) Along r-axis at z=0.

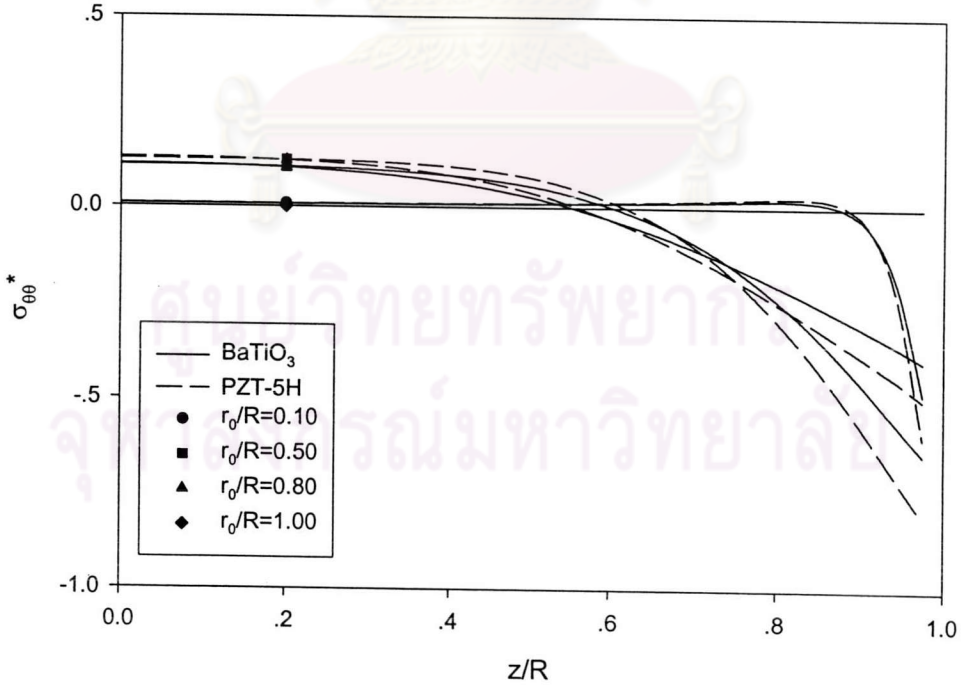

(b) Along z-axis at r=0.

Figure 4.36 Non-dimensional hoop stress profiles due to uniform load for various r_0.

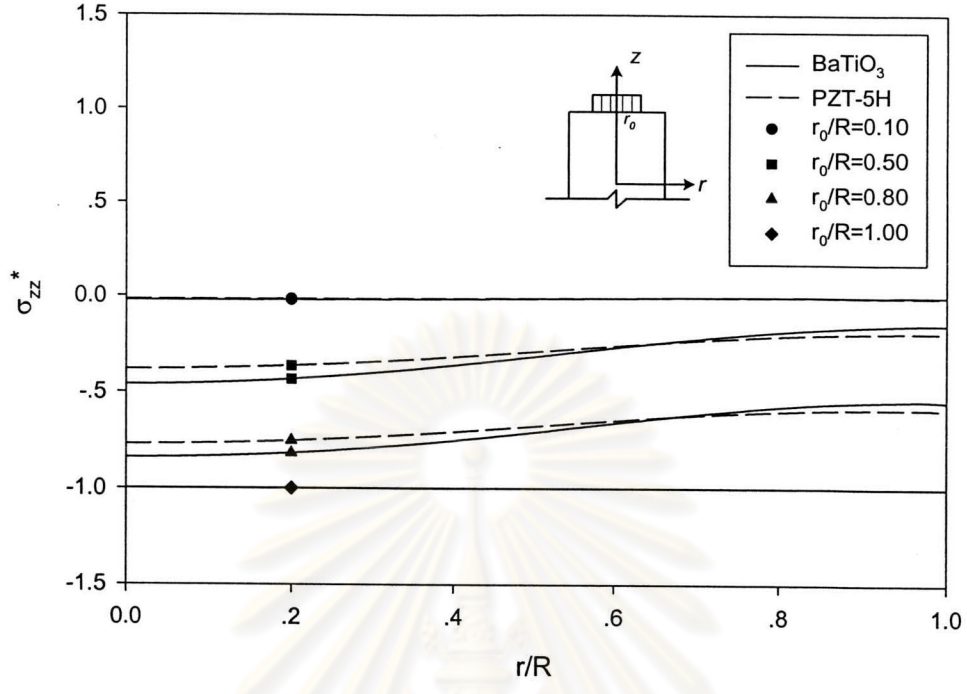

(a) Along r-axis at z=0.

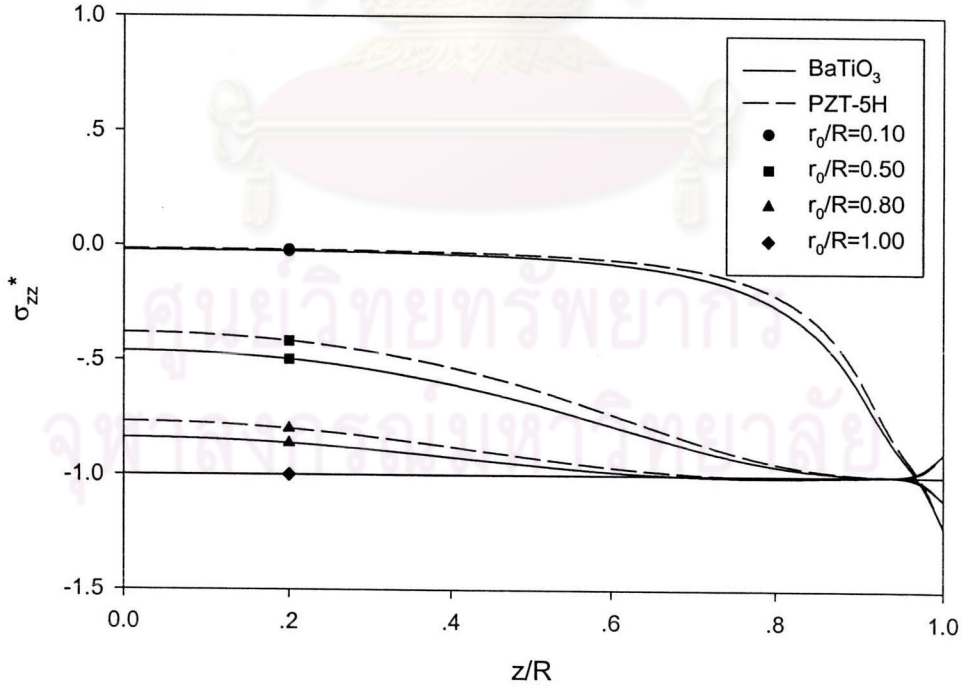

(b) Along z-axis at r=0.

Figure 4.37 Non-dimensional vertical stress profiles due to uniform load for various r_0.

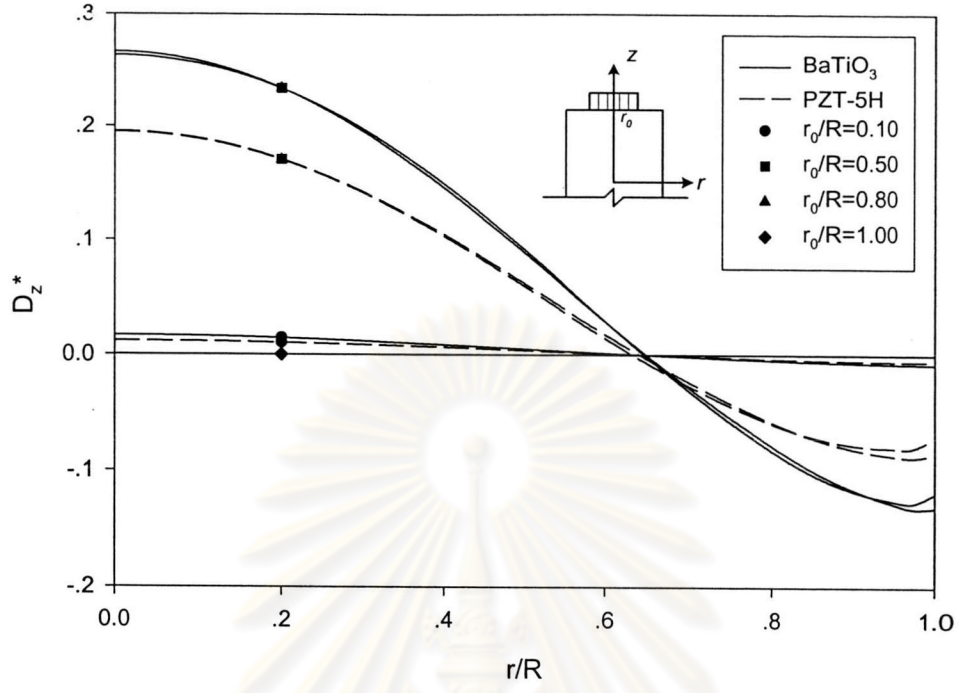

(a) Along r-axis at z=0.

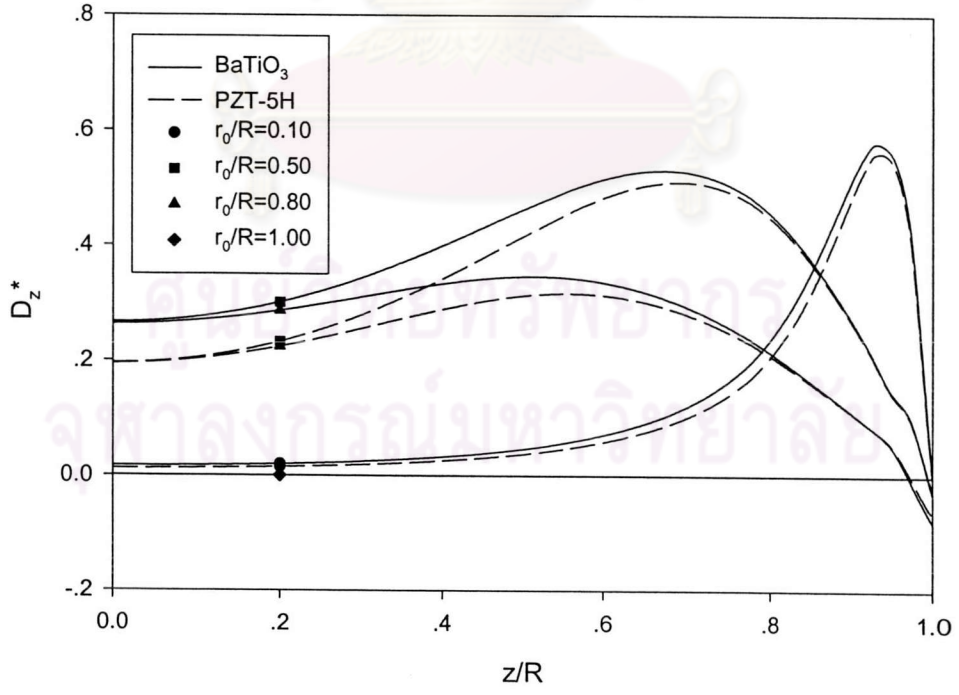

(b) Along z-axis at r=0.

Figure 4.38 Non-dimensional electric displacement profiles due to uniform load for various r_0.

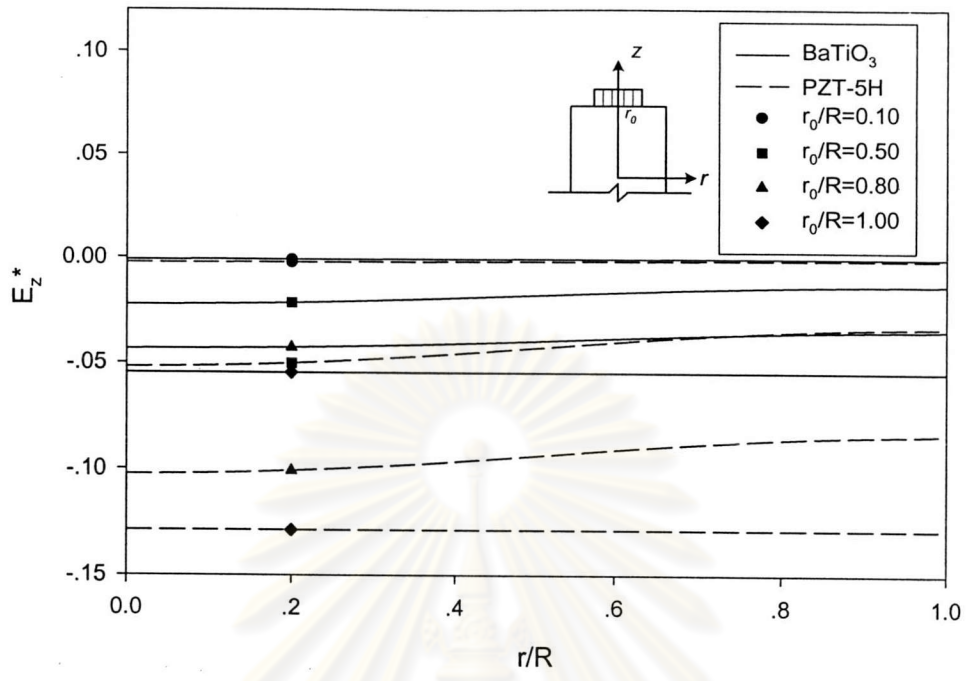

(a) Along r-axis at z=0.

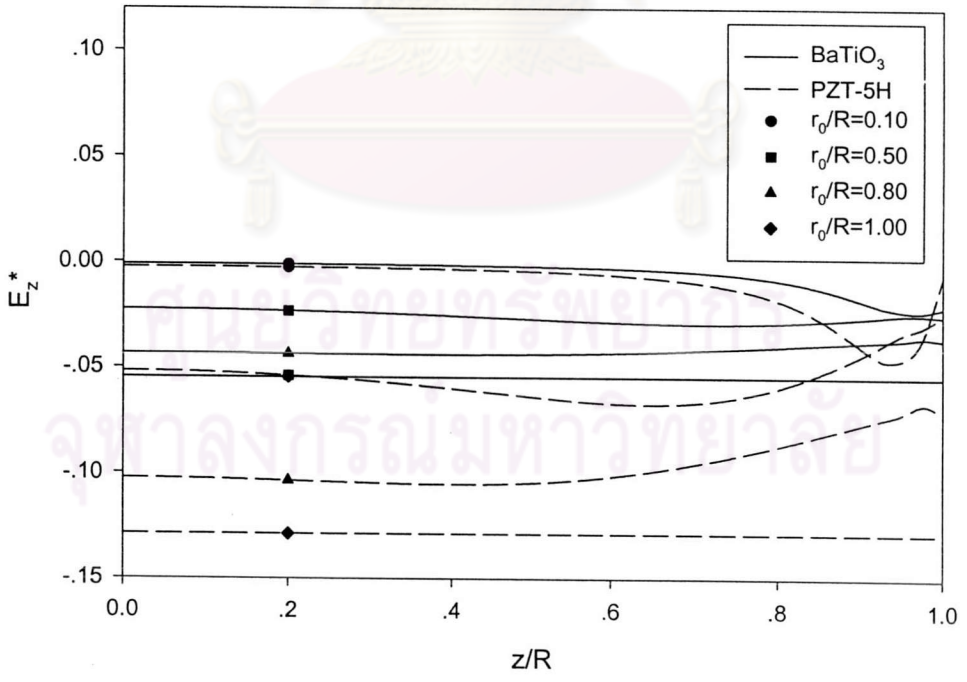

(b) Along z-axis at r=0.

Figure 4.39 Non-dimensional electric field profiles due to uniform load for various r_0.

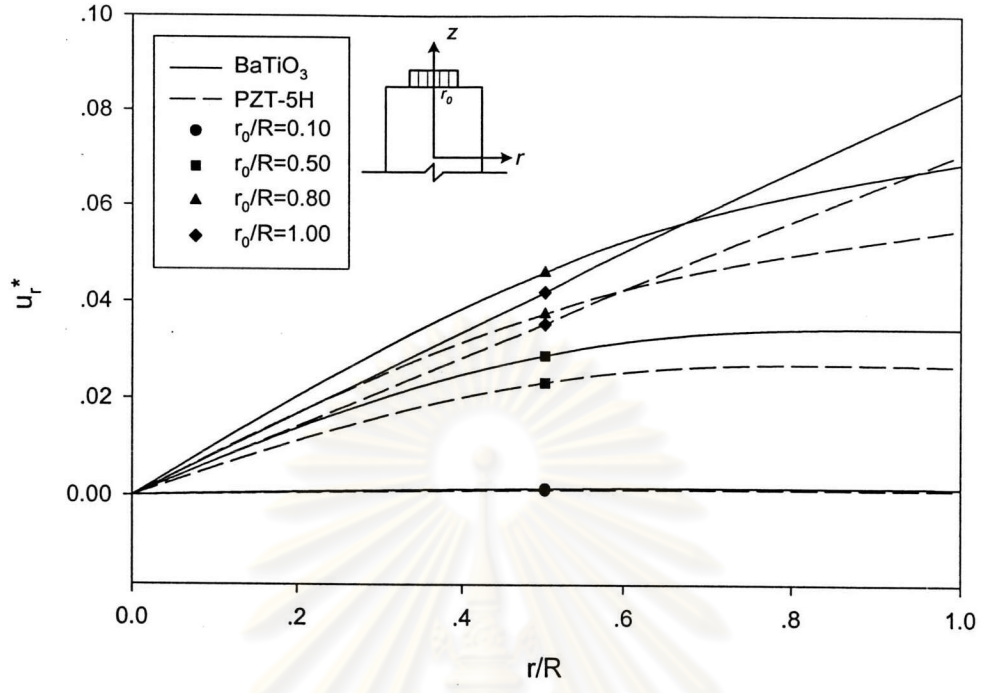

Figure 4.40 Non-dimensional radial displacement profiles along r-axis at z=0 due to uniform load for various r_0.

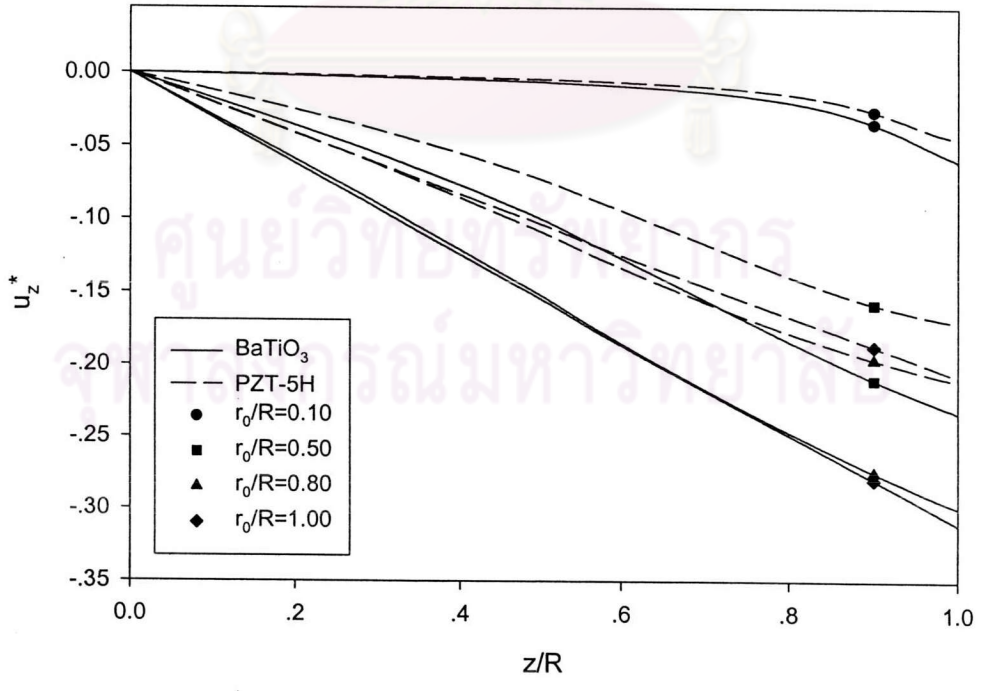

Figure 4.41 Non-dimensional radial and vertical displacement profiles along z-axis at r=0 due to uniform load for various r_0.

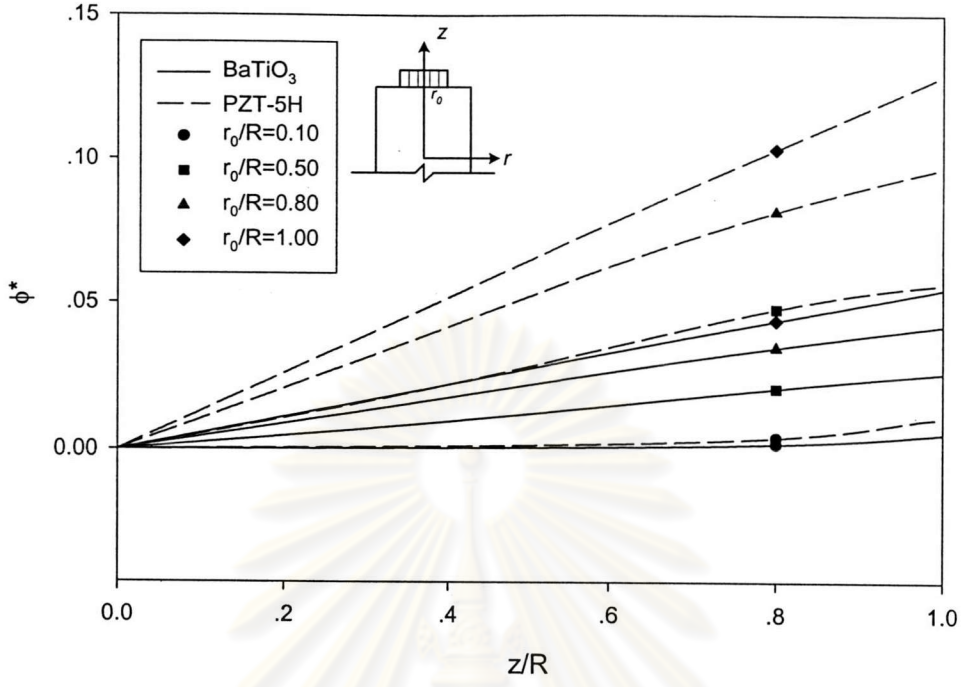

Figure 4.42 Non-dimensional electric potential profiles along z -axis at r =0 due to uniform load for various r_0 .

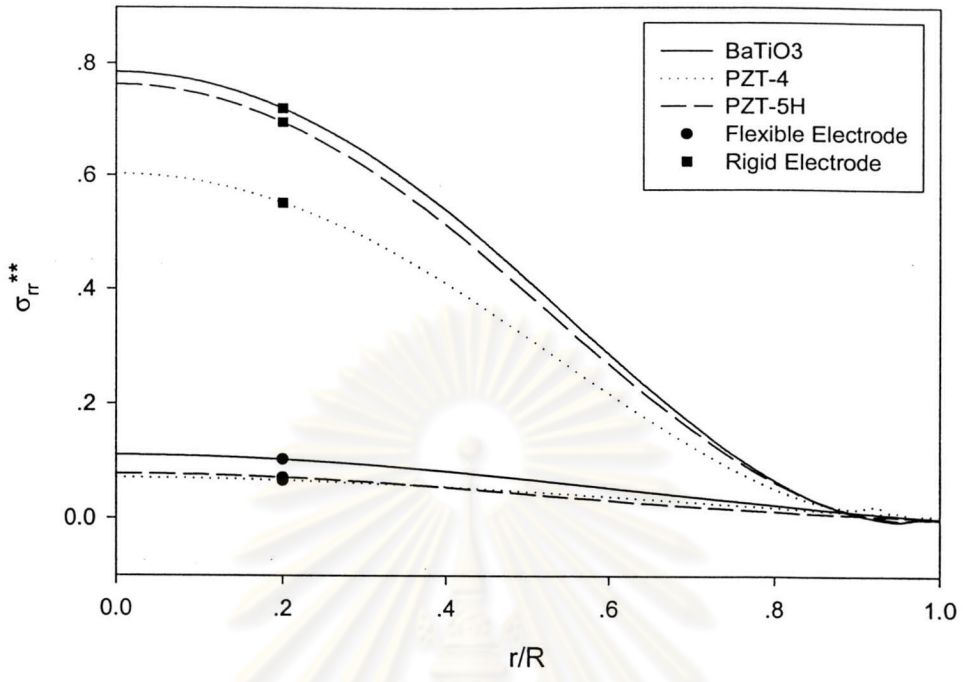

(a) Along r-axis at z=0.

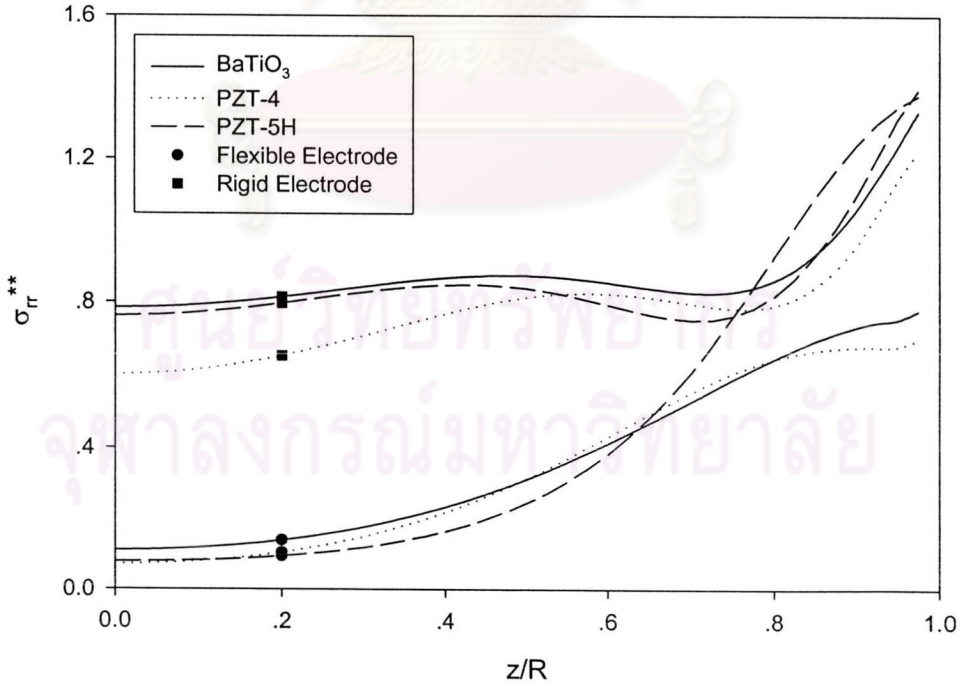

(b) Along z-axis at r=0.

Figure 4.43 Non-dimensional radial stress profiles due to electrical loading for flexible and rigid electrodes.

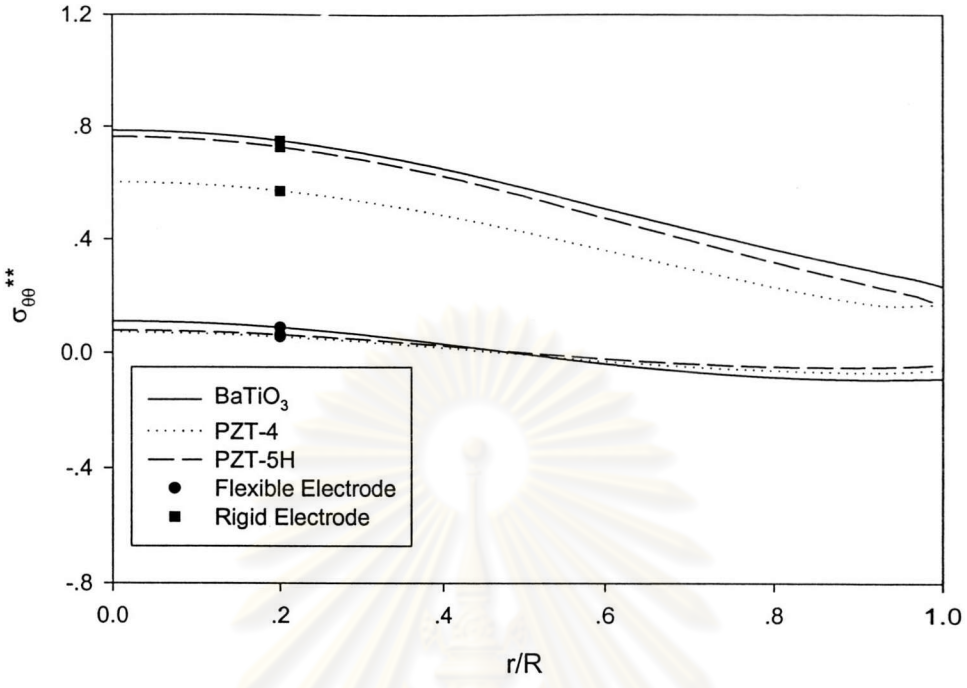

(a) Along r-axis at z =0.

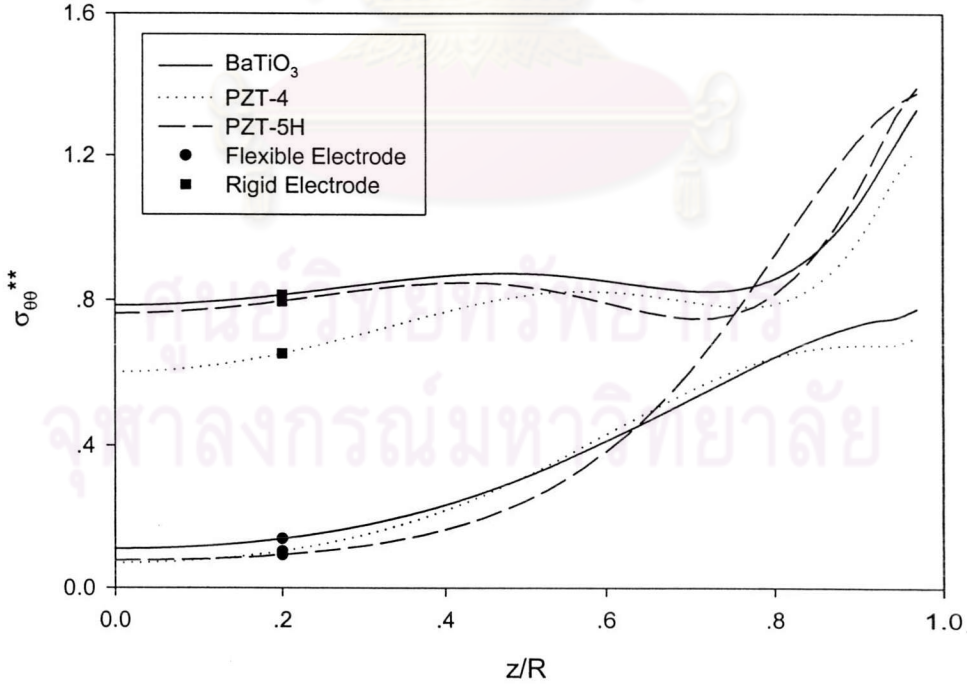

(b) Along z-axis at r =0.

Figure 4.44 Non-dimensional hoop stress profiles due to electrical loading for flexible and rigid electrodes.

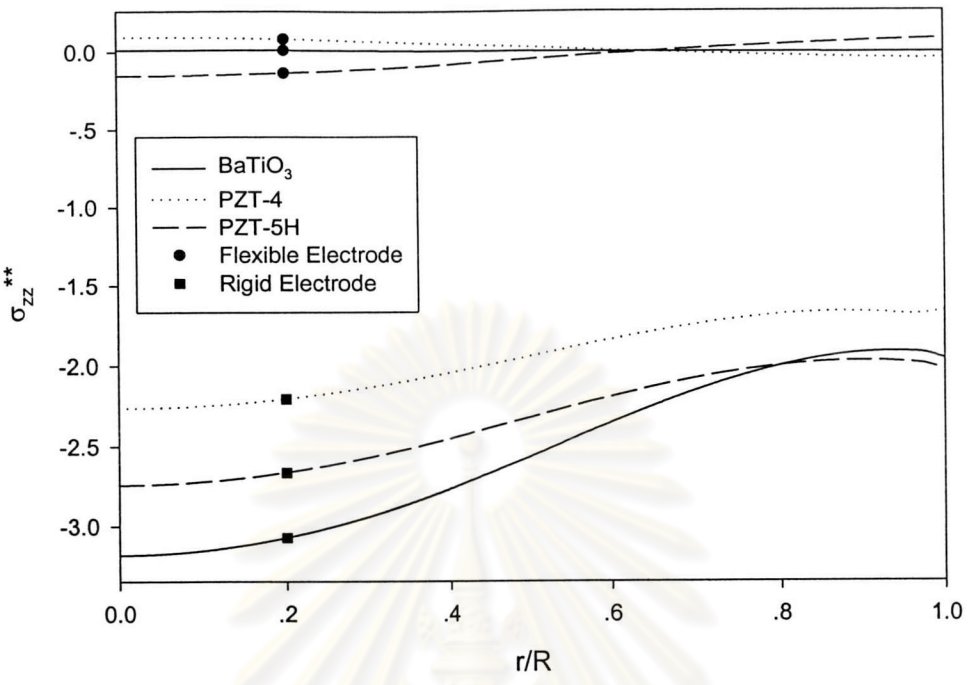

(a) Along r-axis at z=0.

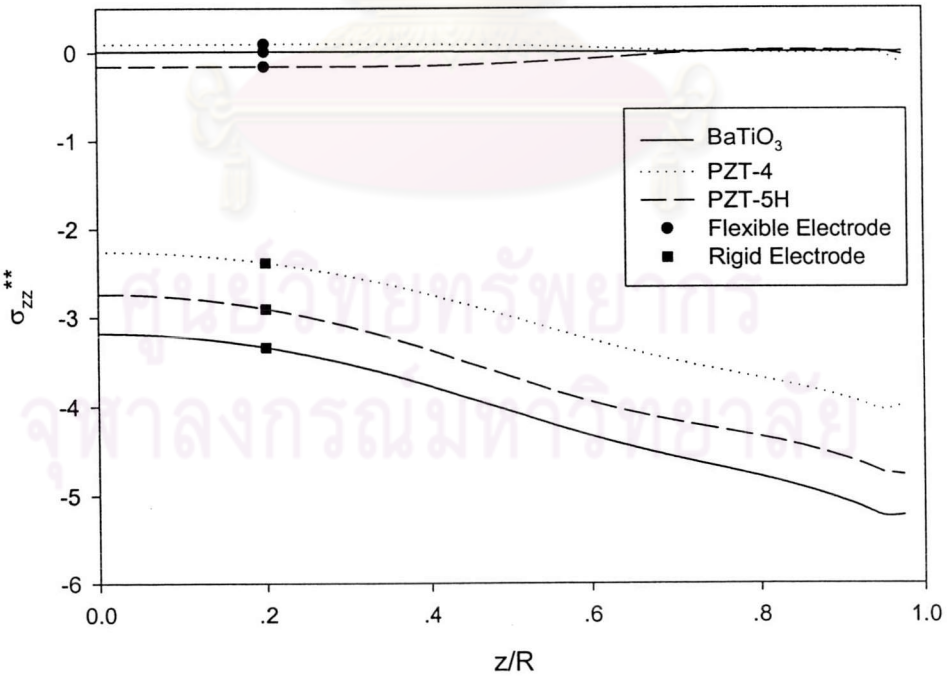

(b) Along z-axis at r=0.

Figure 4.45 Non-dimensional vertical stress profiles due to electrical loading for flexible and rigid electrodes.

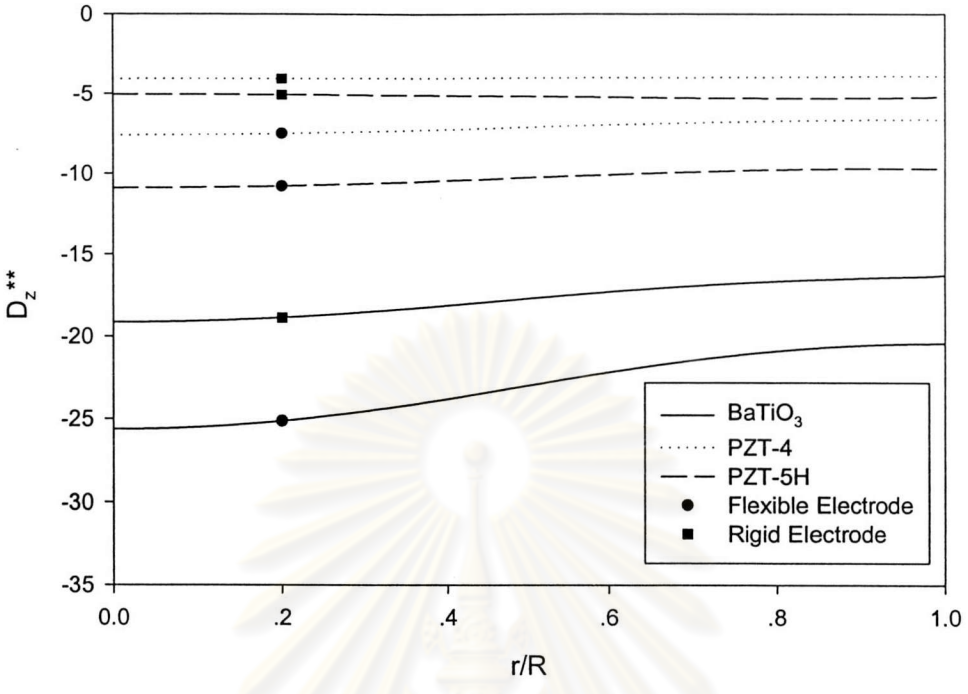

(a) Along r-axis at z=0.

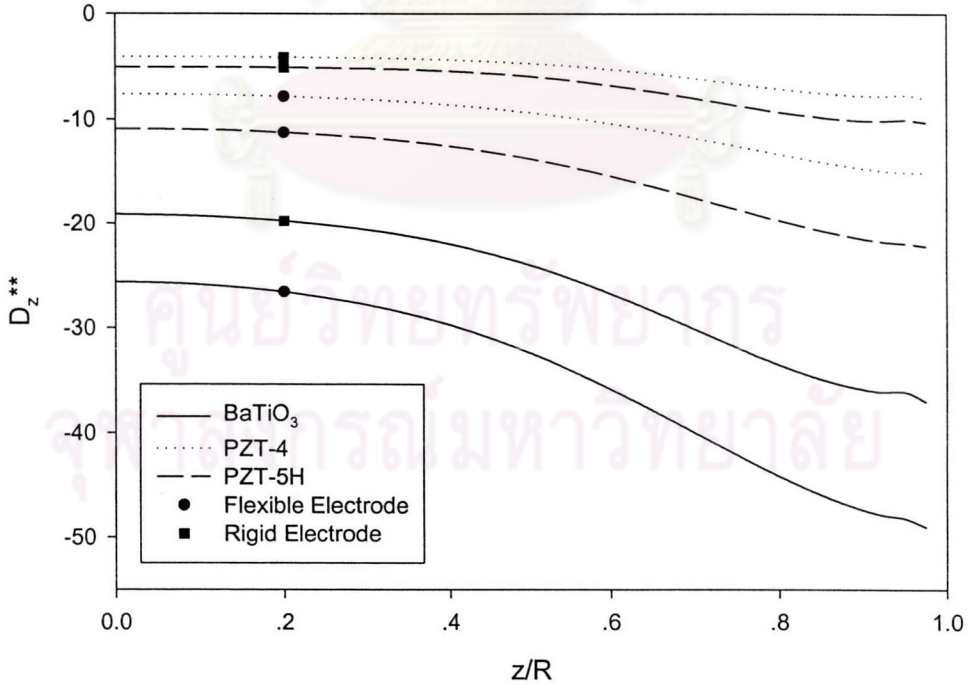

(b) Along z-axis at r=0.

Figure 4.46 Non-dimensional electric displacement profiles due to electrical loading for flexible and rigid electrodes.

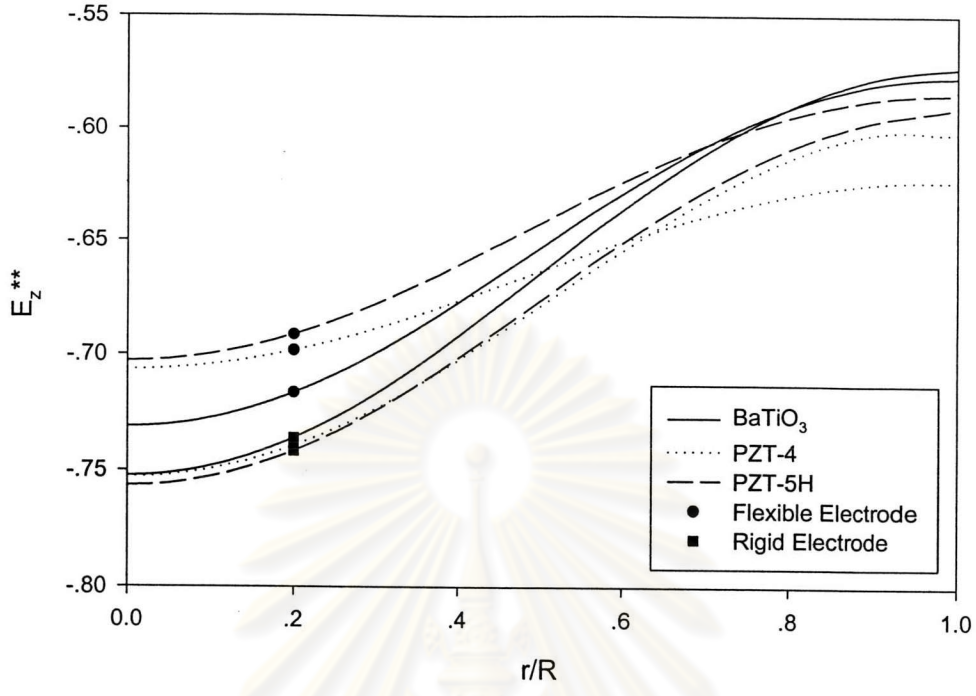

(a) Along r -axis at z =0.

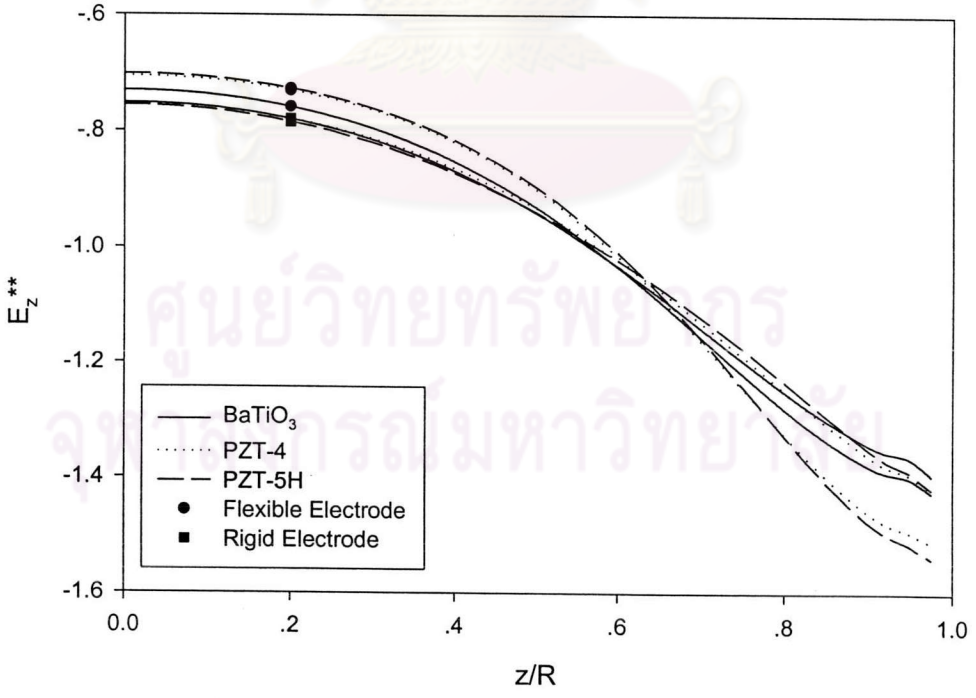

(b) Along z -axis at r =0.

Figure 4.47 Non-dimensional electric field profiles due to electrical loading for flexible and rigid electrodes.

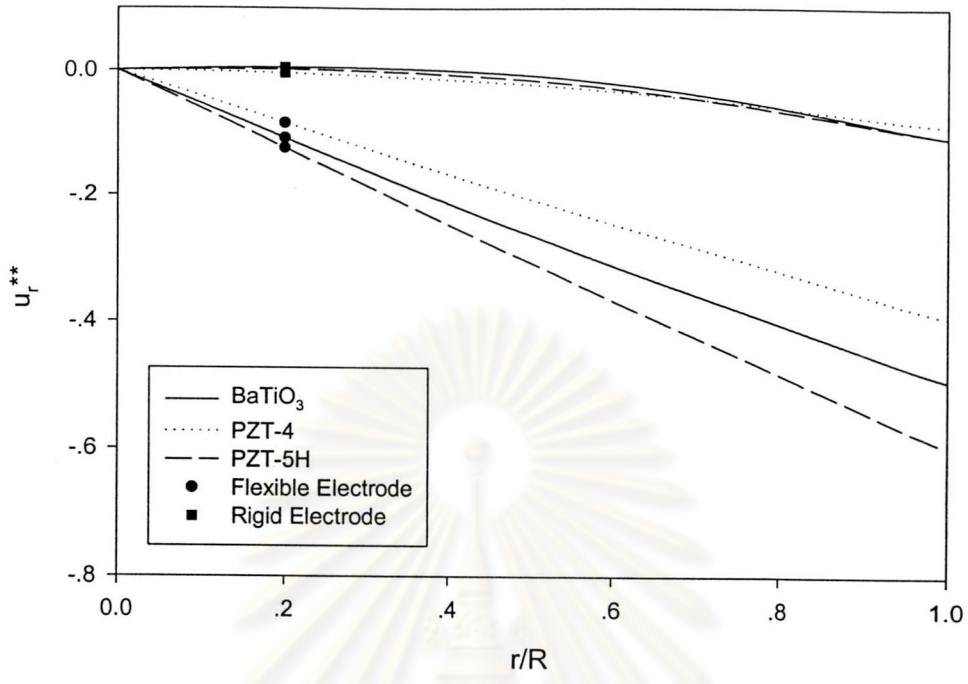

Figure 4.48 Non-dimensional radial displacement profiles along r-axis at z =0 due to electrical loading for flexible and rigid electrodes.

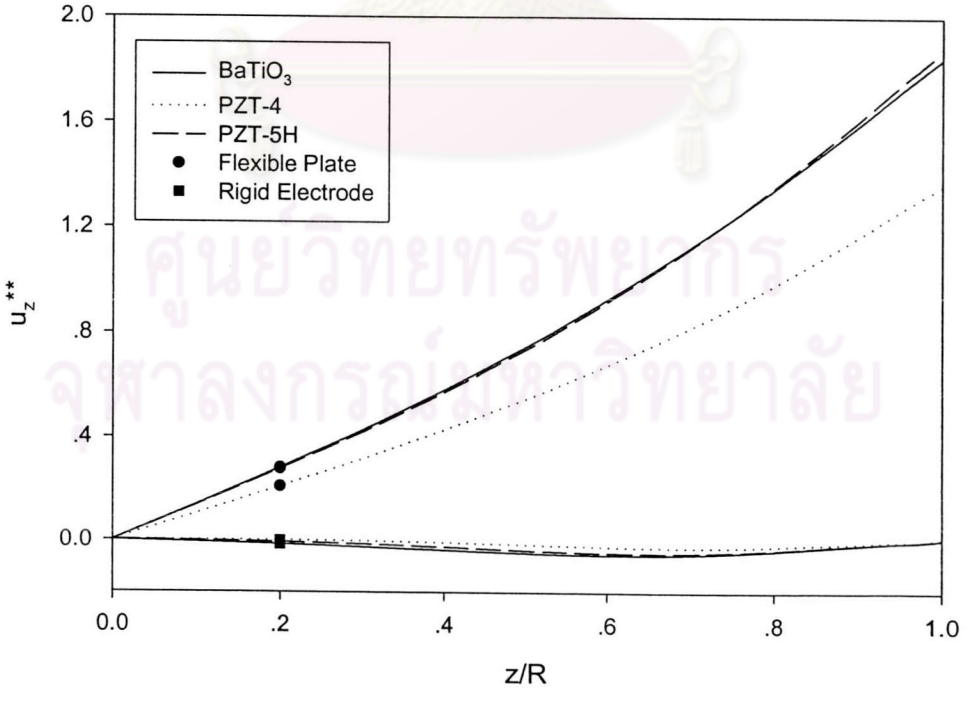

Figure 4.49 Non-dimensional vertical displacement profiles along z-axis at r =0 due to electrical loading for flexible and rigid electrodes.

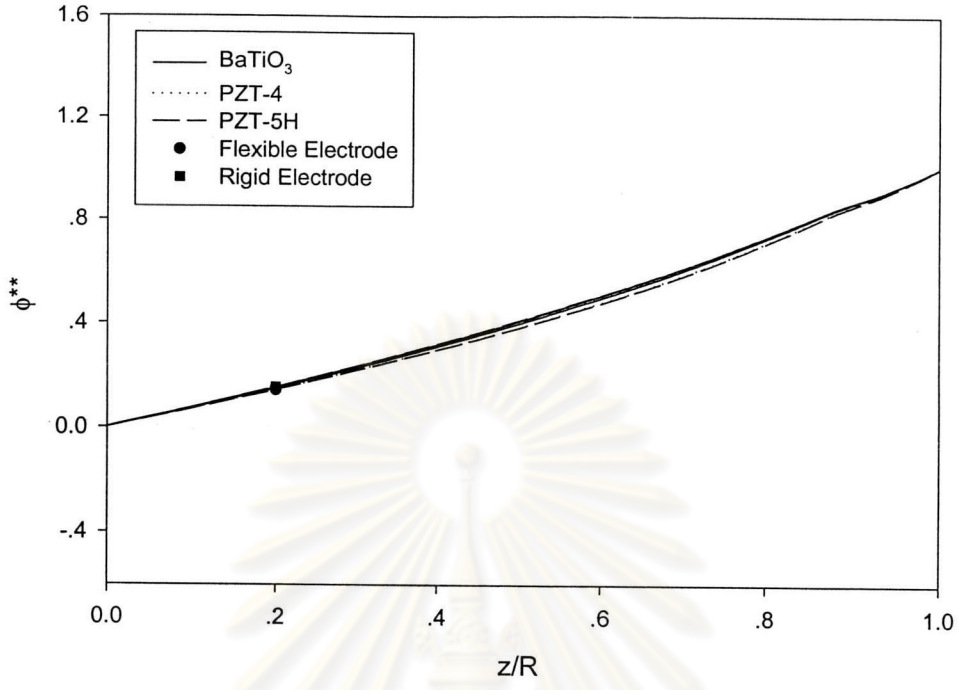

Figure 4.50 Non-dimensional electric potential profiles along z-axis **at** $r=0$ due to electrical loading for flexible and rigid electrodes.

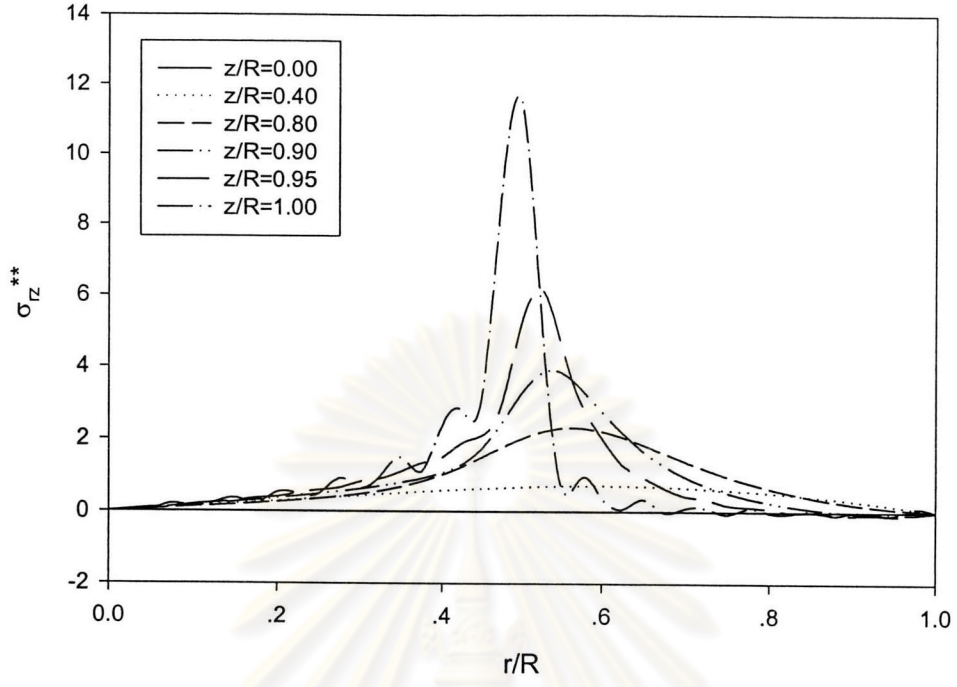

Figure 4.51 Non-dimension shear stress profiles along the r-axis for different z due to electrical loading with rigid electrode.

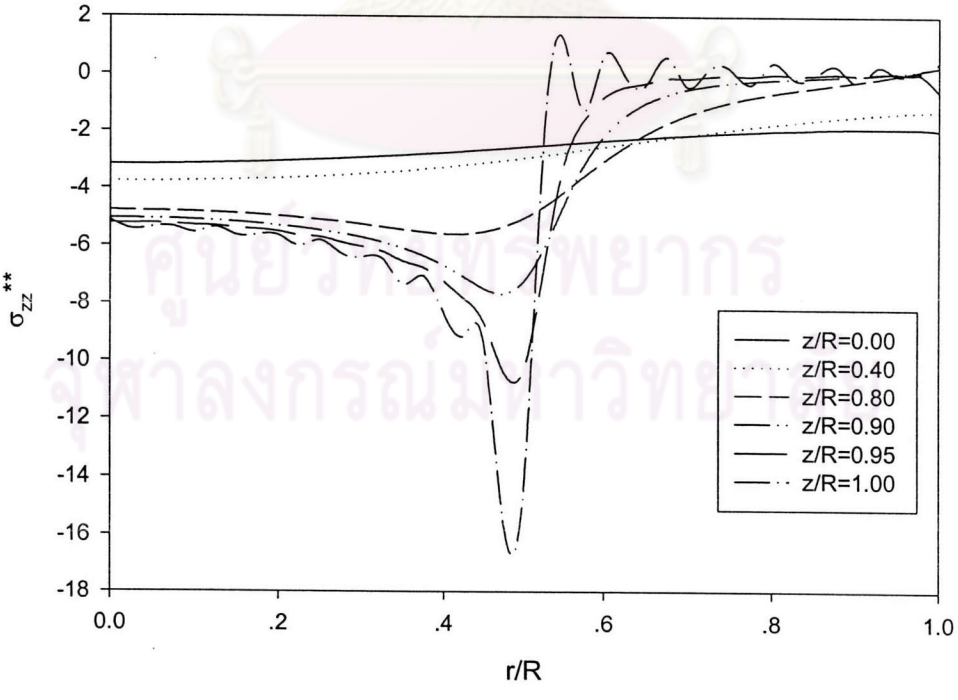

Figure 4.52 Non-dimension vertical stress profiles along the r-axis for different z due to electrical loading with rigid electrode.

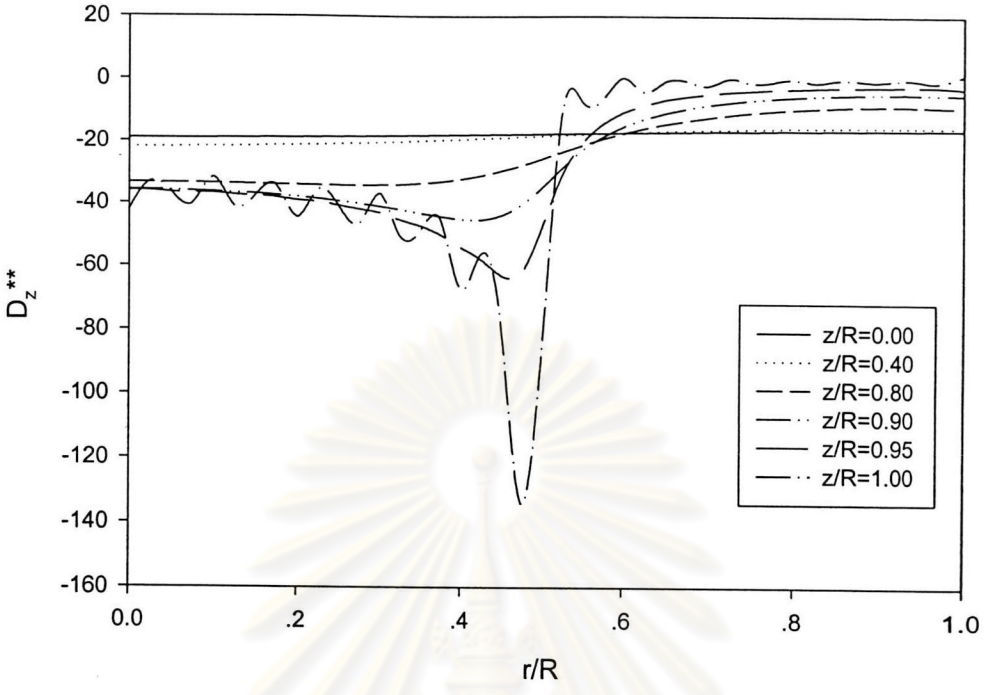

Figure 4.53 Non-dimension vertical electric displacement profiles along the r-axis for different z due to electrical loading with rigid electrode.

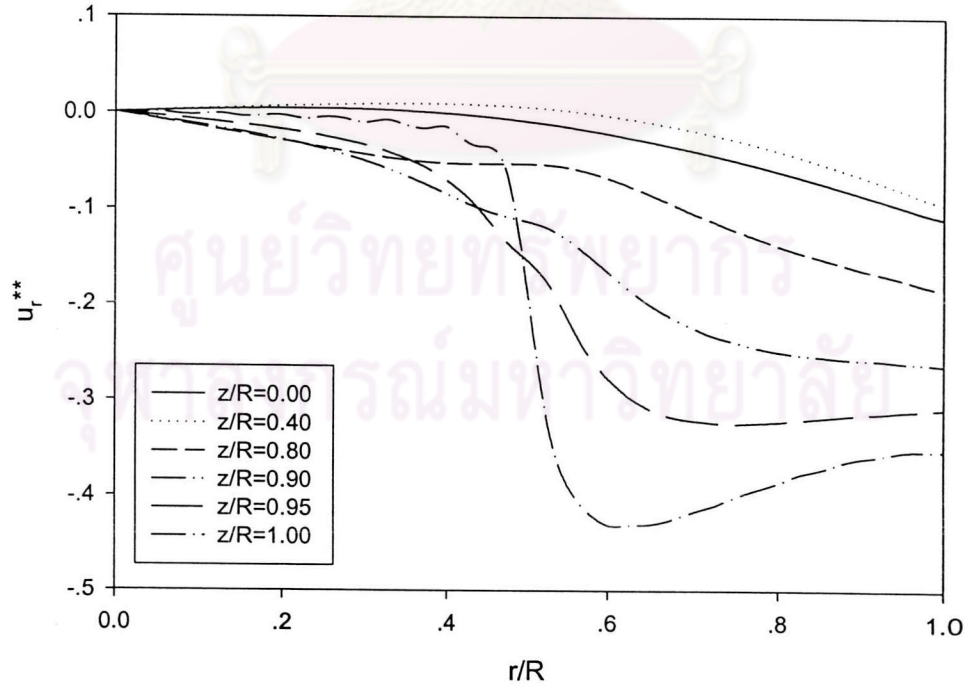

Figure 4.54 Non-dimension radial displacement profiles along the r-axis for different z due to electrical loading with rigid electrode.

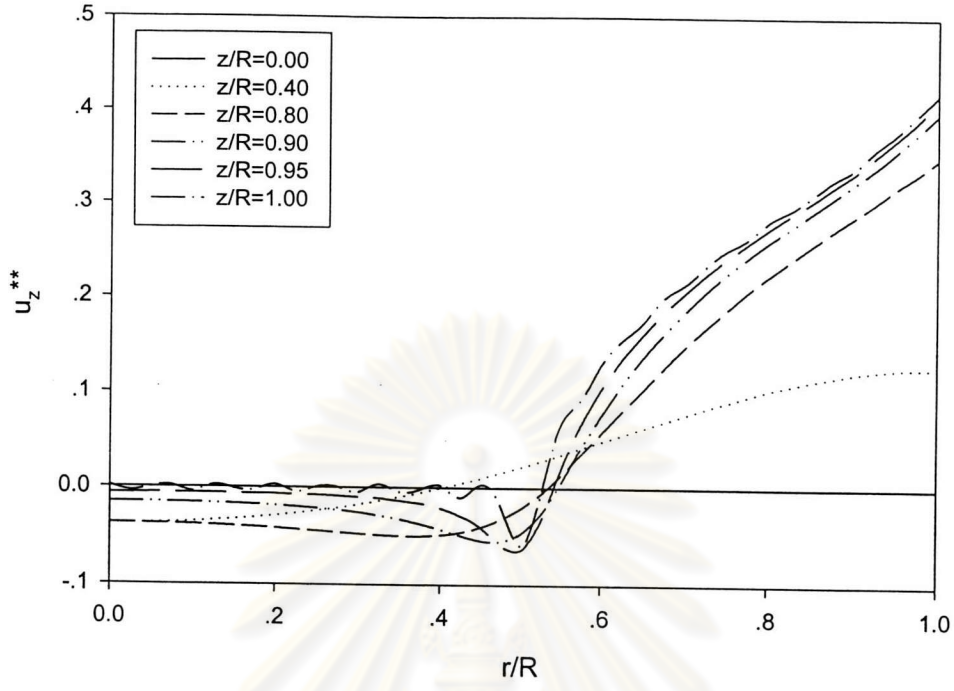

Figure 4.55 Non-dimension vertical displacement profiles along the r-axis for different z due to electrical loading with rigid electrode.

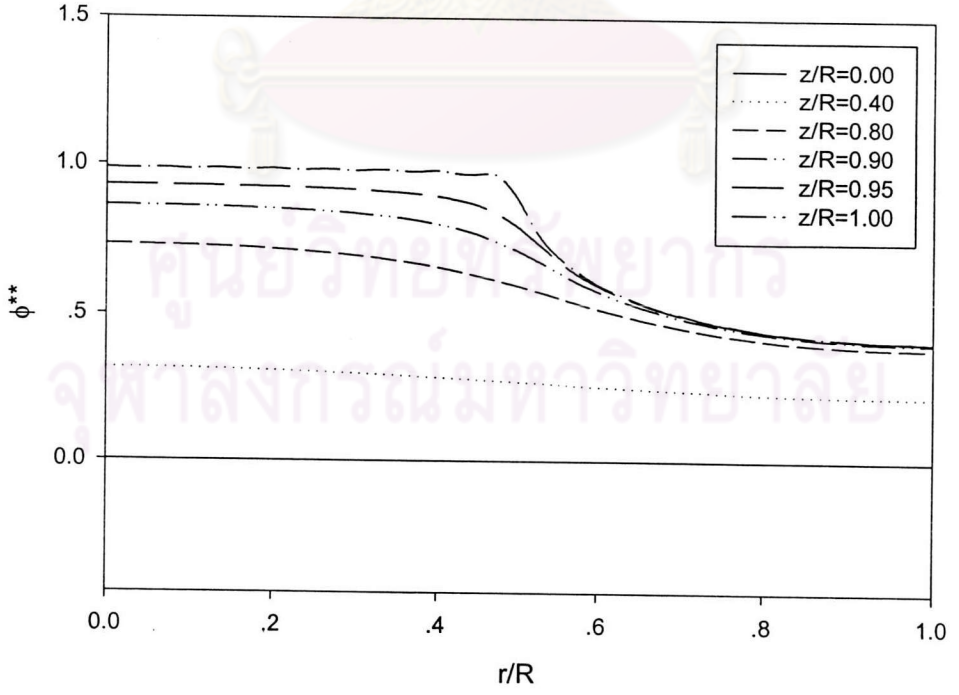

Figure 4.56 Non-dimension electric potential profiles along the r-axis for different z due to electrical loading with rigid electrode.

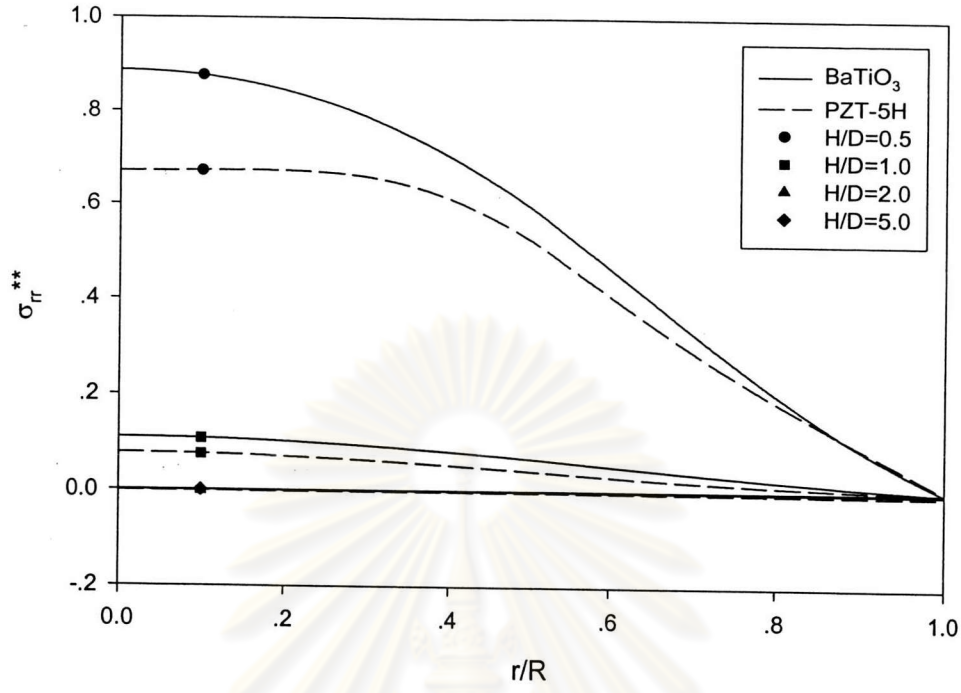

(a) Along r-axis at $z=0$

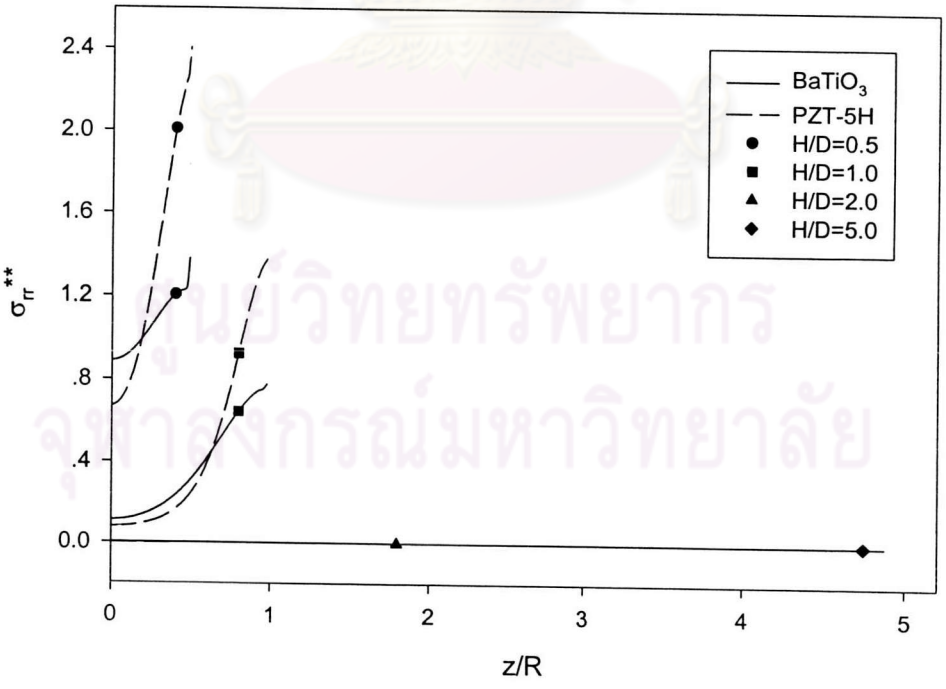

(b) Along z-axis at $r=0$

Figure 4.57 Non-dimensional radial stress profiles due to electrical loading for various shape factors H/D with flexible electrode.

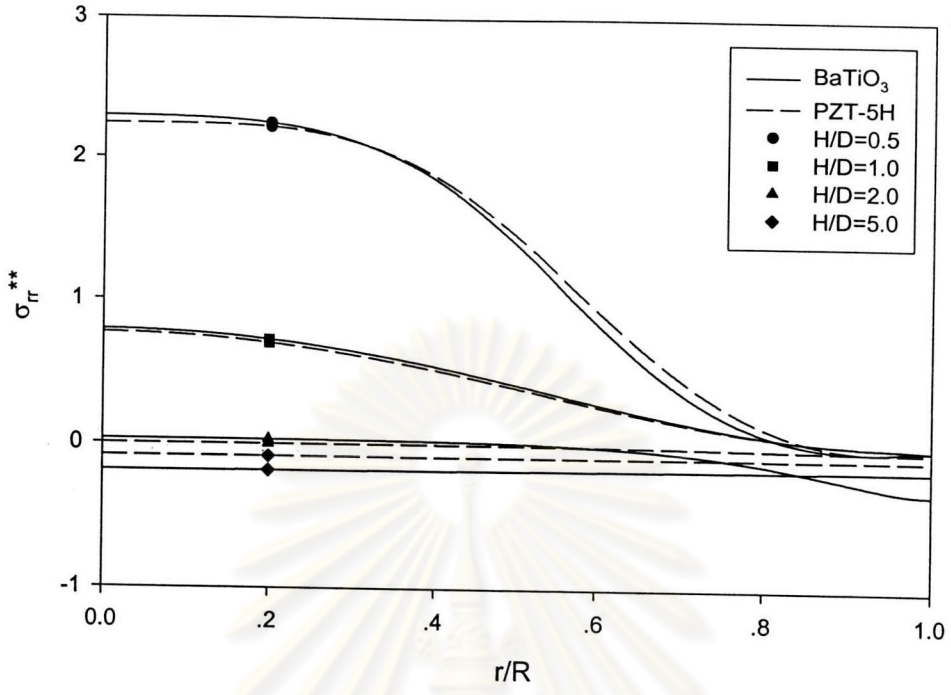

(a) Along r-axis at $z=0$

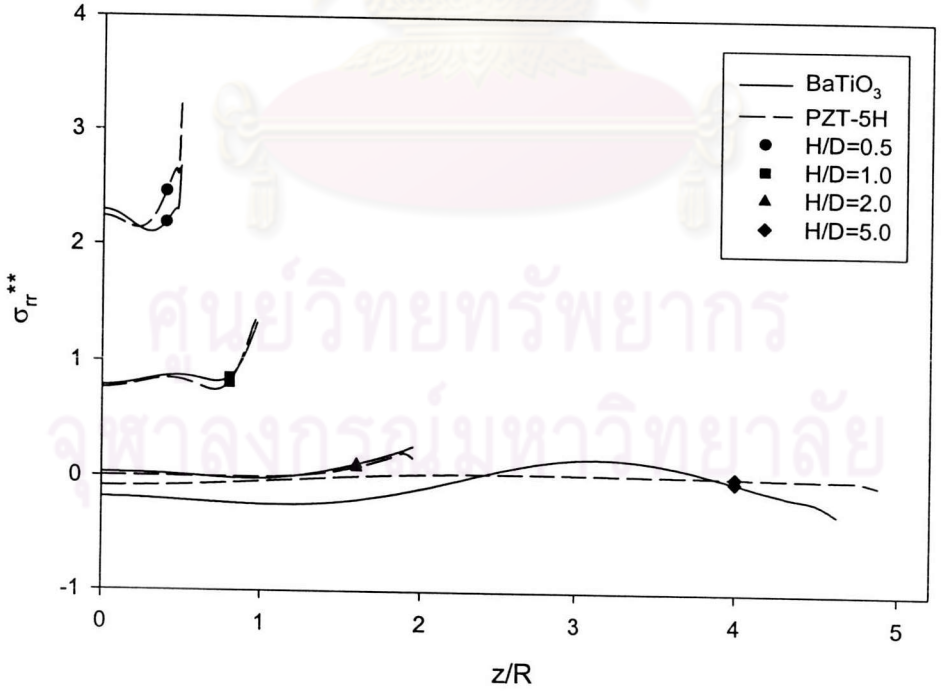

(b) Along z-axis at $r=0$

Figure 4.58 Non-dimensional radial stress profiles due to electrical loading for various shape factors H/D with rigid electrode.

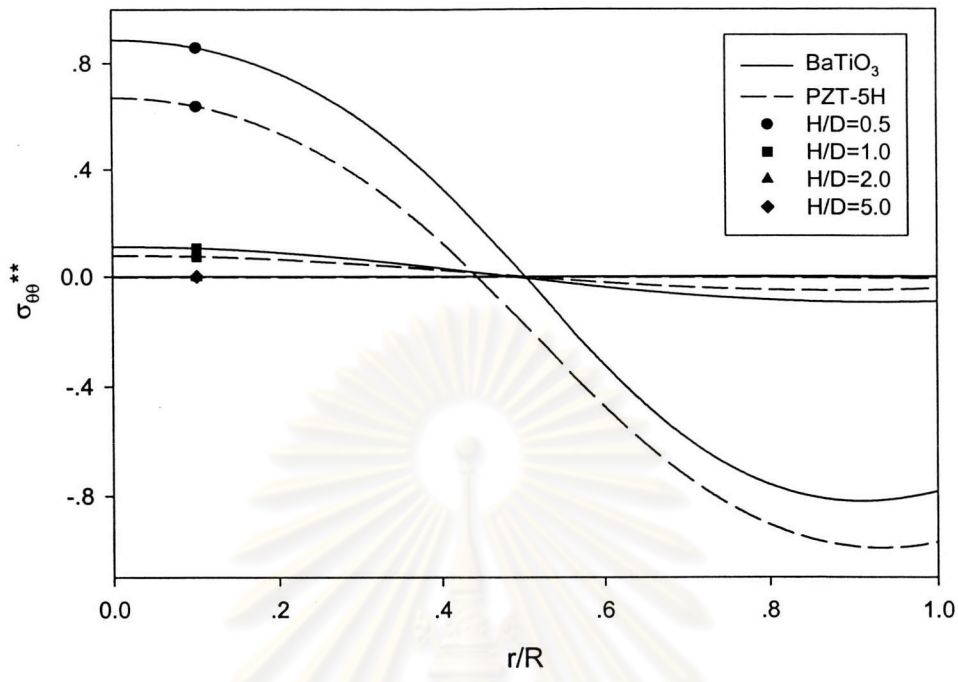

(a) Along r-axis at $z=0$

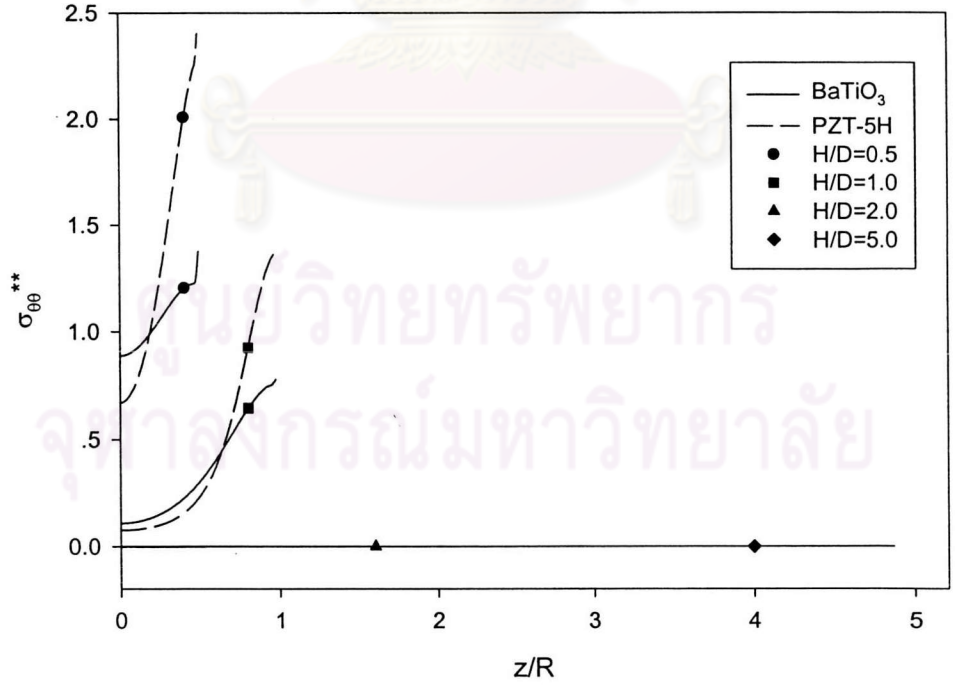

(b) Along z-axis at $r=0$

Figure 4.59 Non-dimensional hoop stress profiles due to electrical loading for various shape factors H/D with flexible electrode.

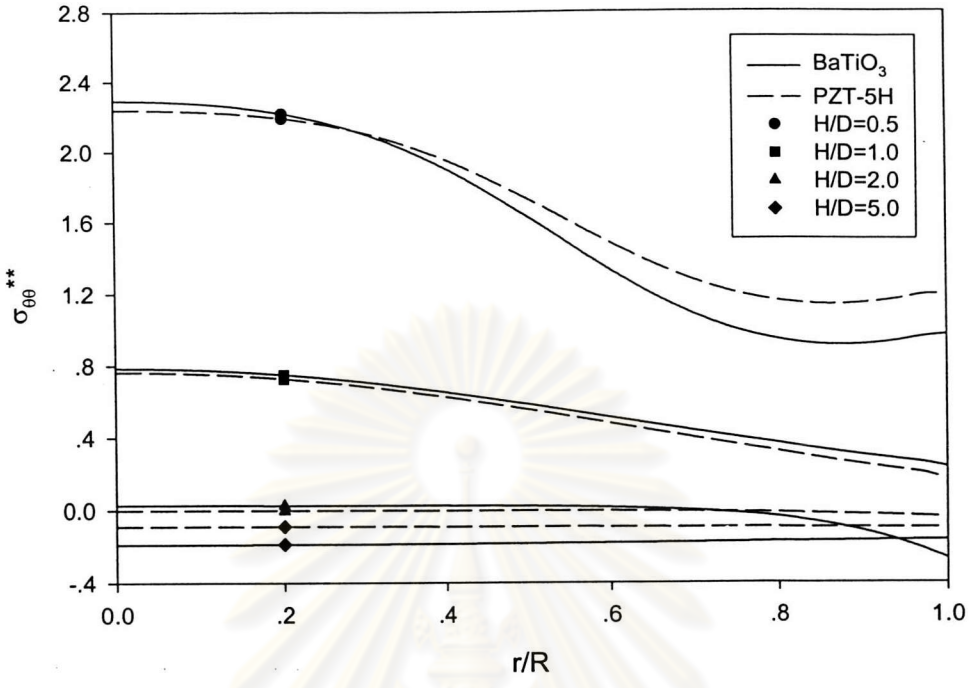

(a) Along r-axis at z=0

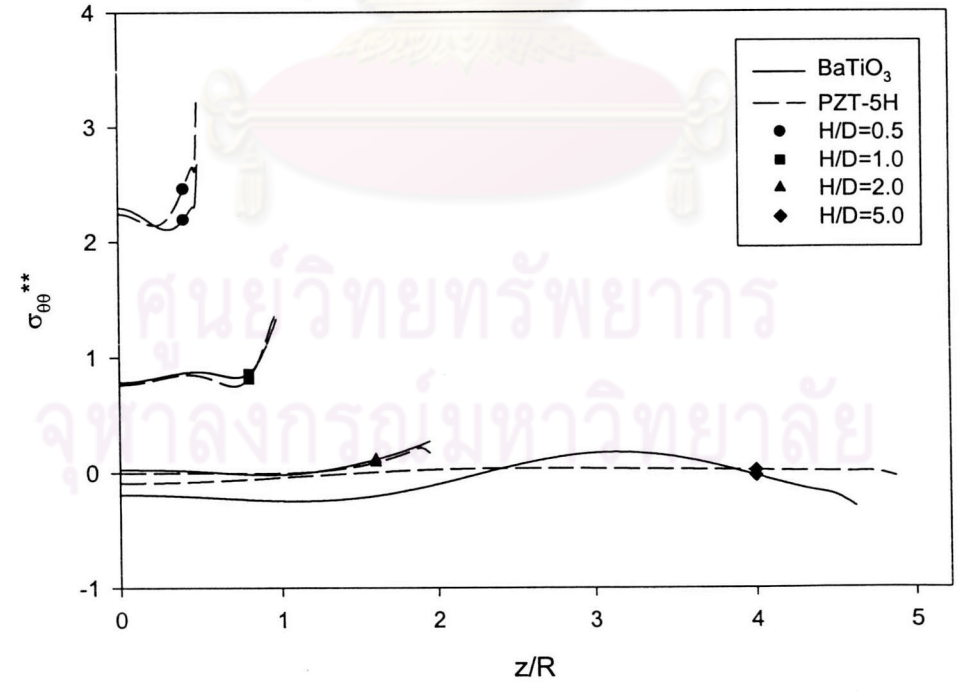

(b) Along z-axis at r=0

Figure 4.60 Non-dimensional hoop stress profiles due to electrical loading for various shape factors H/D with rigid electrode.

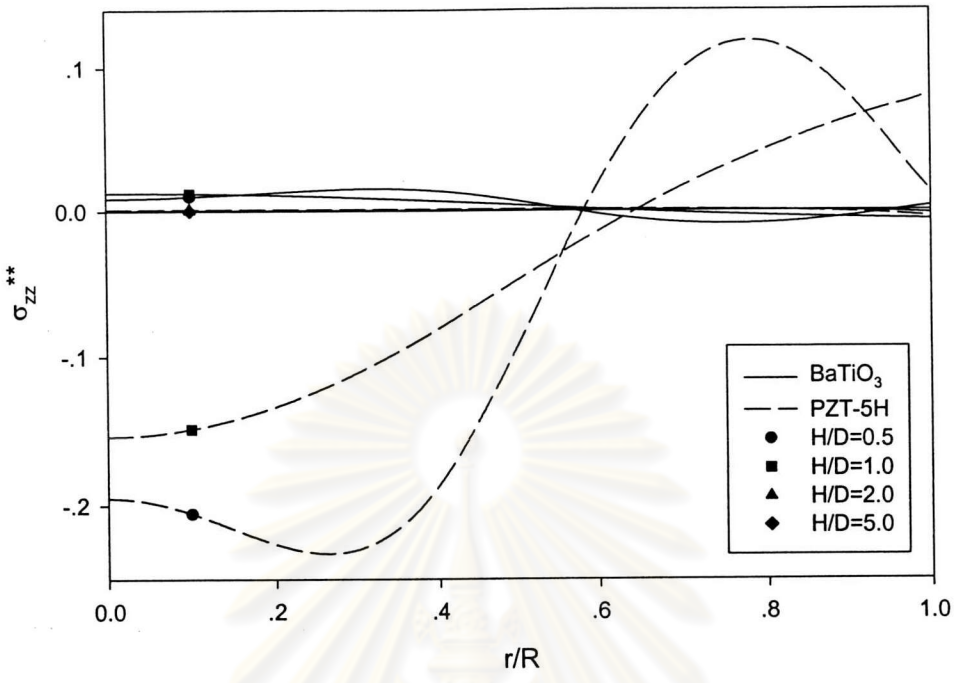

(a) Along r-axis at $z=0$

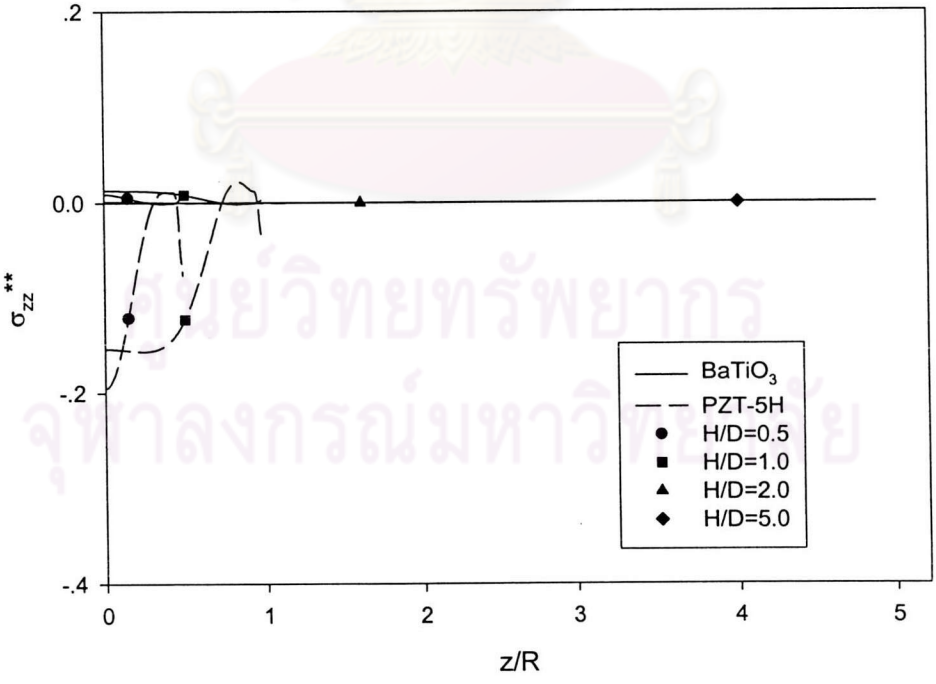

(b) Along z-axis at $r=0$

Figure 4.61 Non-dimensional vertical stress profiles due to electrical loading for various shape factors H/D with flexible electrode.

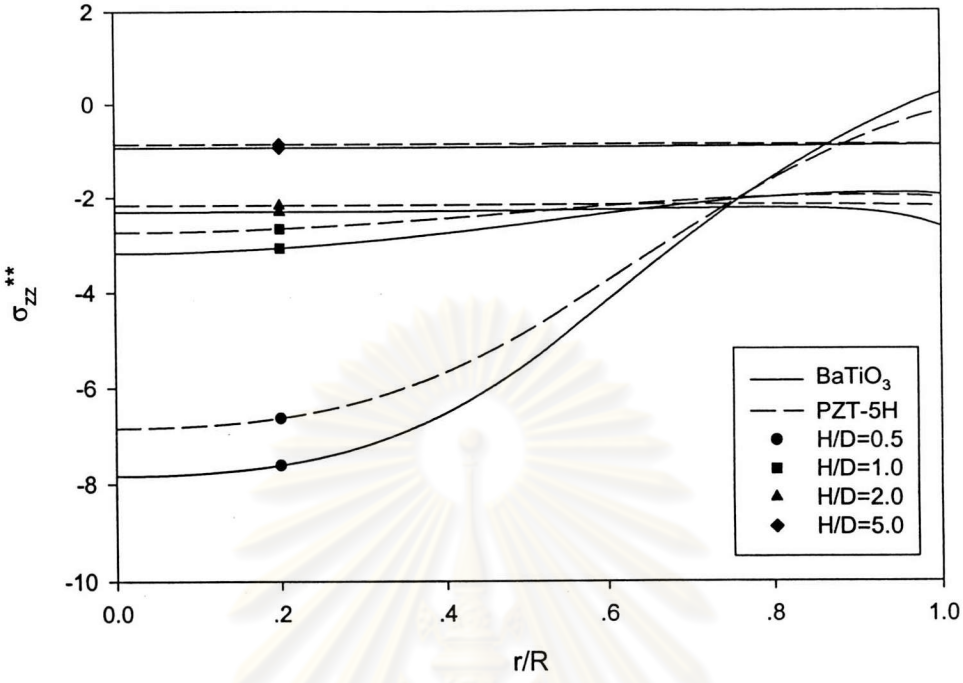

(a) Along r-axis at $z=0$

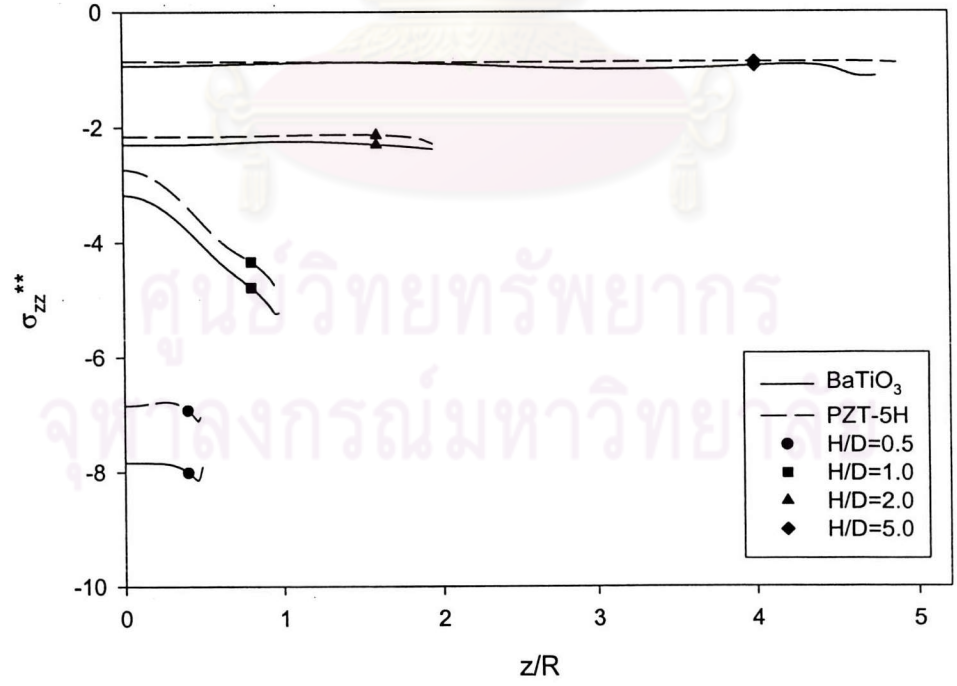

(b) Along z-axis at $r=0$

Figure 4.62 Non-dimensional vertical stress profiles due to electrical loading for various shape factors H/D with rigid electrode.

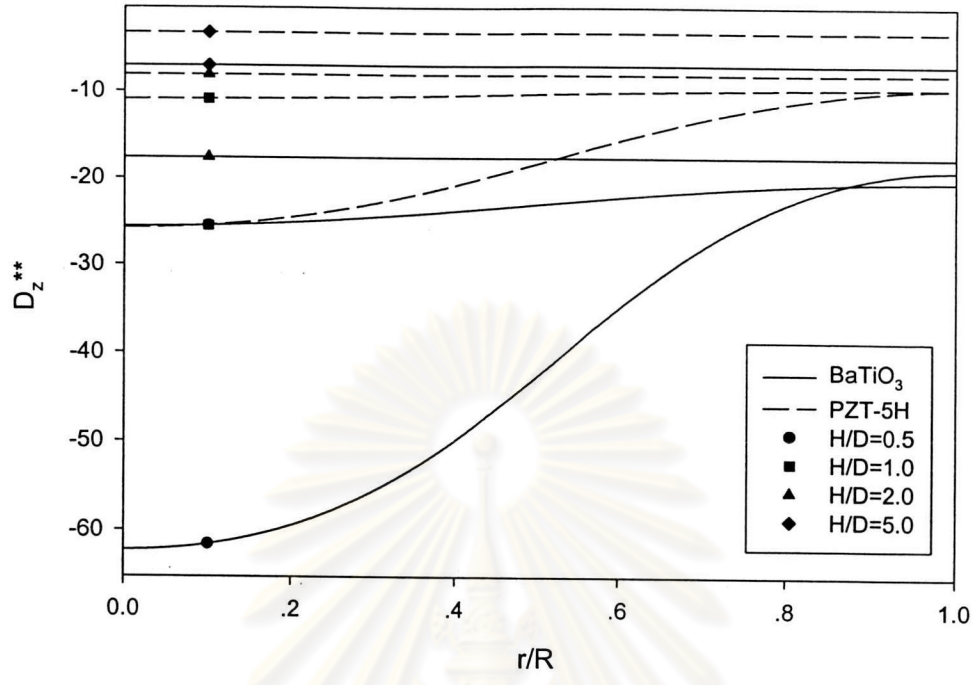

(a) Along r-axis at $z=0$

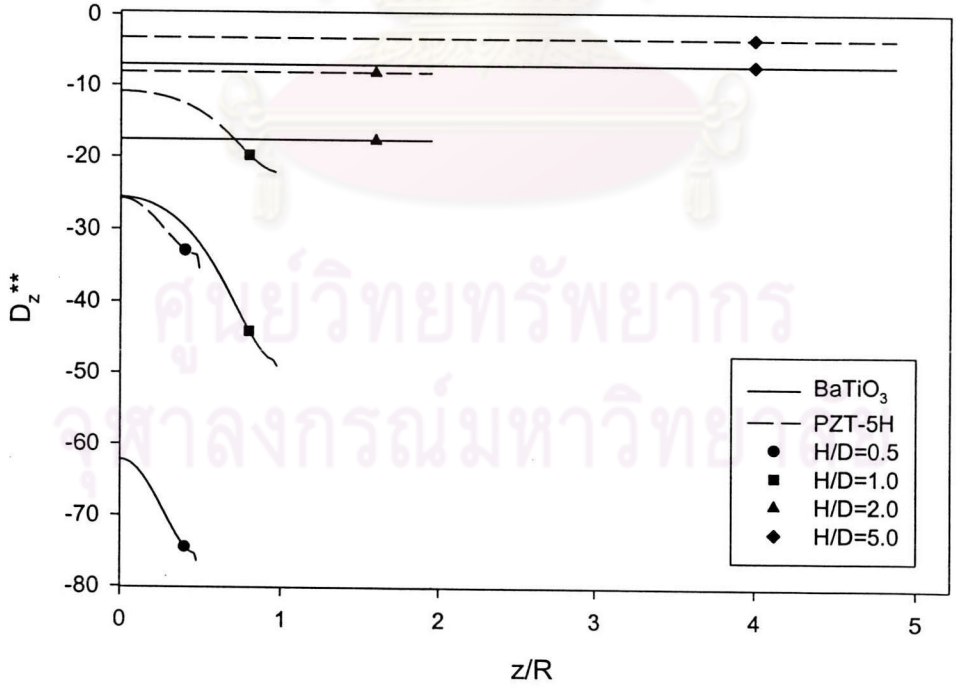

(b) Along z-axis at $r=0$

Figure 4.63 Non-dimensional vertical electric displacement profiles due to electrical loading for various shape factors H/D with flexible electrode.

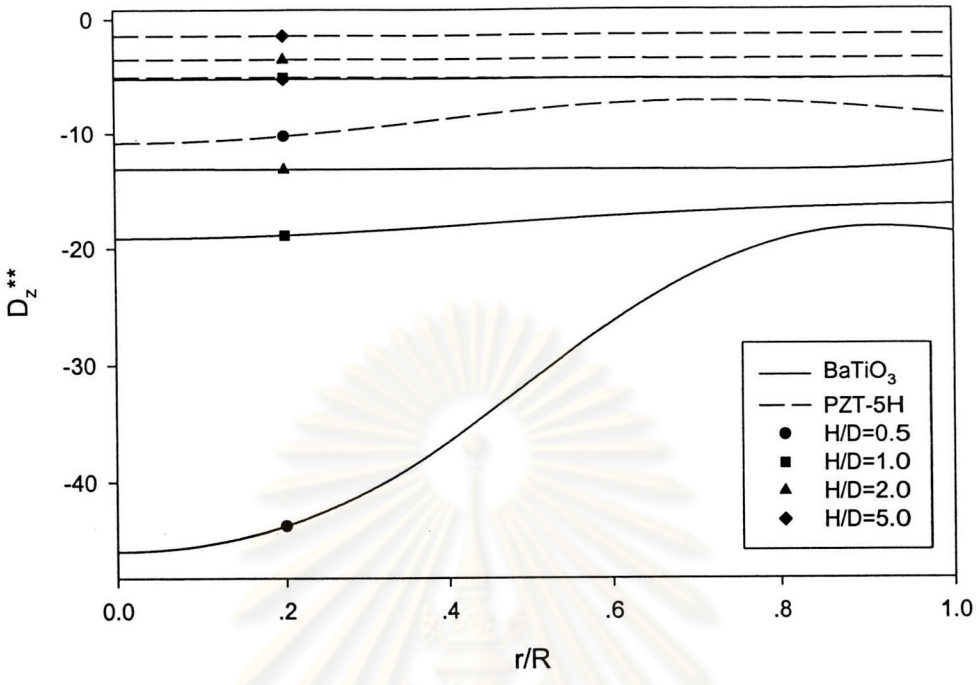

(a) Along r-axis at $z=0$

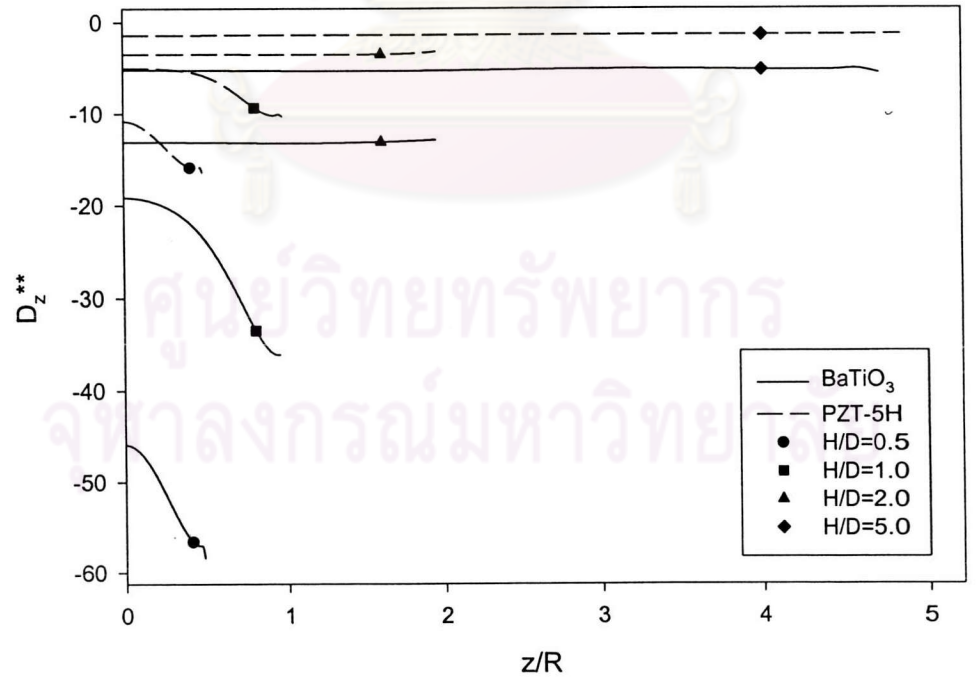

(b) Along z-axis at $r=0$

Figure 4.64 Non-dimensional vertical electric displacement profiles due to electrical loading for various shape factors H/D with rigid electrode.

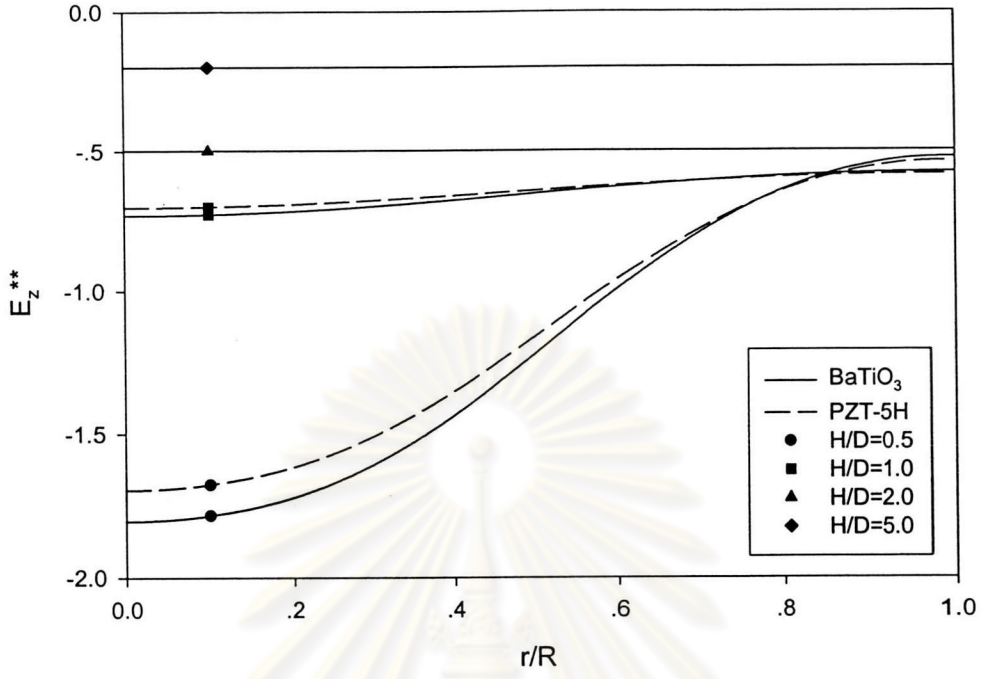

(a) Along r-axis at $z=0$

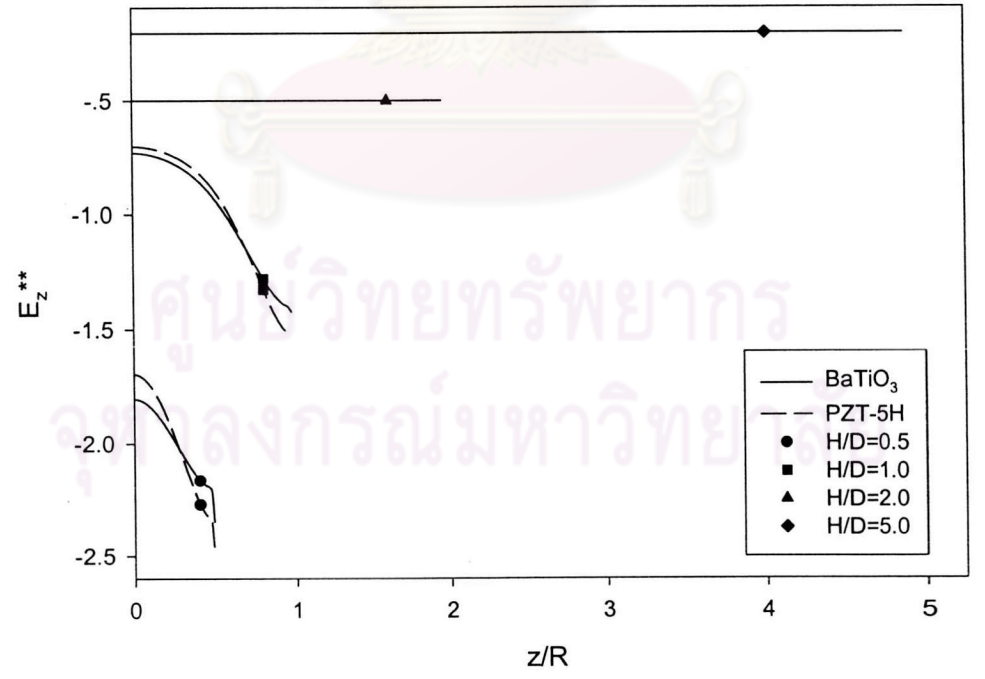

(b) Along z-axis at $r=0$

Figure 4.65 Non-dimensional vertical electric field profiles due to electrical loading for various shape factors H/D with flexible electrode.

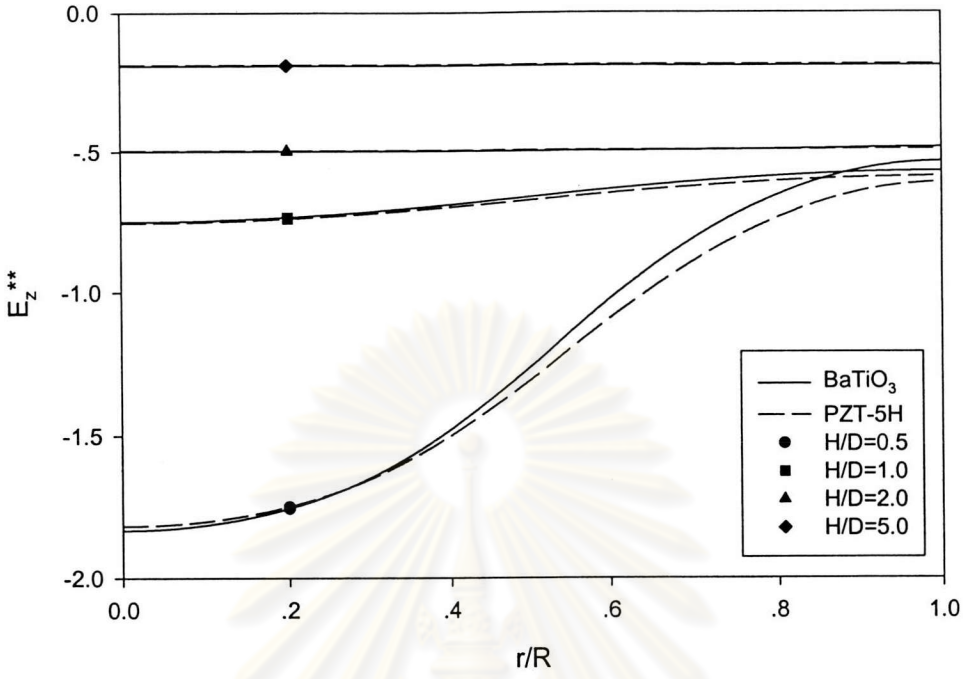

(a) Along r-axis at $z=0$

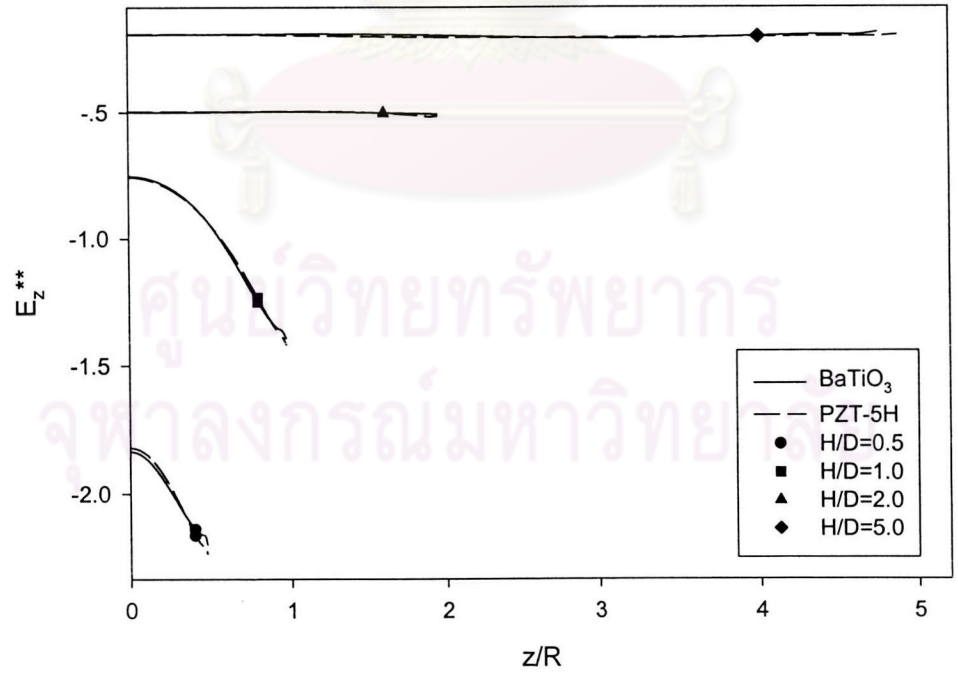

(b) Along z-axis at $r=0$

Figure 4.66 Non-dimensional vertical electric field profiles due to electrical loading for various shape factors H/D with rigid electrode.

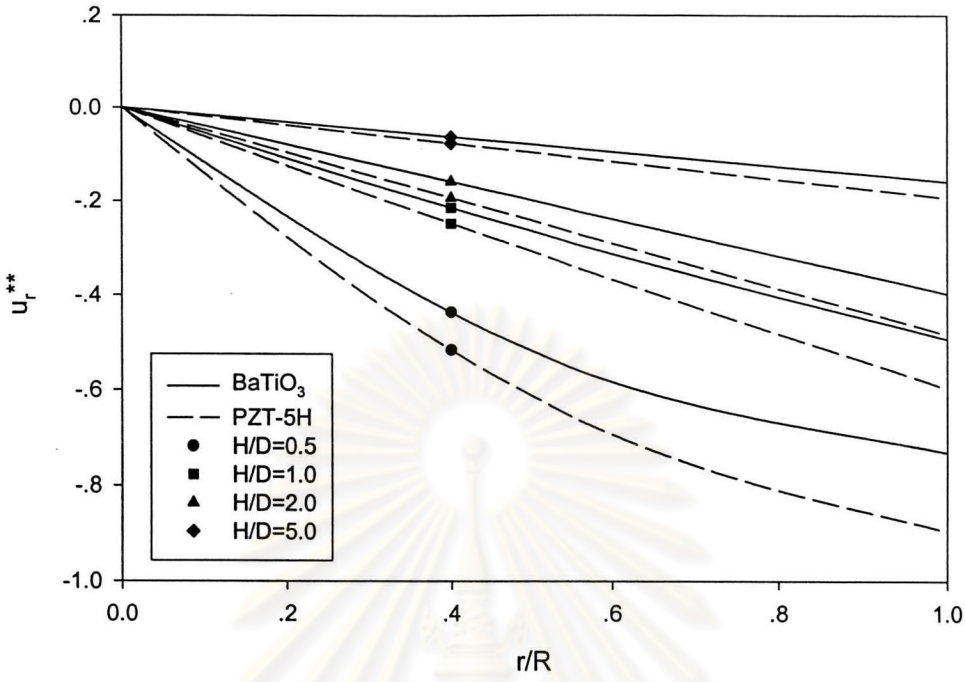

(a)

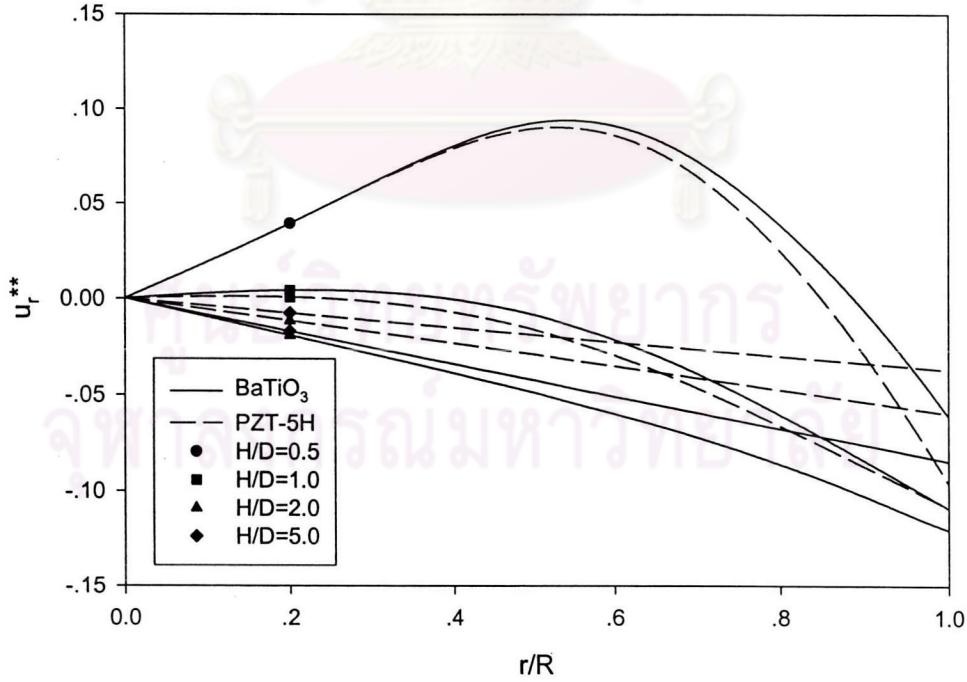

(b)

Figure 4.67 Non-dimensional radial displacements profiles due to electrical loading for various shape factors H/D with (a) flexible electrode and (b) rigid electrode.

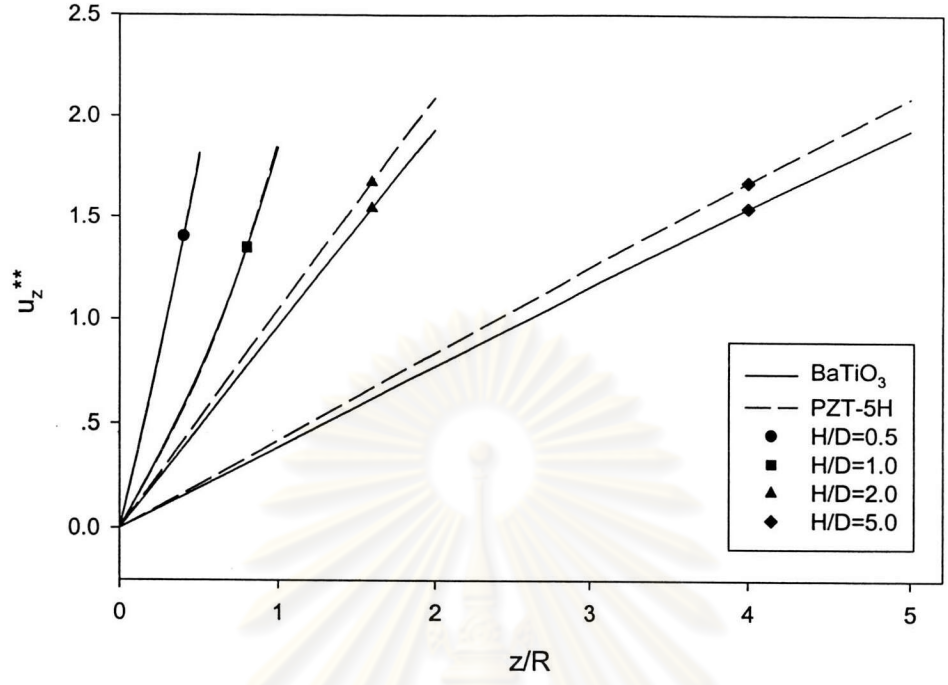

(a)

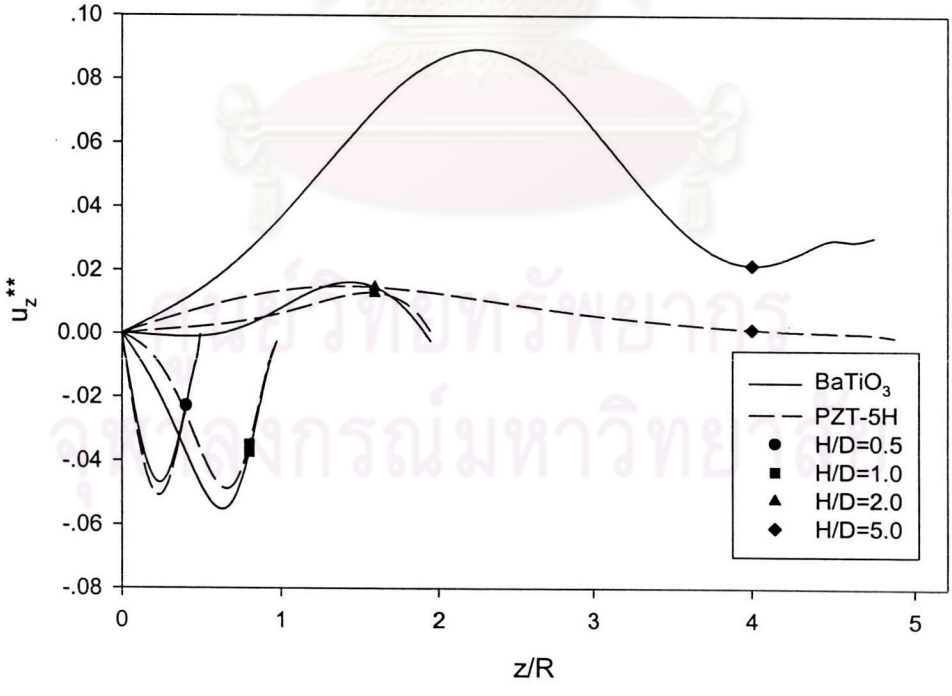

(b)

Figure 4.68 Non-dimensional vertical displacement profiles due to electrical loading for various shape factors H/D with (a) flexible electrode and (b) rigid electrode.

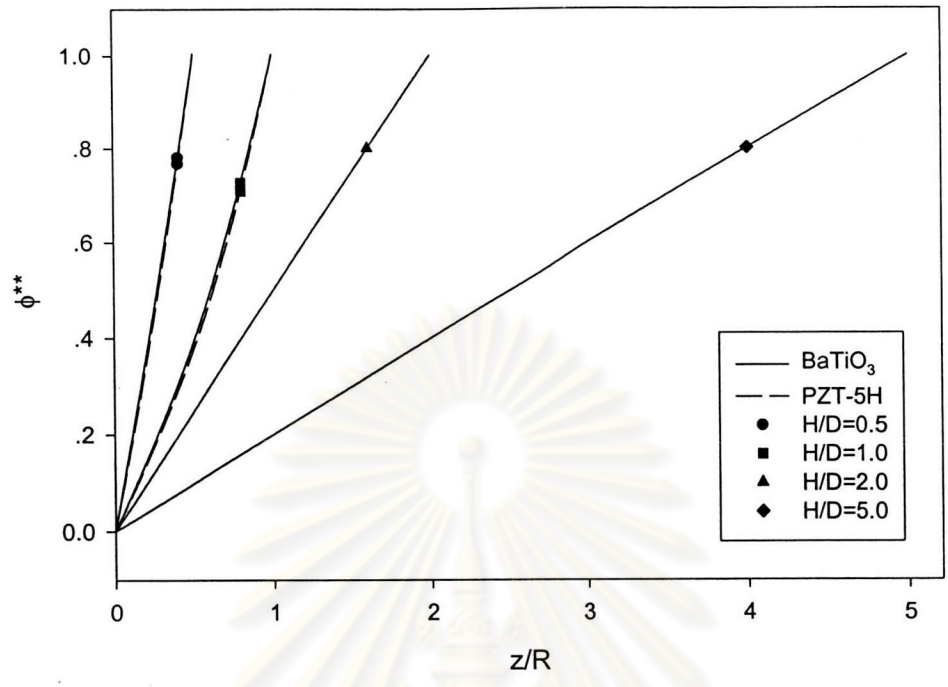

(a)

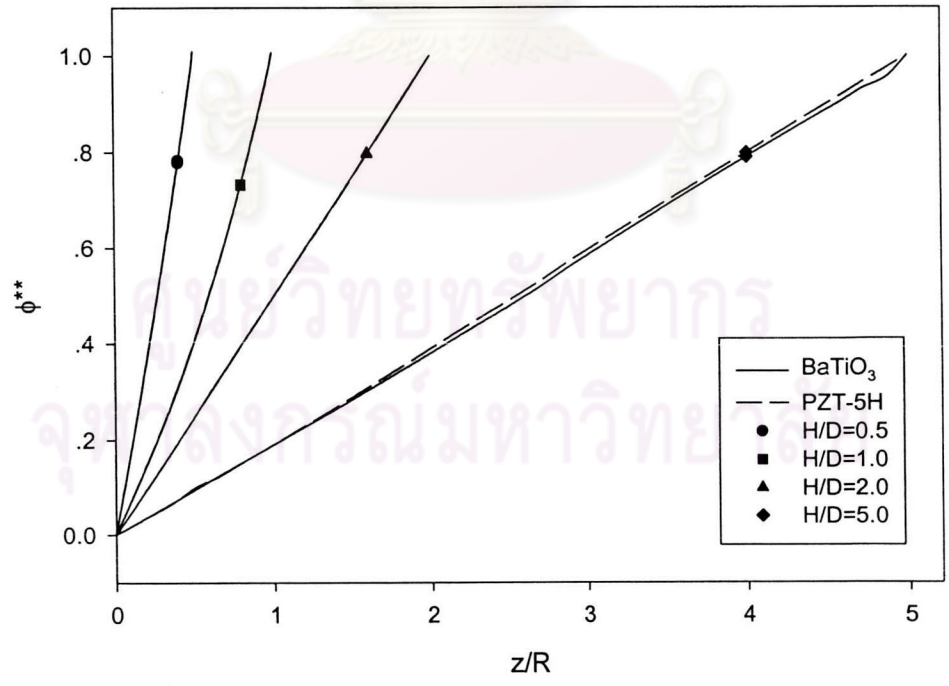

(b)

Figure 4.69 Non-dimensional electric potential profiles due to electrical loading for various shape factors H/D with (a) flexible electrode and (b) rigid electrode.

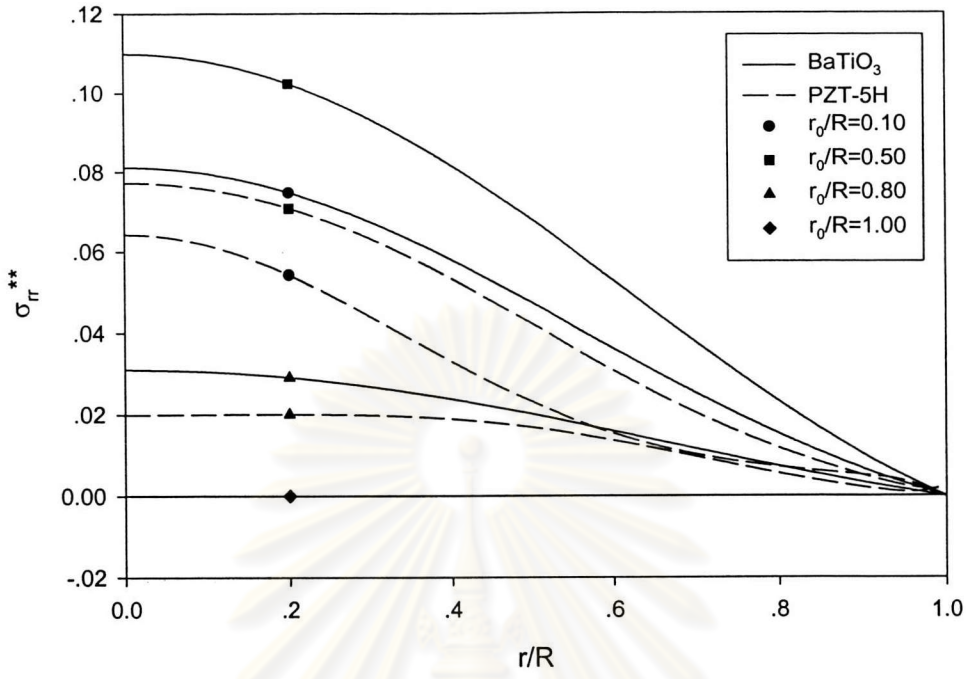

(a) Along r-axis at $z=0$

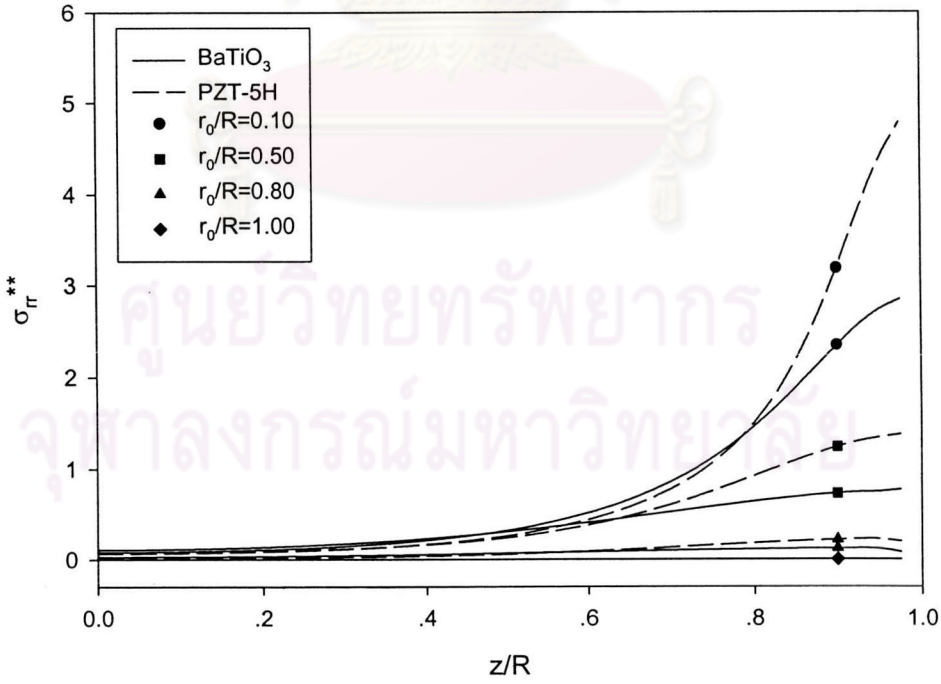

(b) Along z-axis at $r=0$

Figure 4.70 Non-dimensional radial stress profiles due to electrical loading for various radii of flexible electrode.

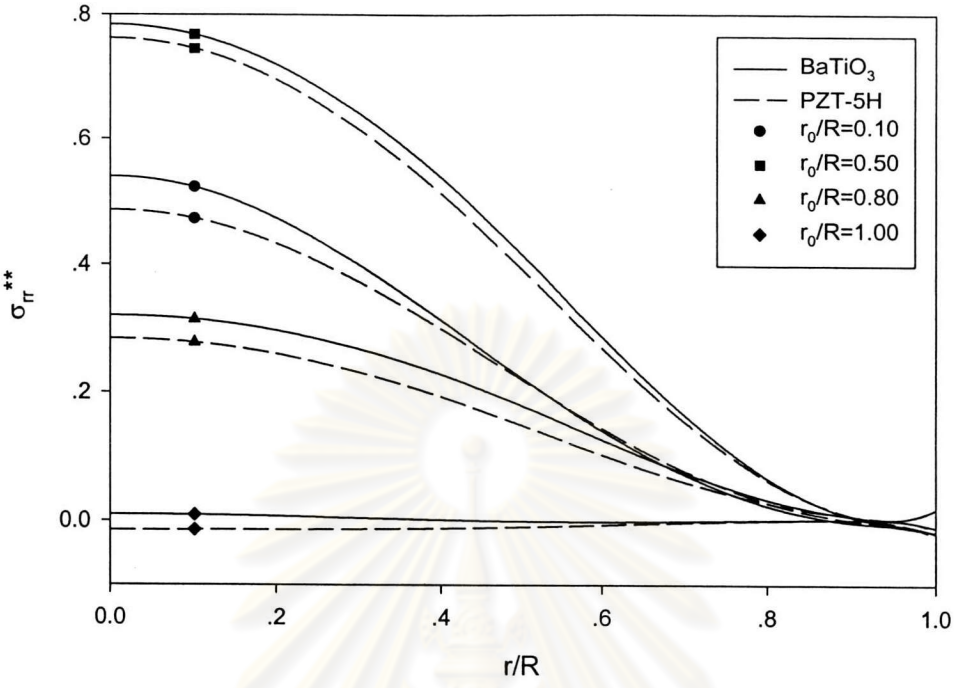

(a) Along r-axis at $z=0$

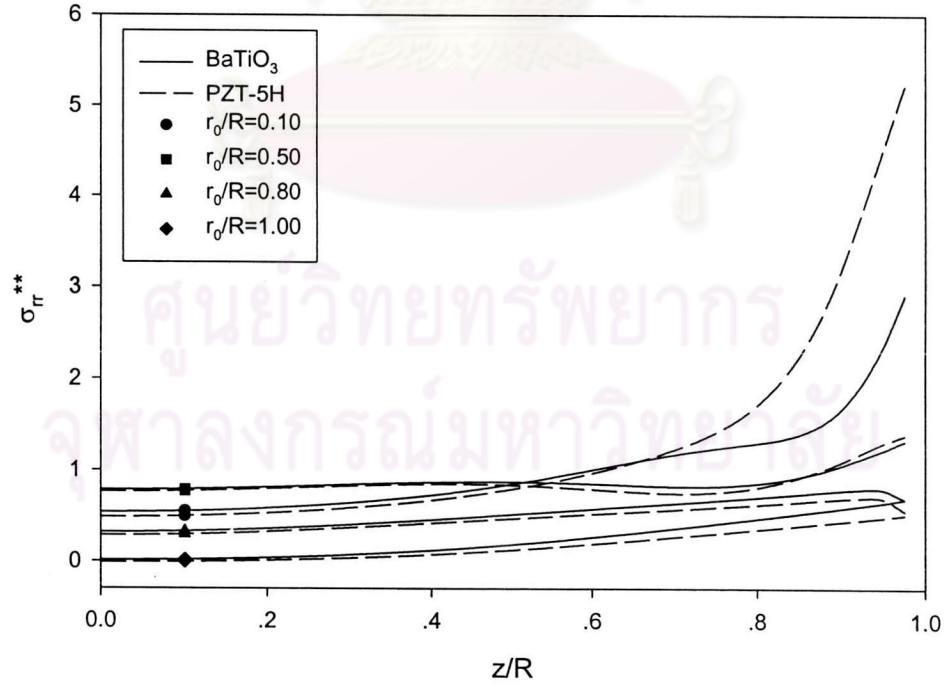

(b) Along z-axis at $r=0$

Figure 4.71 Non-dimensional radial stress profiles due to electrical loading for various radii of rigid electrode.

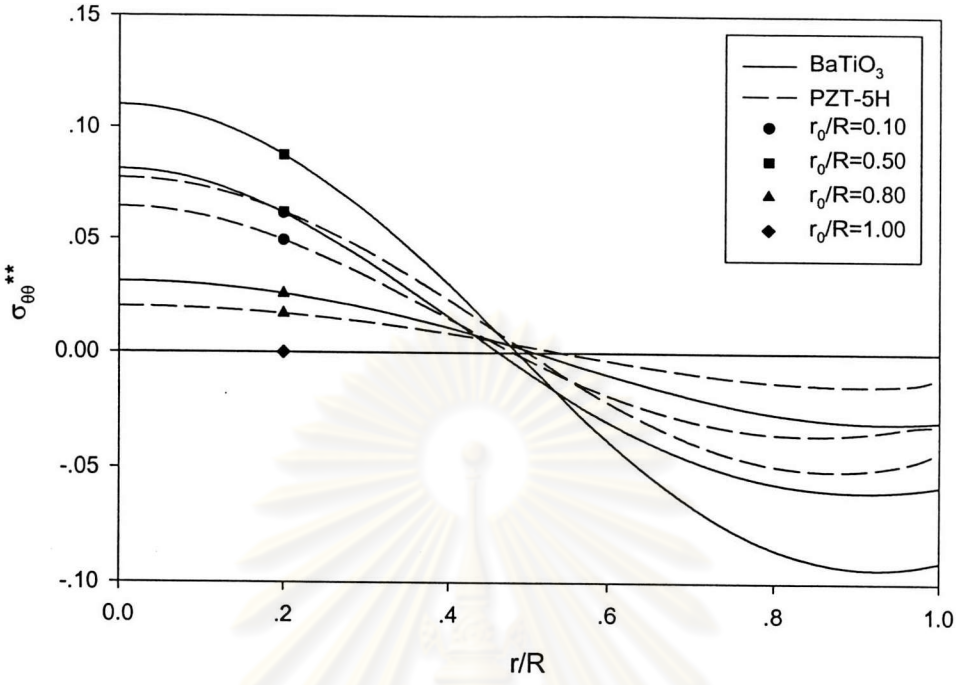

(a) Along r-axis at $z=0$

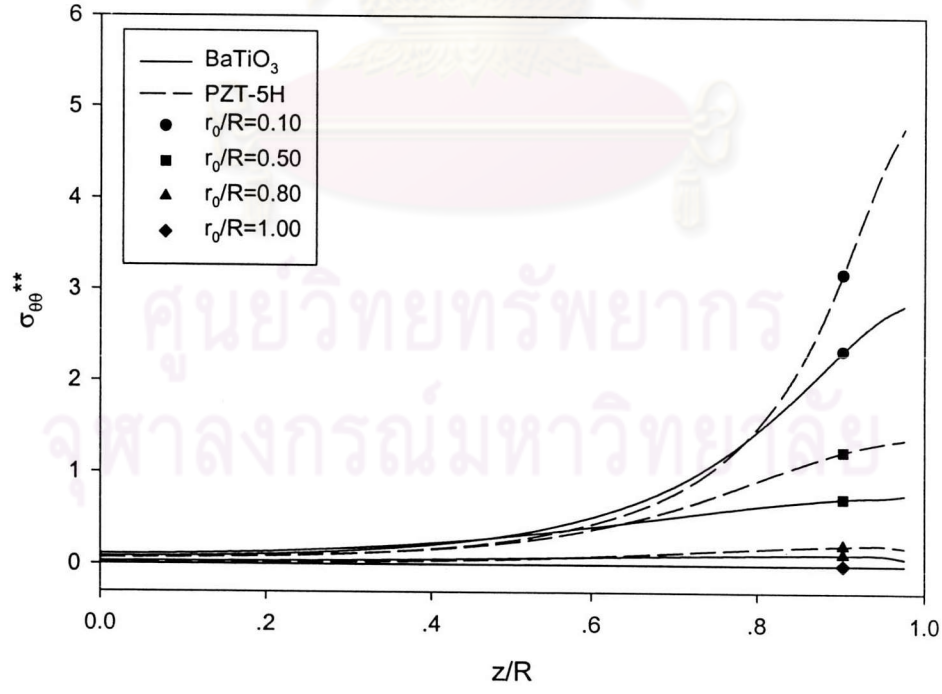

(b) Along z-axis at $r=0$

Figure 4.72 Non-dimensional hoop stress profiles due to electrical loading for various radii of flexible electrode.

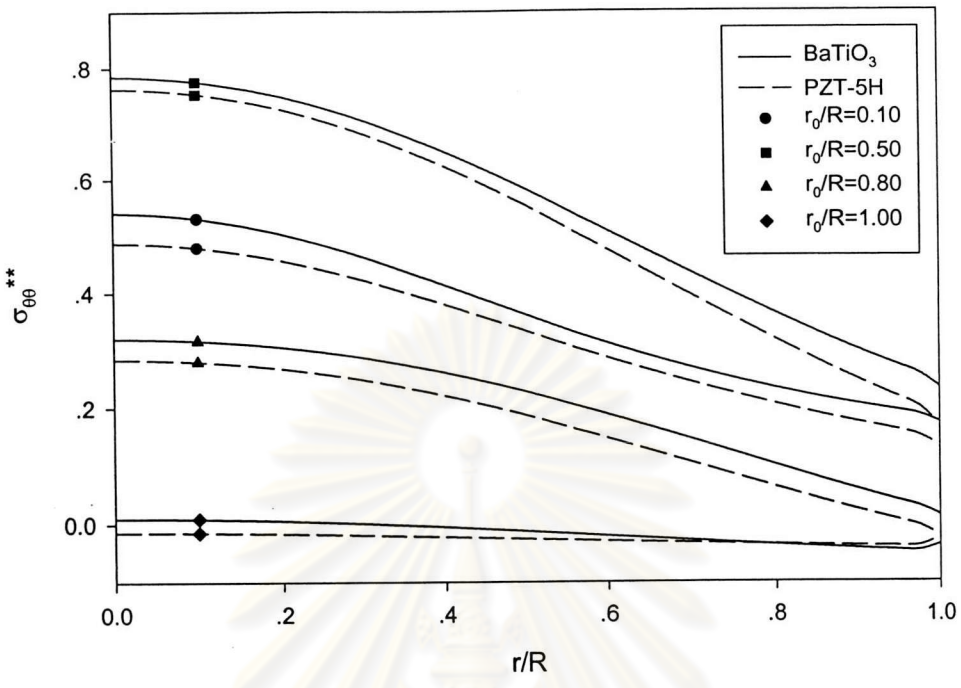

(a) Along r-axis at $z=0$

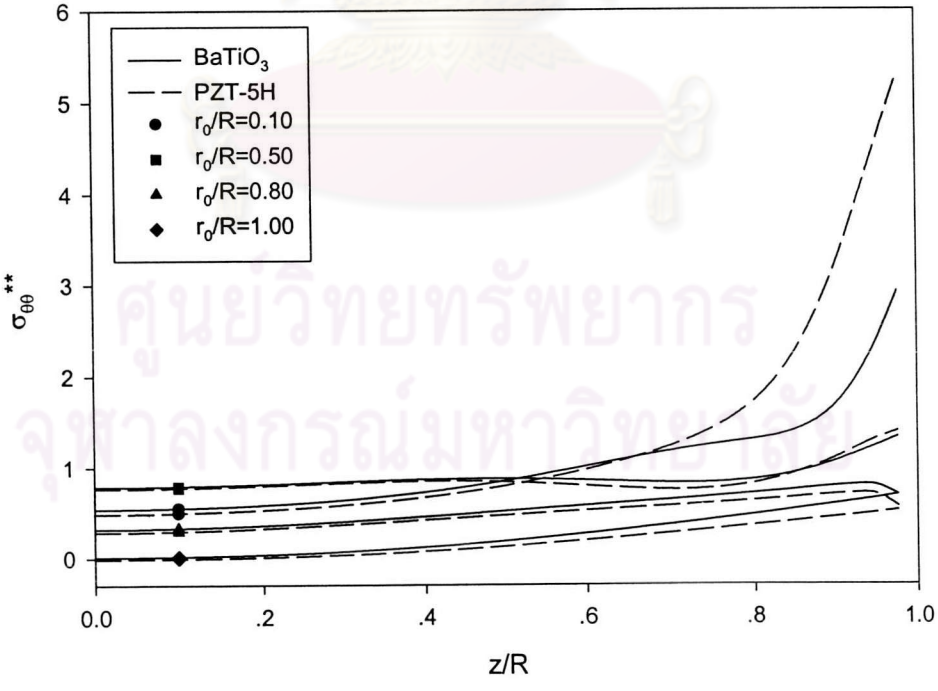

(b) Along z-axis at $r=0$

Figure 4.73 Non-dimensional hoop stress profiles due to electrical loading for various radii of rigid electrode.

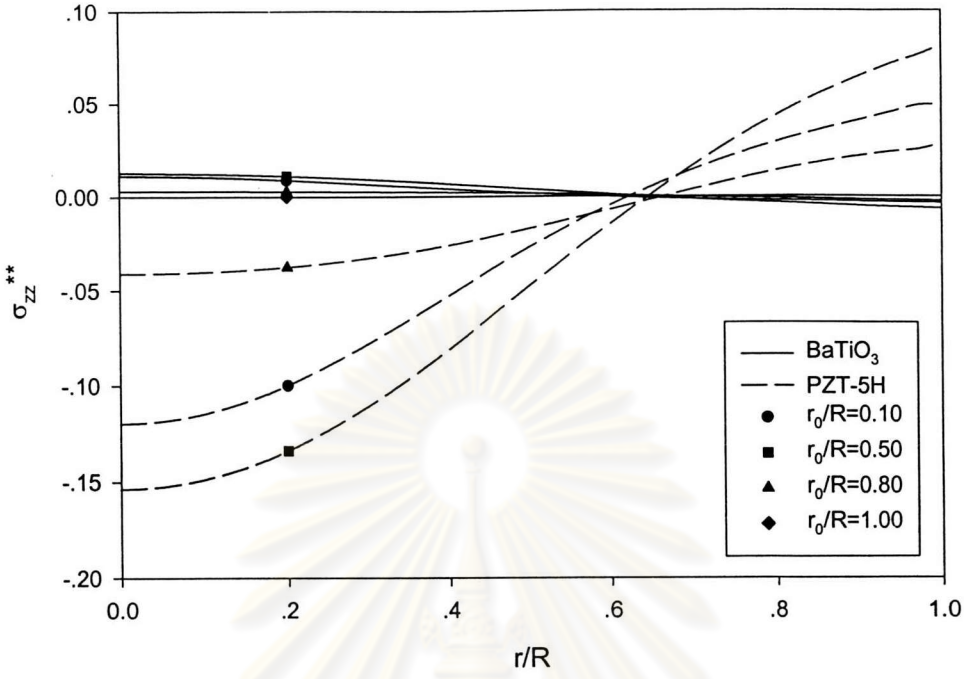

(a) Along r-axis at $z=0$

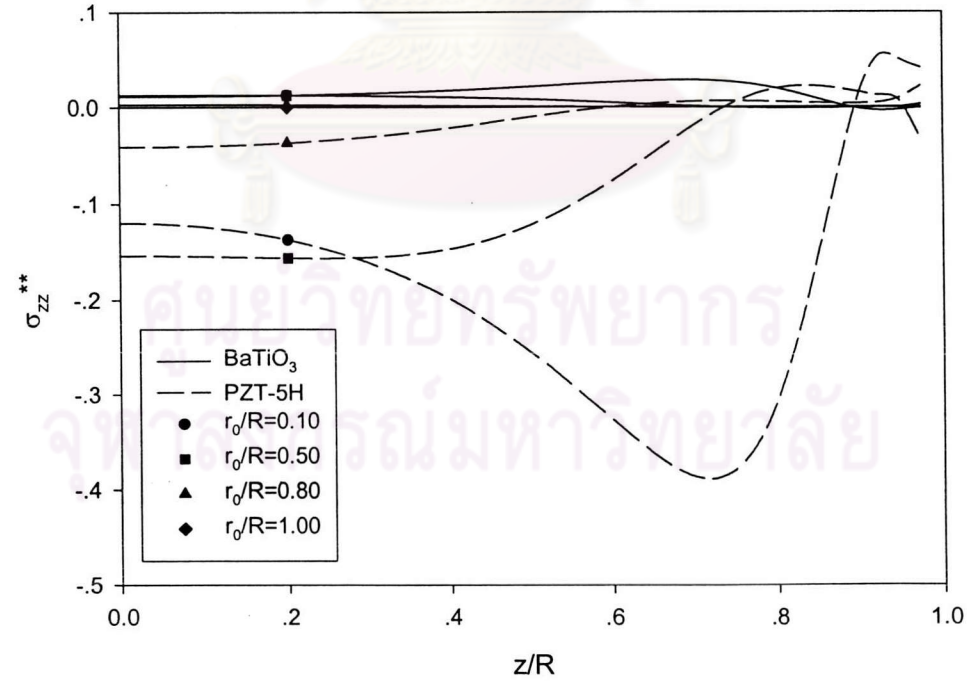

(b) Along z-axis at $r=0$

Figure 4.74 Non-dimensional vertical stress profiles due to electrical loading for various radii of flexible electrode.

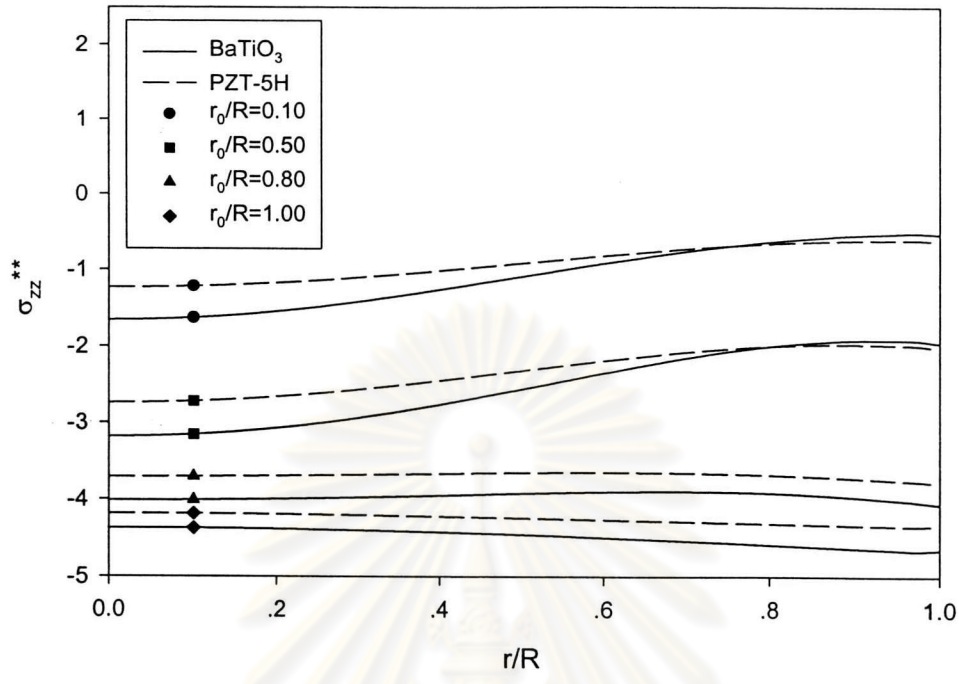

(a) Along r-axis at $z=0$

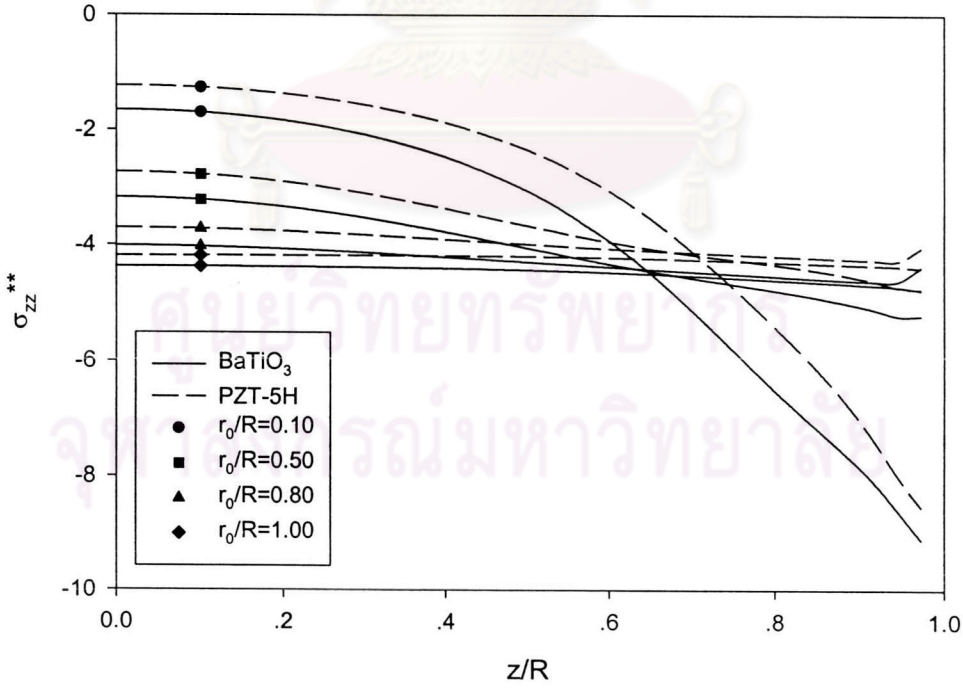

(b) Along z-axis at $r=0$

Figure 4.75 Non-dimensional vertical stress profiles due to electrical loading for various radii of rigid electrode.

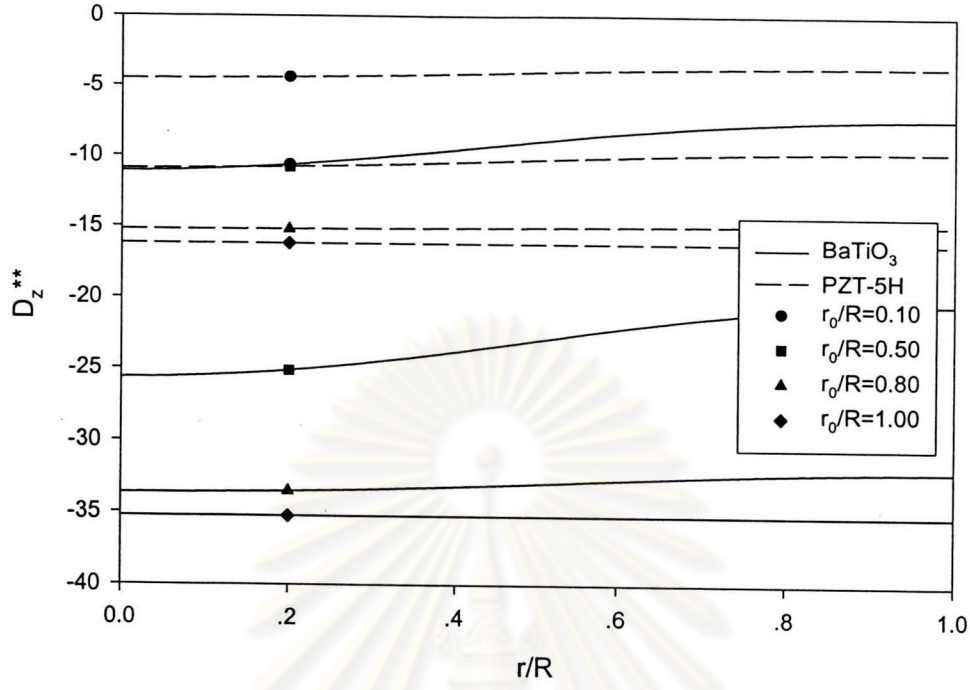

(a) Along r-axis at $z=0$

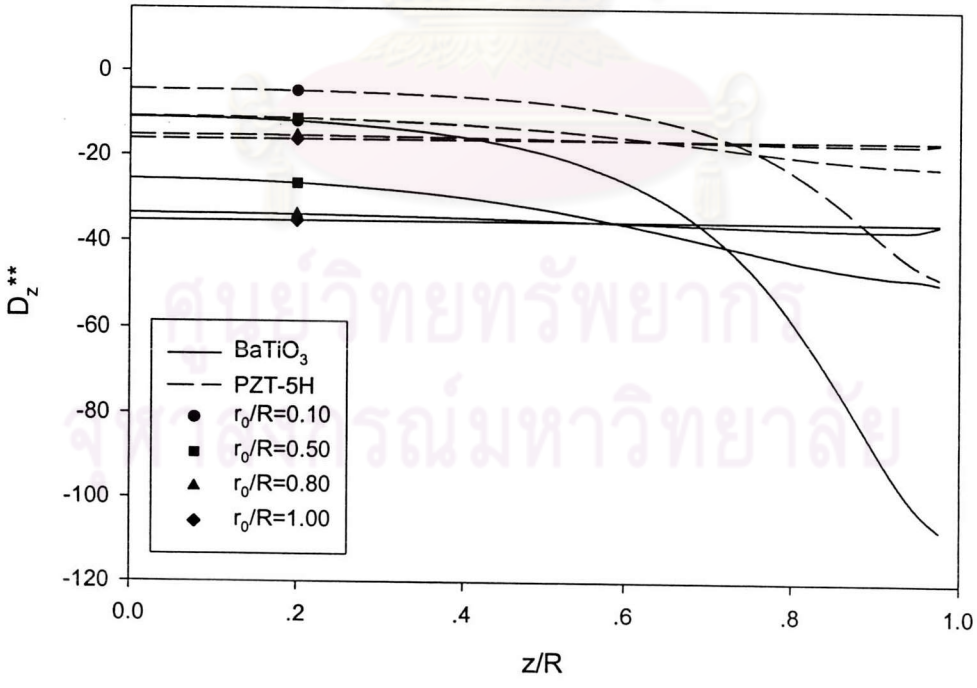

(b) Along z-axis at $r=0$

Figure 4.76 Non-dimensional vertical electric displacement profiles due to electrical loading for various radii of flexible electrode.

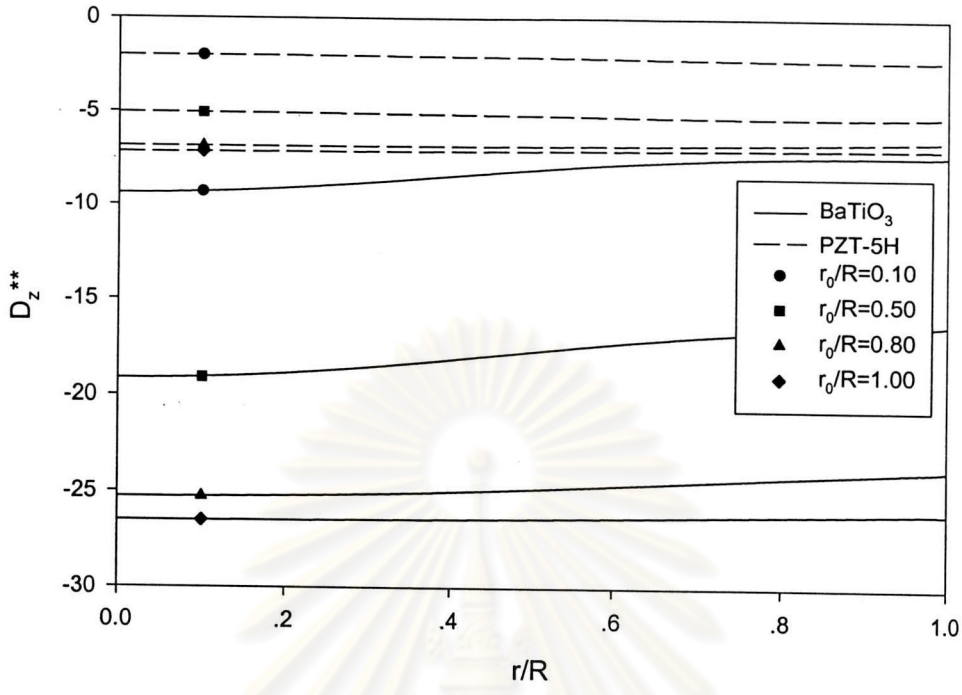

(a) Along r-axis at $z=0$

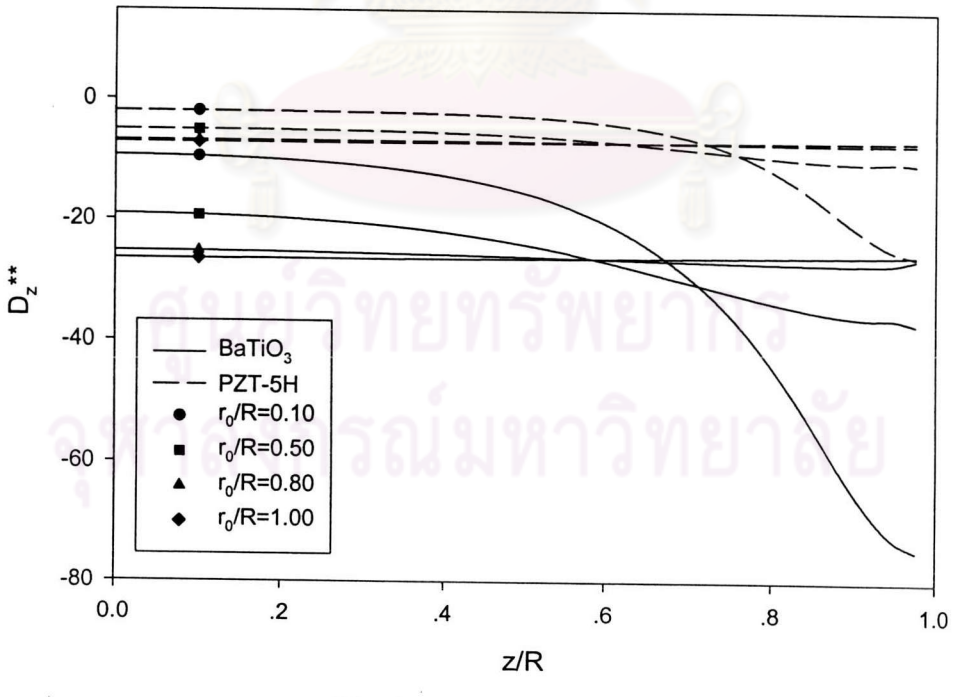

(b) Along z-axis at $r=0$

Figure 4.77 Non-dimensional vertical electric displacement profiles due to electrical loading for various radii of rigid electrode.

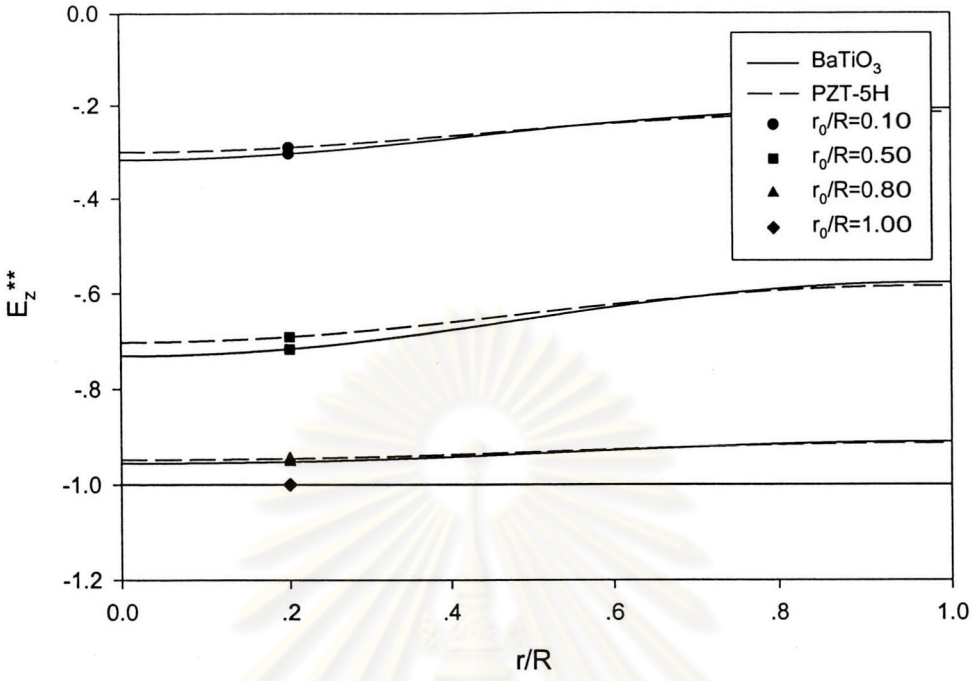

(a) Along r-axis at $z=0$

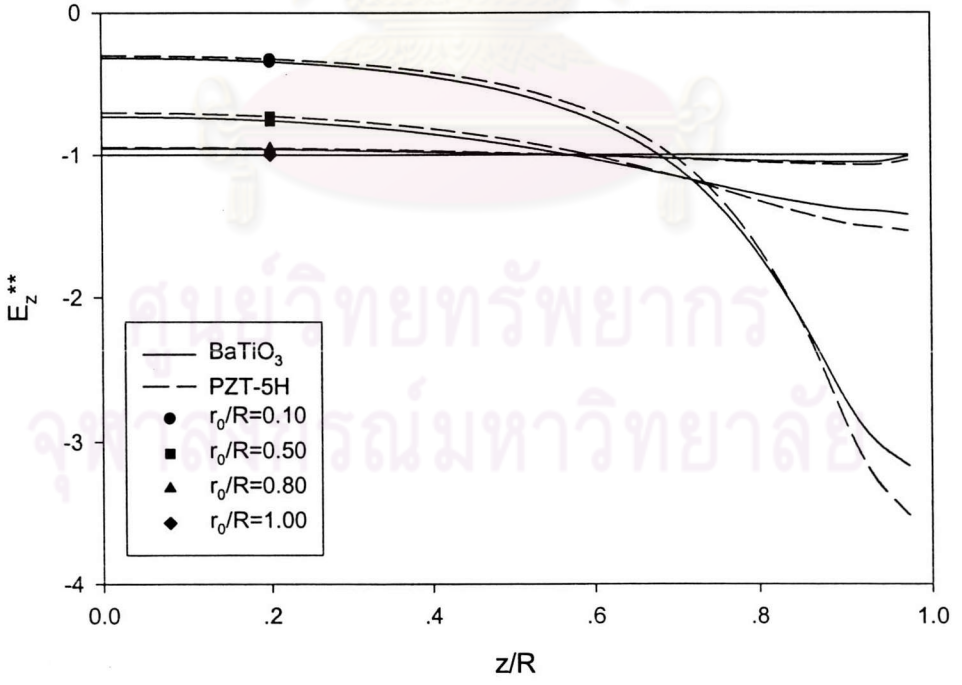

(b) Along z-axis at $r=0$

Figure 4.78 Non-dimensional vertical electric field profiles due to electrical loading for various radii of flexible electrode.

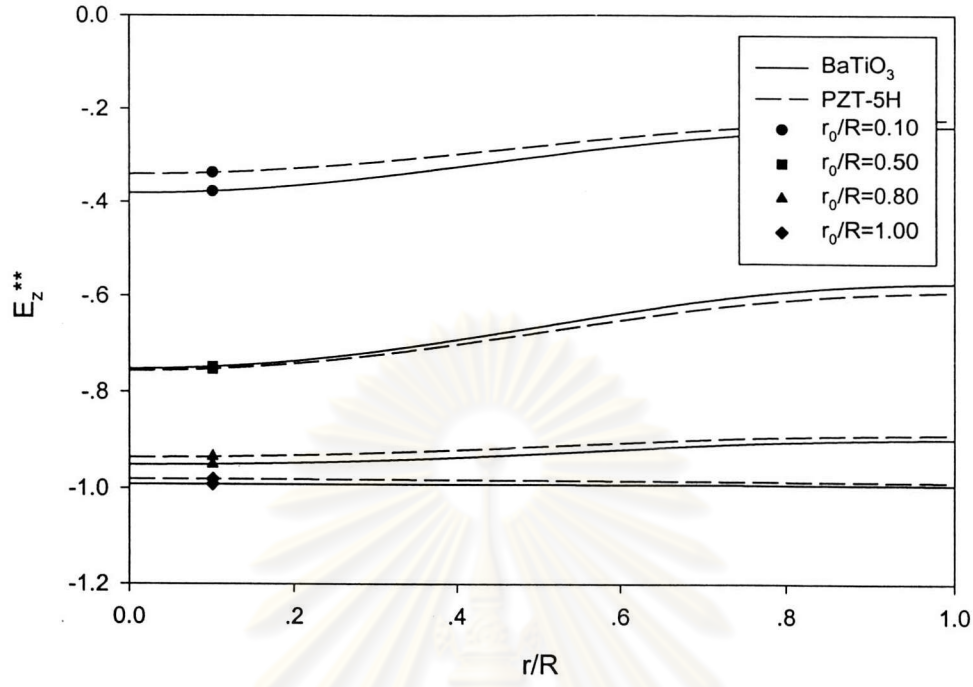

(a) Along r-axis at $z=0$

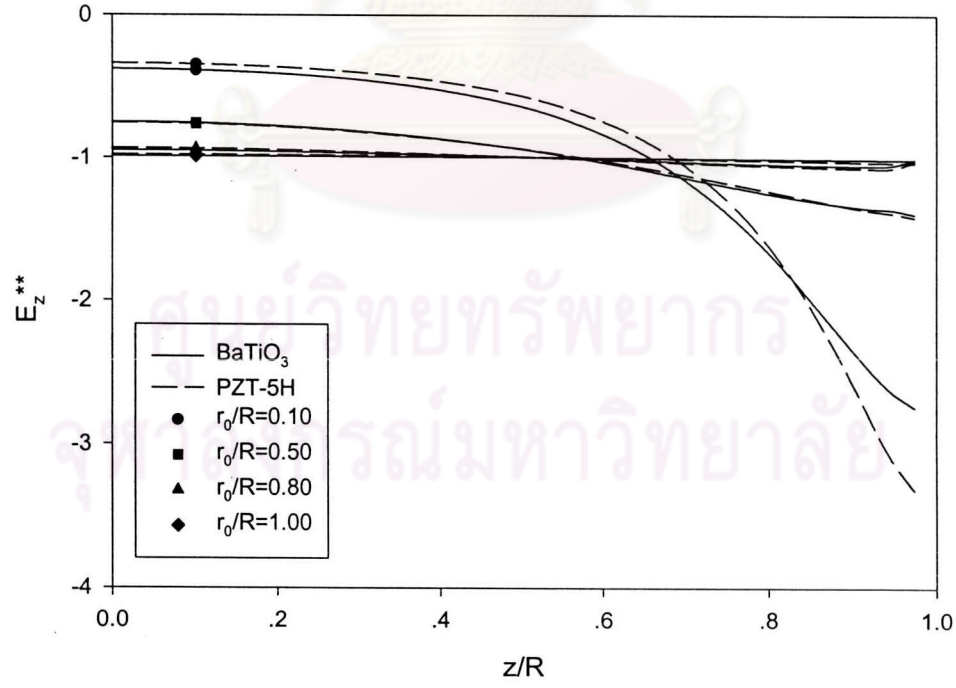

(b) Along z-axis at $r=0$

Figure 4.79 Non-dimensional vertical electric field profiles due to electrical loading for various radii of rigid electrode.

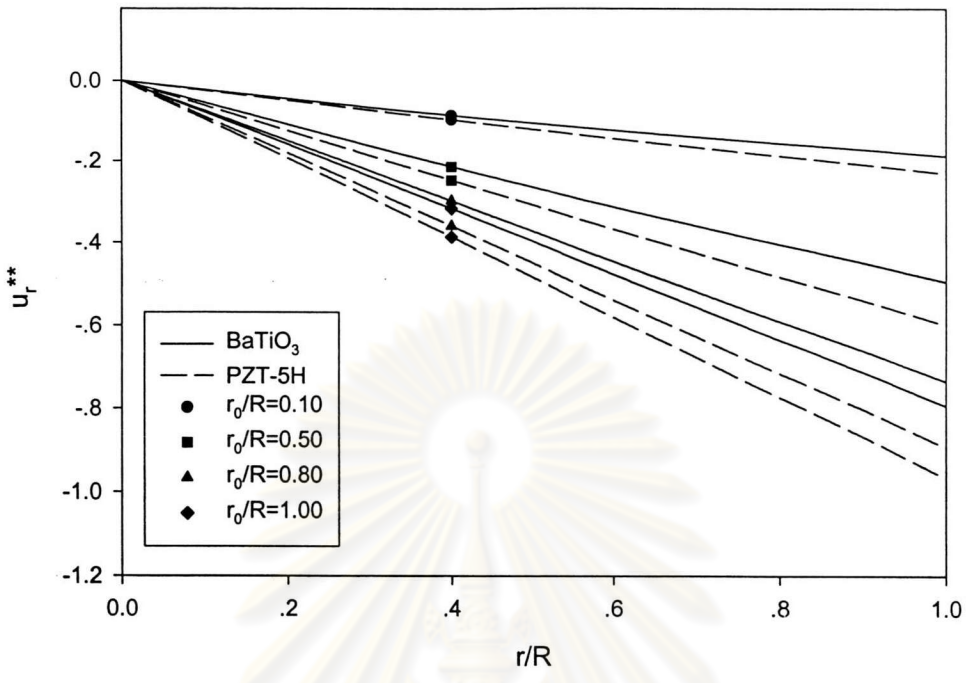

(a)

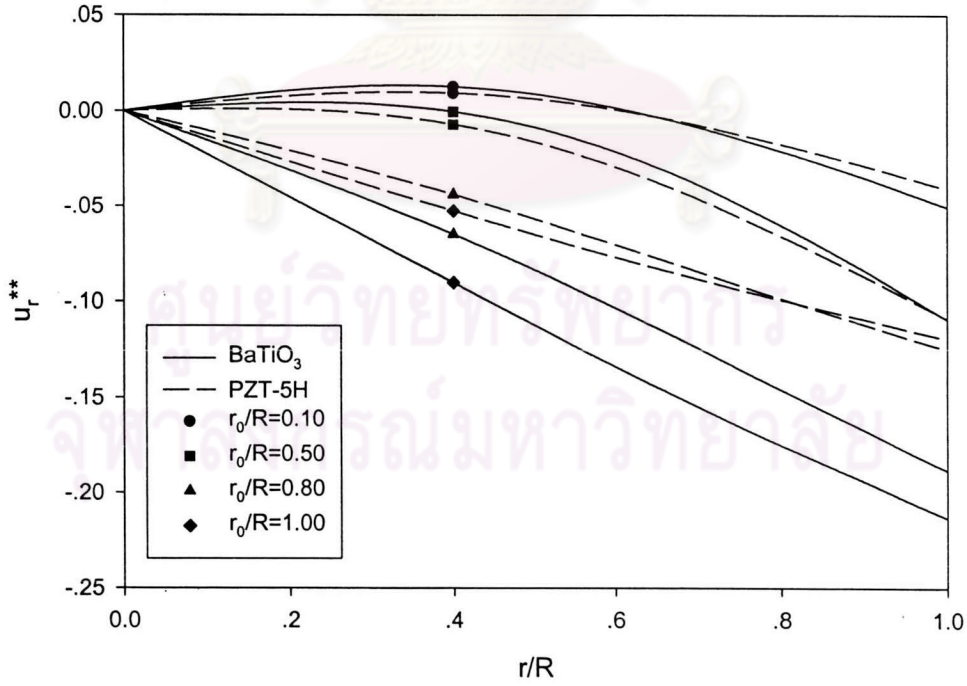

(b)

Figure 4.80 Non-dimensional radial displacements profiles due to electrical loading for various radii of (a) flexible electrode and (b) rigid electrode.

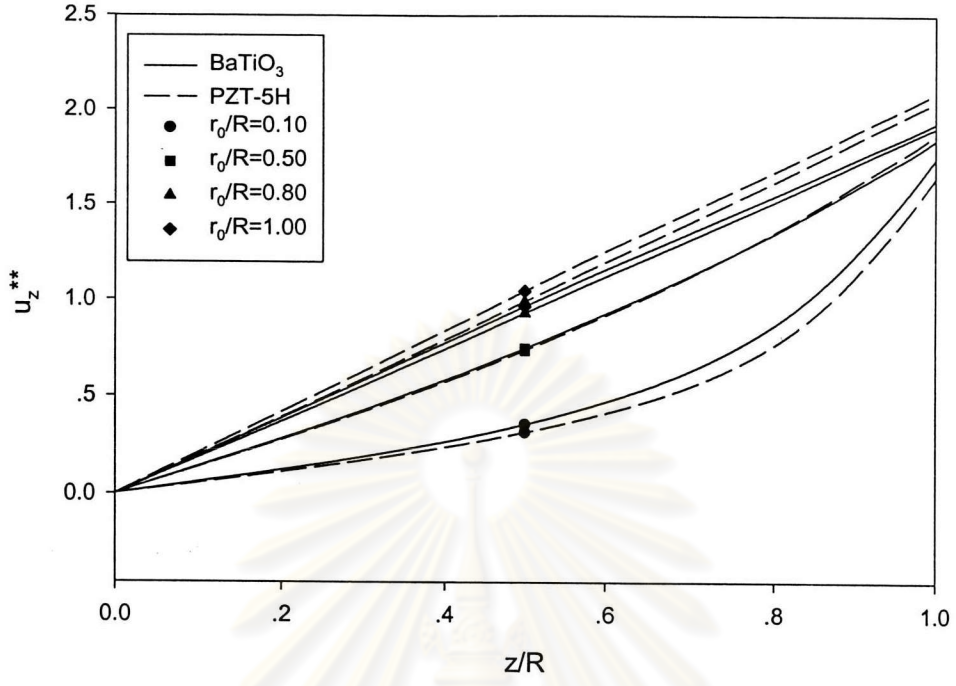

(a)

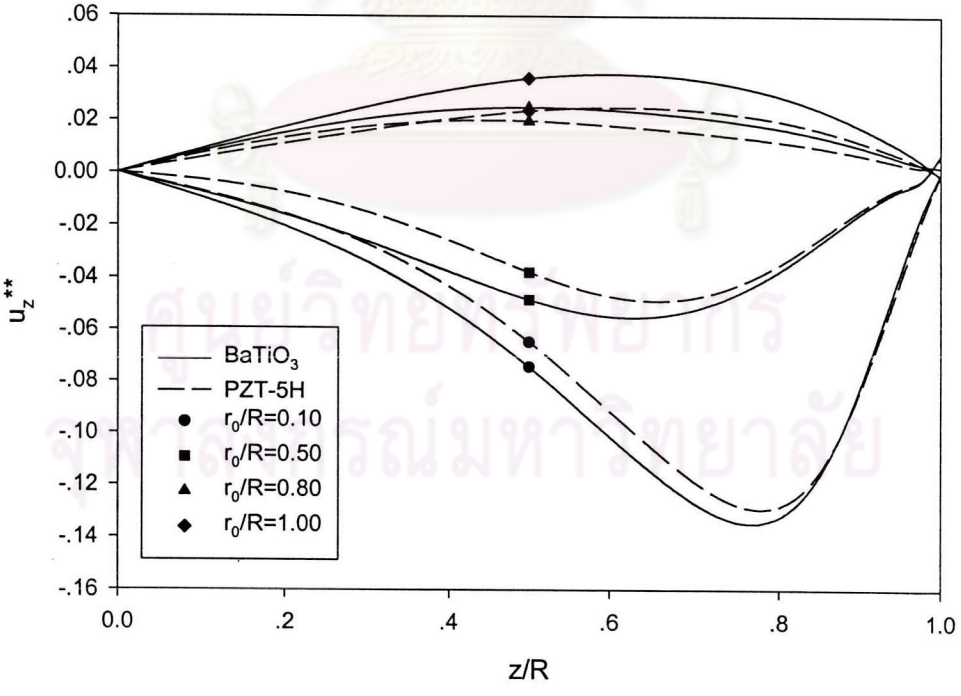

(b)

Figure 4.81 Non-dimensional vertical displacements profiles due to electrical loading for various radii of (a) flexible electrode and (b) rigid electrode.

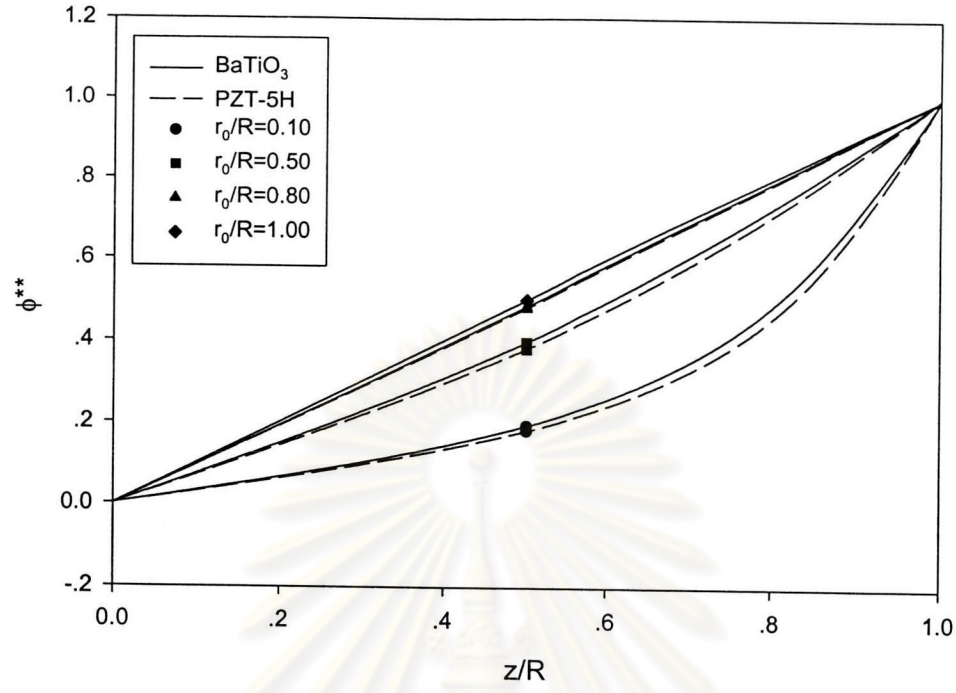

(a)

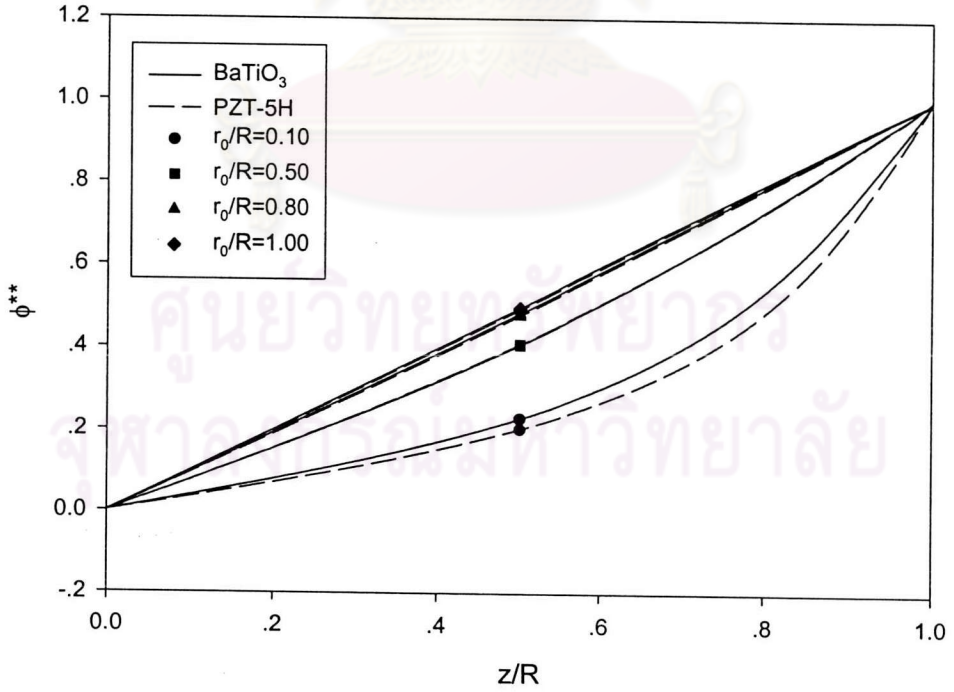

(b)

Figure 4.82 Non-dimensional electric potential profiles due to electrical loading for various radii of (a) flexible electrode and (b) rigid electrode.